

5. TWO INTERACTION REGION DESIGN

Figure 7 shows schematically four arrangements of the two vaults and their associated staging areas. In (a) each vault has its own staging area. In (b) the vaults share a staging area. In (c) the vaults are adjacent which gives a minimum distance between the two beam lines. This is a minimum cost design, there are no staging areas, and each detector must be assembled in its own pit. Design (d) also has adjacent vaults, but now one of the areas has a staging area. Hence one of the detectors can be assembled off its beam line. The extension of design (d) to two separated staging areas is straight forward and is not considered here. At this time we have ruled out option (a), since it is the most expensive, and has no crucial advantages over (b), (c) or (d).

Options (b), (c) or (d) could be carried out by the cut-and-fill construction method, or by the below-ground method. Section 5b describes option (b) designs using both construction methods. Section 5c describes an option (c) design using the below-ground construction method. Finally Sec. 5d describes an option (d) below-ground design.

a. Two Staging Areas, 2IR Design

This design allows both detectors to be simultaneously withdrawn from their vaults. This is a convenient, but expensive, capability, and it has not been studied in detail.

b. Shared Staging Area, 2IR Designs.

This concept has been studied using the cut-and-fill construction method and using the below-ground construction method.

(i) Cut-and-Fill Construction Method: A plan view of this design is shown in Fig. 8. The interaction hall consists of two equal-sized vaults, each 14 meters wide and 16 meters long. The common staging area is 20 meters wide and 18 meters long. Access to the staging area is through a door 12 meters wide looking out on to a turnabout and parking area and access road. The common staging area is separated from the

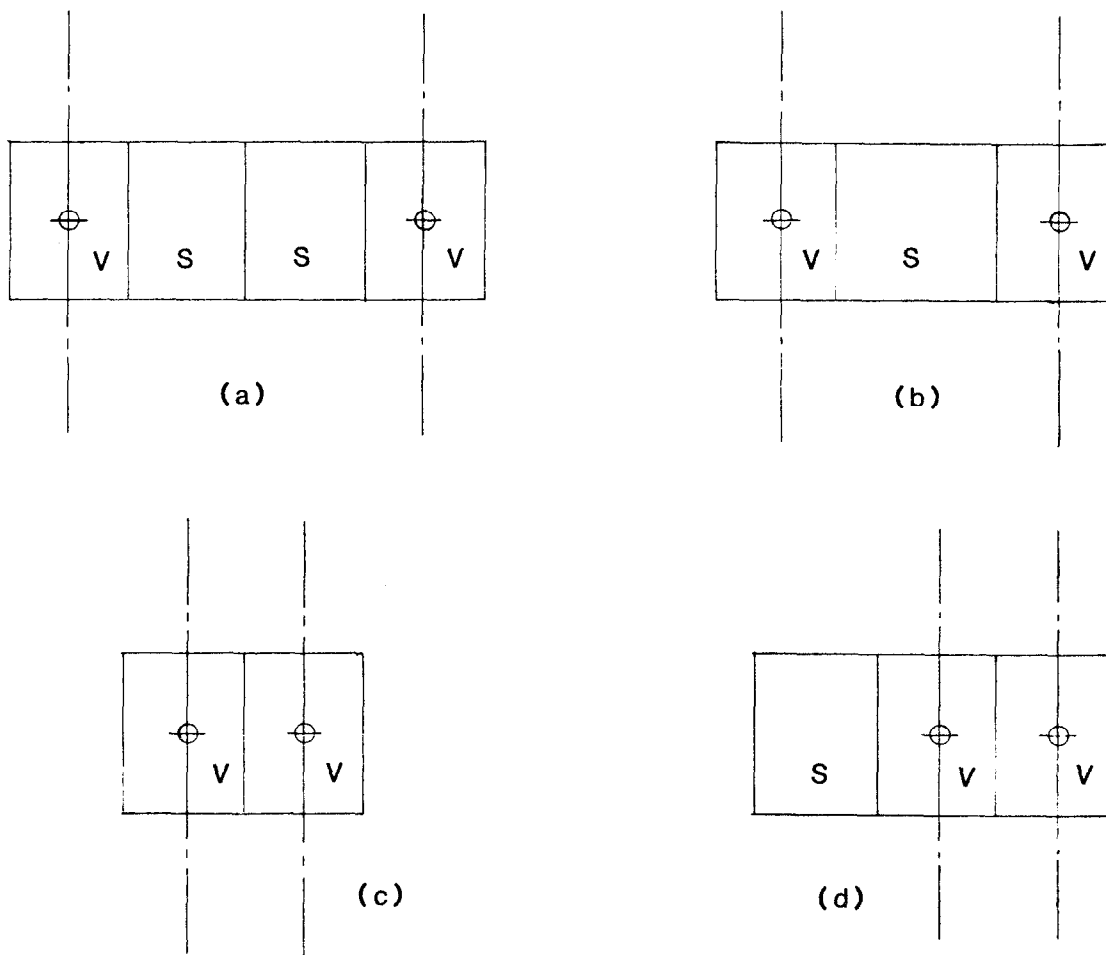


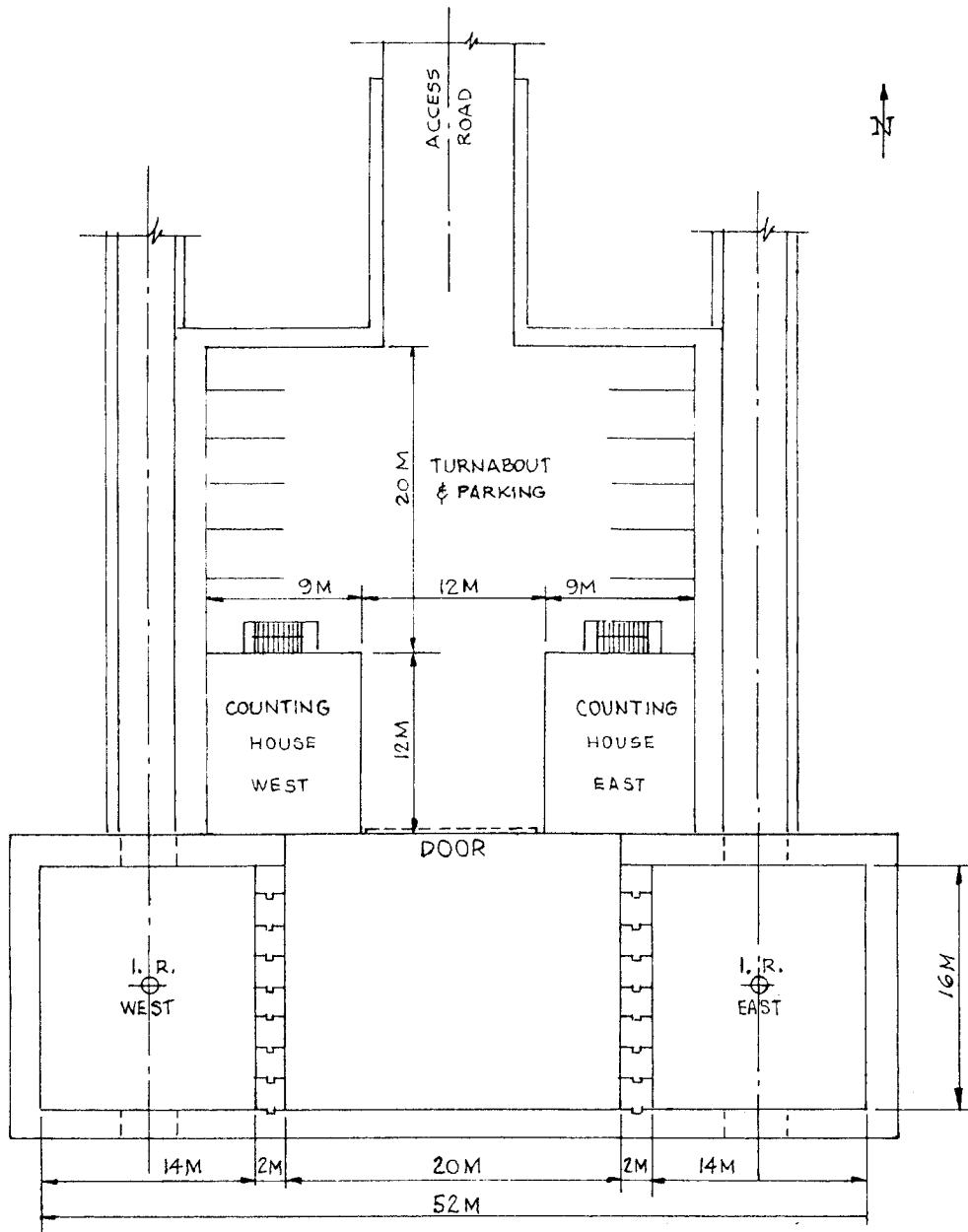
FIG. 7

Schematic Plan View of four 2 I.R. Designs :

- (a) Two staging areas
- (b) Shared staging area
- (c) No staging area
- (d) Staging area for one vault

V : Vault

S : Staging area



PLAN VIEW

FIG. 8 PLAN VIEW OF CUT-AND-FILL,
SHARED STAGING AREA, 2IR DESIGN

vaults by concrete-block shielding walls and an overhead curtain, similar to the schemes now in practice at PEP. An overhead 50 ton crane provides coverage of the assembly area, and by pushing the curtains into garage compartments at the far side of the vaults, crane coverage of the detectors in the vault areas is possible.

The beam lines are 38 m apart. It might be possible to decrease this distance by about 6 m by reducing the staging area width to 14 m. This distance is one distinct disadvantage of this scheme relative to other with closer spacing, because it requires longer tunnels to bring the beams to the two vaults, and hence additional costs in tunnel construction and technical components.

Separate counting houses are located at the same level and near to each detector. Cable runs to the detectors will be short if the LEACH electronics are located near to the ground level. The counting houses are each 4 stories high, with the ground floor allocated to conventional use such as tools, storage space, and perhaps some cryogenics. The second and third levels are for fast electronics and computers. The fourth level can contain additional detector support equipment. Location of a utility pad for power and gas supplies is not specified, but a suitable pad can be located near the surface off to one side, or perhaps on the roof of the assembly area.

Excavation of an area for this interaction region is quite expensive because the cuts are quite deep. Considerably larger amounts of concrete are used in the support walls in this design compared with other 2IR designs considered. Nevertheless, a two-vault design of this kind provides the best access for staging of large experiments.

(ii) Below-Ground Construction Method: The below-ground construction method can also be used for the shared staging area, 2IR design. Three overlapping circular pits might be used as described in Sec. 4c, or one larger pit with additional underground excavation might be used. The distance between the beam lines would probably be set at 32 m to minimize the excavation costs. Each vault and the shared staging area would then be 14 m wide.

This design, as well as the cut-and-fill version, have the following advantageous features: during studies of the final focus system in either IR the detector destined for that IR need not be in the IR; either detector can be retracted for changes or repairs, and an IR can be used for a small-term, small experiment while a large detector is on standby in the staging area. The disadvantage of this shared staging area design, as has already been stated, is the additional cost of longer arcs.

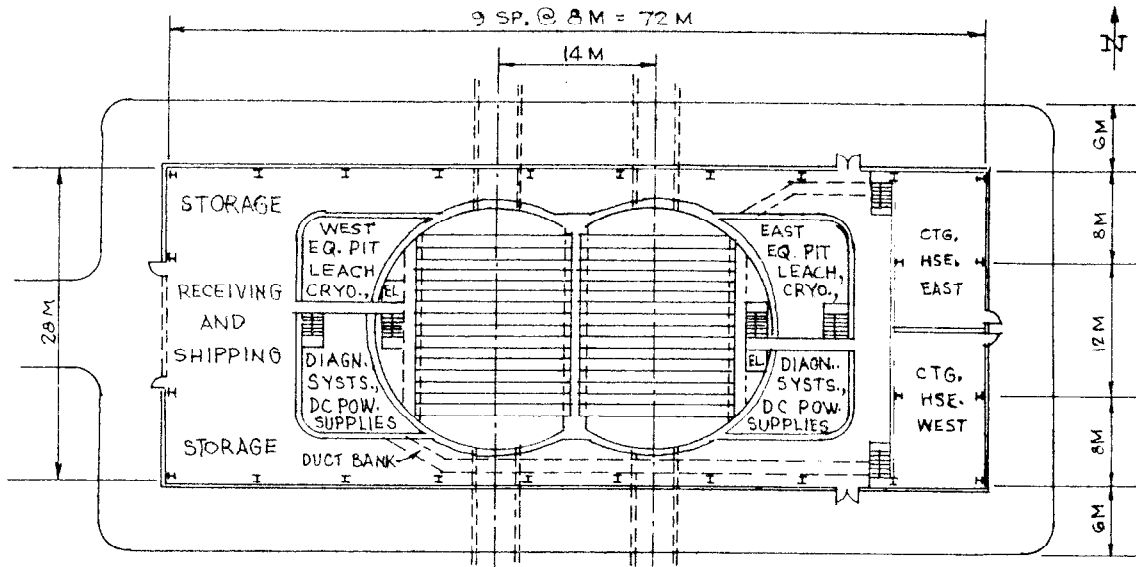
c. Below-Ground, Minimum 2IR Design

This design is intended to provide two interaction regions at minimum cost for the experimental area. There is a trade-off in this design. Construction costs are smaller than in other 2IR designs; but compared to option (b) it is more difficult and more time consuming for the experimenters to assemble, check out, and service their detector.

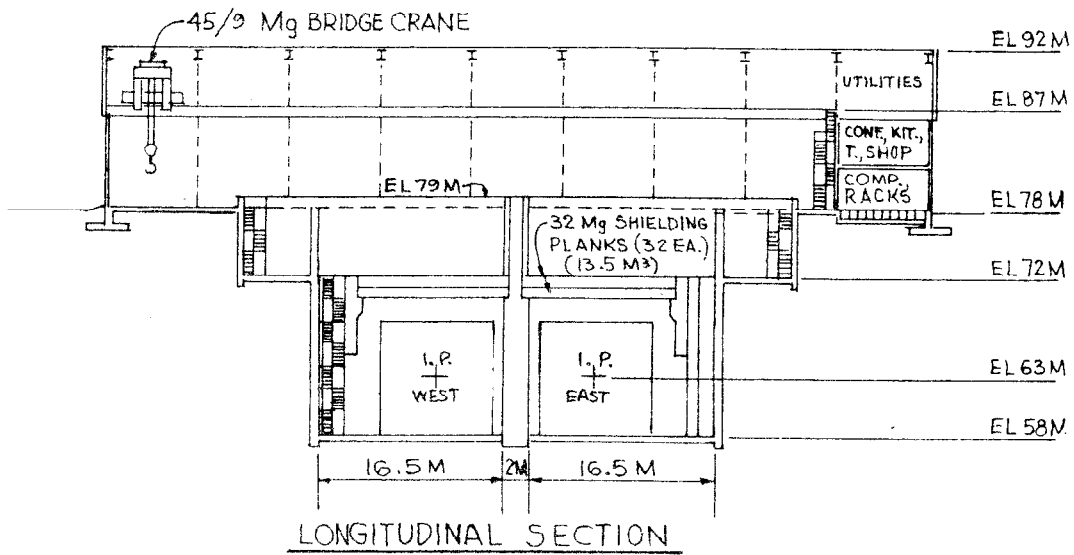
As shown in Fig. 9, each IR is a circular pit vault, 21 m in diameter and 20 m deep. In this design most of the radiation shielding is done by the earth. A single 28 m x 72 m metal building with a traveling crane covers both IR's. The counting houses are inside the building. This version of a 2IR design allows the beam line separation to be reduced to 14 m; which leads to a cost reduction in the construction of the second beam line. Some of the design details are as follows.

(i) Circular Pit Vaults: The floor is at 58 m elevation, 5 m below the beam line. Top shielding for the vault is provided by reinforced, concrete roof beams at the 72 m elevation. These beams are handled by the building crane. The detectors may have to be lowered in pieces to the vault floor and assembled there. The 21 m diameter is fully adequate for the detector size criteria discussed in Sec. 2.

(ii) Counting Houses: The two counting houses are at one end of the building; they consist of two floors plus a roof for service facilities.



PLAN AT ELEV 78 M



LONGITUDINAL SECTION

FIG. 9 PLAN AND ELEVATION VIEWS OF BELOW-GROUND, MINIMUM 21R DESIGN

(iii) Auxiliary Equipment Pits: There are auxiliary equipment pits at each end of the main pits. They are 6 m deep and each has about 120 m² of floor area. They can be used for electronic trailers and/or cryogenic equipment.

d. Below-Ground, Single Staging Area, 2IR Design

Figure 10 shows a variation of the previous design which allows one detector to be assembled off a beam line, or to be moved off that beam line. This allows full access to the final focus system of that beam line in order to do machine studies. The advantage of this, option (d) design over an option (b) design, is that the two beam lines are close together, reducing tunnel costs. The disadvantage is that one detector always surrounds its interaction point. However this is better than option (c) where both detectors always surround their interaction points.

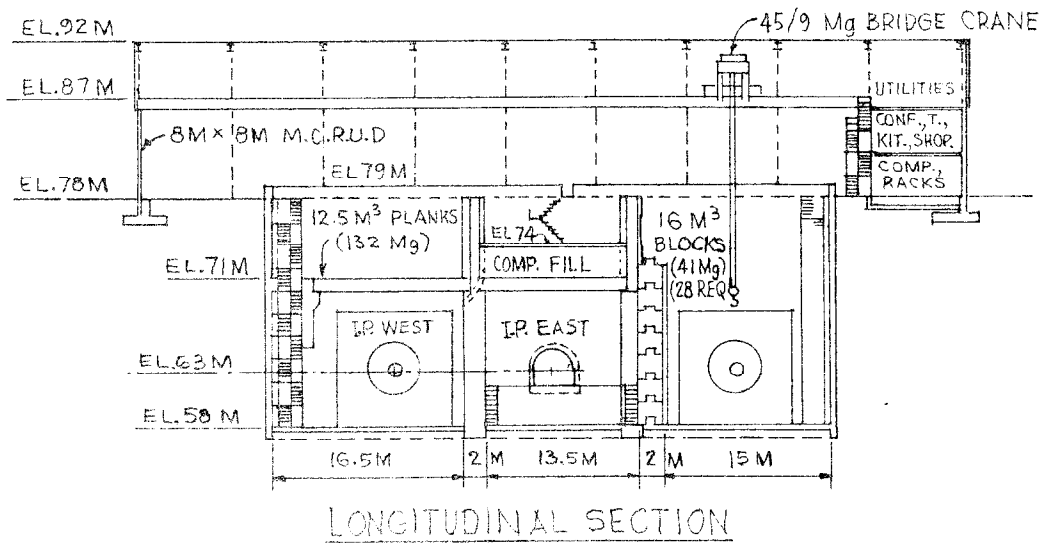
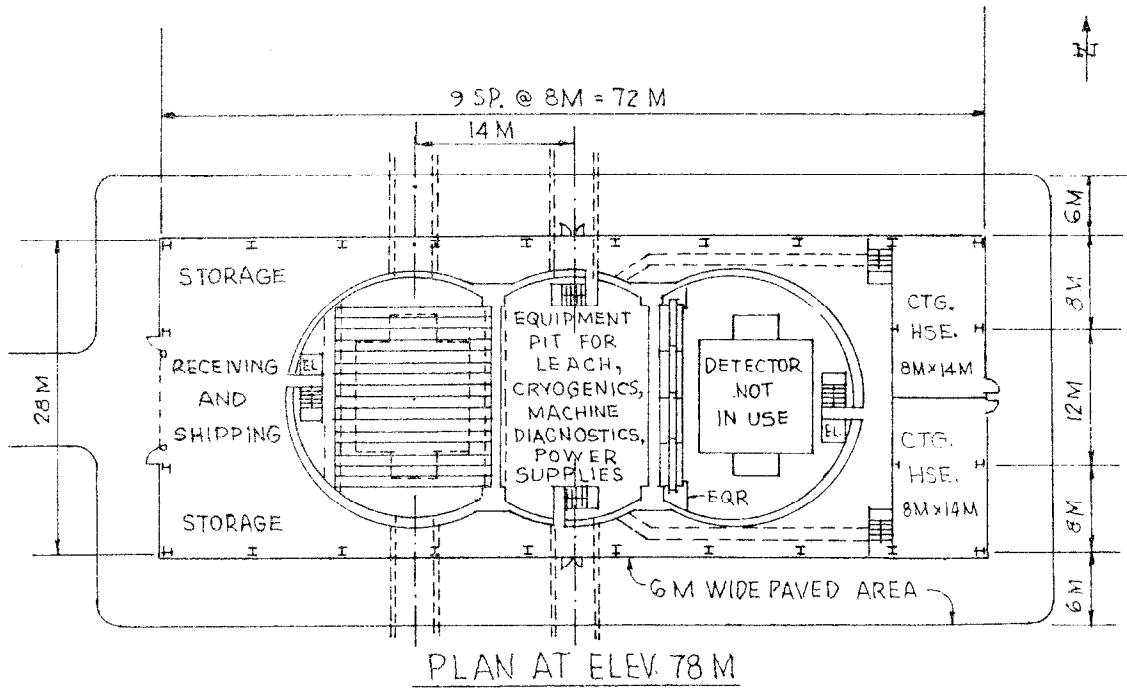


FIG. 10

PLAN AND ELEVATION VIEWS OF SINGLE STAGING AREA, 2IR DESIGN

6. DESIGN COMPARISONS AND SUMMARY

a. Analysis Criteria

The Two Detector Management Subgroup has endeavored to search for and examine a wide range of designs for the experimental areas in order to have as complete as possible a basis on which to make a recommendation. In the preceding two sections seven different conceptual designs have been described. These designs were evaluated with regard to certain criteria we have chosen: i) cost, ii) gain in beam utilization time, and iii) flexibility. The cost includes all incurred costs, directly or indirectly associated with a particular design, and so, for example in the case of various 2IR schemes, it includes costs associated with the second arc tunnel, additional magnets, etc. In the case described in Sec. 4c, it includes the cost of a road between the experimental hall and IR2 where the detector is assembled and tested. The gain in beam utilization time results from more efficient use of the beam, such as during experiment or machine tuneup, detector repair periods, etc. The criterion of flexibility implies the ability to easily change or upgrade experiments, or use the beam for machine studies, thus allowing the physics goals to be dynamic. Ultimately, the choice of design must be based on a judgment of the value of the features ii) and iii) that a particular design offers versus the cost of having those features. The Subgroup has analyzed the seven designs described above using these criteria, and has arrived at the conclusions discussed in this section.

b. Design Comparison

The IR hall designs may be classified by two general properties: i) provision for level access ("roll-in") of detector or assembly of detector in a pit; ii) provision for one interaction point or two interaction points. Examples of each of the four possible combinations of these properties have been described earlier, as well as additional variations. First, we shall discuss the designs with respect to point i).

i) Level Access vs Below-Ground Assembly of Detectors

As discussed in 3b, the cut-and-fill method is needed to provide a roadway to the level where the detector will operate. These level-access schemes are represented by designs 4a, 4b, and 5b(i) in this report

(see Figs.3, 4, 5, and 8). These designs have in common the advantage of the portability into the beam vault of an intact, assembled and checked-out detector. The design 4a is derived from the CDR employing a large T-shaped building to provide a staging area for two large detectors plus one relatively small beam vault, which is well shielded by earth back-fill. In this scheme the detector will have been largely debugged using cosmic rays and is ready for final checkout in the beam line when it is installed. In design 4b, there is provision for only one detector in the assembly area, but there is a road connecting the single SLC IR region to IR2 at PEP, where check-out could be done under actual colliding beam conditions in the PEP beam line. In this case the detector is expected to reach a higher level of readiness than in the design 4a, but nevertheless will not be tested in the physics or background environment of the SLC IR. Design 5b(i) has level access and two IR's, with a staging area for one large detector between the beam vaults. As with design 4a, the detectors will be debugged on cosmic rays, and then installed in the beam line. Since the assembly area is restricted to one detector the detector installations will be done serially, but this presents no particular difficulties since one detector can begin running in the beam while the second is being assembled and checked out. The advantages deriving from having two IR's rather than one will be discussed below.

Common to all the level access designs is the cut-and-fill construction method, with its associated large cost of earth-moving to reach the design floor level of about 60 m starting from ground level of about 90 m. The volume of material to be moved is large because of the excavation for both the experimental hall and the access road. The situation is somewhat aggravated by the poor strength of the underlying material, requiring a relatively shallow cut in order to prevent earth slippage, and thus requiring a larger excavation volume. Moreover, the design of the experimental hall must allow for wall thickness sufficient to hold a large burden of earth that is backfilled against the vault as radiation shielding, resulting in an additional cost.

These cost factors can be considerably reduced by adopting a quite different approach, but at the sacrifice of the level access. In this alternate method circular holes or pits of about 21 m diameter are excavated

vertically, which then form the walls of the beam vault or assembly area (see Figs. 6, 9, and 10). The shafts are sunk from a level excavated to a depth of about 80 m. The cost reduction, as compared with the level access designs, is a result of: the much smaller volume of excavated material from the experimental hall by use of the vertical shafts; the relatively thin concrete shaft walls which exploit the natural strength of the circular shape; the very thin walls and roof of the above-ground building, which has no loading or shielding requirements; and the excavation for the access road, which is much reduced because it is constructed much closer to ground level. The penalty for the cost reduction is that detectors must be assembled and checked out in the underground areas.

ii) One vs Two Interaction Regions: Examples of designs for one IR are described in Sec. 4 (Figs. 3, 4, 5, and 6), and for two IR's in Sec. 5 (Figs. 8, 9, and 10). It is apparent from Fig. 1 that with two IR's, there are additional costs incurred for the tunnels, beam transport and final focus magnets associated with the second arc. There are other costs as well, such as two beam switching regions, additional beam dumps, instrumentation, etc. Assuming two detectors are to be accommodated in the experimental hall, there is only a small increase in the cost of a hall containing two IR's rather than one IR. Many operational gains are achieved, however, through the ability to switch the beam collision point from one IR to the other in a short time period, of the order of one day.

There is also considerable advantage in having a staging area adjacent to an IR. During the initial running periods of the SLC, the availability of two IR's plus staging area makes it possible to set up the first detector next to one IR while the beam line is completed and debugged. Once the beam is tuned so adequate luminosity is available for physics, the detector is inserted and debugged while the second beam line is readied for further machine studies.

After completion of the beam tests, the second detector can be installed, and the luminosity can be shared between the detectors. In the initial tune-up period, only a fraction of the beam time will be needed by a detector for check-out. The tune-up will extend until the background rejection is sufficient and the data quality is acceptable. The remaining fraction of the beam time may then be used by the first detector, or for beam studies.

After the initial tune-up, in the steady-state operating mode, there are still substantial gains in utilization of beam time achieved by the two IR designs compared to the one IR design. Some of these gains occur when a new detector is being installed, since the beam can be turned over to the other region during the necessary access periods for that new detector. These gains also occur when a detector breaks down. Although detectors will be designed to be able to continue data collection in spite of minor component failures, there will be some unavoidable shutdowns for repairs, and during these periods, the beam time otherwise wasted can be utilized by the other IR. In one exercise which analyzed the use of beam time, an increase of productive beam time usage of about 35% was predicted for the first two years of SLC operation with the two IR design relative to the one IR design. This exercise was based on the length of the tune-up periods for the present PEP detectors.

When both detectors are in the full production mode, it will be beneficial to the physics program for the detectors to share luminosity for data collection. Experiments with different and complementary detection capabilities will, through this time sharing, achieve a more complete and accurate understanding of the new physics.

Thus the overall flexibility in beam time-sharing provided by the 2IR design allows experiments to be interchanged or upgraded without loss of beam utilization time, not just during the usual scheduled shutdown periods, but at any time when it is most beneficial to the overall program. Such changes may indeed be motivated by early physics results at the SLC (or elsewhere), the changing emphasis on physics goals, and the differing capabilities of the detectors at the SLC.

c. Summary

The need to have provision for two or more detectors at the SLC is clear from the variety and importance of the anticipated physics results and the expressed interest of the High Energy Physics Community. The charge to this Subgroup is to find the optimal utilization of the SLC with two detectors. The criteria of cost, optimization of productive time, and flexibility of operation form the basis for the Subgroup's recommendations.

A variety of arrangements and construction methods have been explored, and certain concepts and designs have emerged. First, the underground location of the beam vaults and assembly areas have important cost advantages over the level access experimental hall, independent of whether the hall encloses one or two interaction regions. Second, the SLC design incorporating two arcs and two interaction regions affords an increase in efficiency of beam use, as well as enhanced flexibility in the operation of the program. For example, beams can be switched between IR's for machine development and tests, for installation, removal, upgrade or repair of experiments, or to let two complementary experiments alternate in collection of data. Experiments can be replaced, serviced or improved at any time during the year while operations continue. Although the 2IR option obviously adds to the initial cost, the estimated improvement in efficiency is expected to offset this increased cost early in the SLC program. It has been assumed in the 2IR scenarios that the switch-over between arcs can occur without a major retuning effort, i.e., in a time period of the order of a day.

The SLC is likely to begin operations in a highly competitive atmosphere. There will be a premium on obtaining results soon after usable luminosity is achieved. Some delay in SLC turn-on can be expected due to construction of the second arc; but with proper programming of construction work, that delay can be minimized and probably more than made up for by the gains in operating efficiency early in the SLC program.

To summarize, the Two Detector Management Subgroup has examined seven alternative designs for the experimental hall allowing operation of at least two detectors. The designs which emerge as the best under these criteria are those incorporating two SLC interaction regions (Fig. 1b). In the opinion of this Subgroup the extra costs are more than balanced by the increases in efficiency and flexibility.

Based on the present geologic and engineering information, the technique of digging vertical pits for the interaction regions appears favorable compared with the cut-and-cover method. There are three such

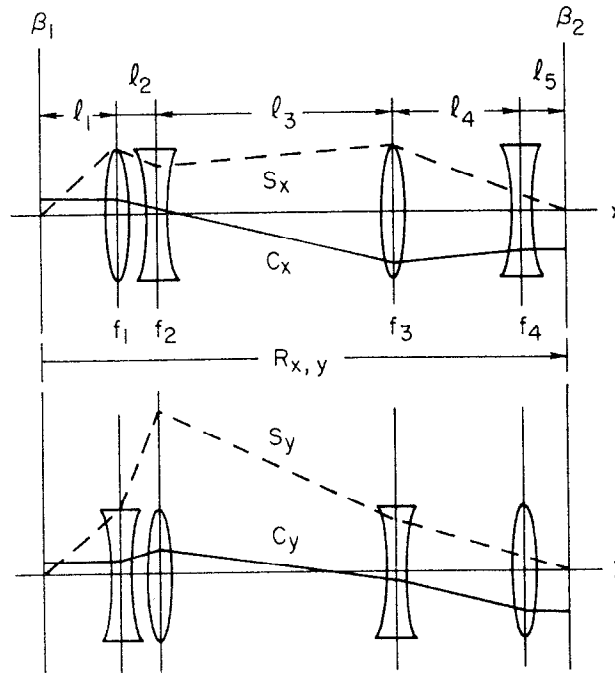
designs in this report: one with just two IR's, and the others having the two IR's plus an assembly area accessible to at least one of the IR's. The Subgroup finds these three designs acceptable within the scope of their studies.

The existence of an assembly area adjacent to an IR is highly desirable for construction of detectors, quick replacement of experiments, and the ability to withdraw a working experiment to allow beam studies. The design of Sec. 5d is estimated to require virtually no cost increase compared with that of Sec. 5c which lacks this feature. The shared staging area design of Sec. 5b(ii) has the additional benefits of greater flexibility and of putting the detectors on an equal basis. This Subgroup endorses these designs which incorporate two interaction regions with an adjacent assembly area.



Participants at the initial meeting of the SLC Workshop in March, 1981, confer outside the auditorium at Stanford University. Two similar meetings were held at SLAC in the summer and in late December. Much of the work took place in the smaller sessions which the eight working groups held monthly during the year.

INTERACTION REGION

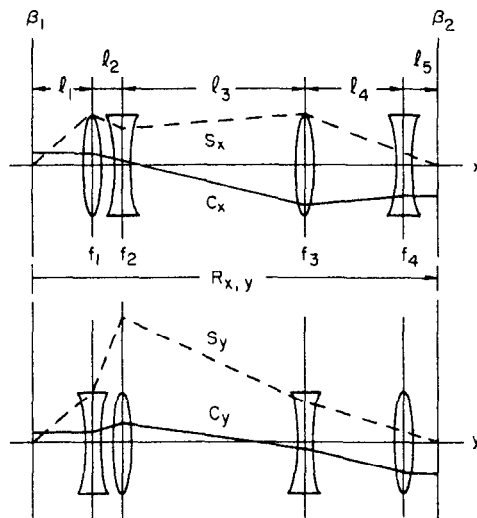


$$R_{x,y} = \begin{bmatrix} -M_x & 0 & & \\ 0 & -\frac{1}{M_x} & & \\ & & -M_y & 0 \\ & & 0 & -\frac{1}{M_y} \end{bmatrix} = \begin{bmatrix} -\sqrt{(\beta_2/\beta_1)_x} & 0 & & \\ 0 & -\sqrt{(\beta_2/\beta_1)_x} & & \\ & & -\sqrt{(\beta_2/\beta_1)_y} & 0 \\ & & 0 & -\sqrt{(\beta_2/\beta_1)_y} \end{bmatrix}$$

12-80
3814840

A TELESCOPIC MODULE

INTERACTION REGION



$$R_{x,y} = \begin{bmatrix} -M_x & 0 & & 0 \\ 0 & -\frac{1}{M_x} & & 0 \\ & & -M_y & 0 \\ & & 0 & -\frac{1}{M_y} \end{bmatrix} = \begin{bmatrix} -\sqrt{(\beta_2/\beta_1)_x} & 0 & & 0 \\ 0 & -\sqrt{(\beta_2/\beta_1)_x} & & 0 \\ & & -\sqrt{(\beta_2/\beta_1)_y} & 0 \\ & & 0 & -\sqrt{(\beta_2/\beta_1)_y} \end{bmatrix}$$

12-80
281-8-0

A TELESCOPIC MODULE

I. INTRODUCTION

The Interaction Region Group addressed the basic questions of how to collide the SLC beams, how to maximize and monitor the luminosity, and how to minimize the detector backgrounds at the interaction region. In practice, five subgroups evolved to study these questions.

(a) The final focus group provided three alternative designs to achieve the 1-2 micron beam spot size required by the SLC, as well as studying other problems including: η, η' matching from the collider arcs, the implementation of soft bends near the interaction region, beam emittance growth, and magnet tolerances in the final focus.

(b) The beam position monitor group proposed two devices, a strip line monitor, and a beamstrahlung monitor, to bring the beams into collision.

(c) The luminosity monitor group reviewed the possible QED processes that would be insensitive to weak interaction (Z^0) effects.

(d) The beam dumping group proposed locations for kicker and septum magnets in the final focus that would achieve a high dumping efficiency and would meet the desired beam tolerances at the Møller scattering target in the beam dump line. Working with the Polarization Group, the Møller experiment was designed into the beam dump beam line. A beam dump was proposed that would maintain radiation backgrounds (penetrating muons) at acceptable levels.

(e) The detector backgrounds group proposed "soft-bend" and masking configurations to shield the detector from synchrotron radiation from the hard/soft bends and from the final focus quadrupoles and evaluated the effectiveness of these designs for the three final focus optics designs. Backgrounds were also estimated from: large angle synchrotron radiation, local and distant beam-gas interactions, 2-photon interactions, and from neutrons and backscattered photons from the beamstrahlung dump.

Two additional subgroups formed to study related questions.

(a) The e^-e^- group summarized e^-e^- physics and proposed alternative designs for several elements of the SLC to allow for the option of colliding e^-e^- beams. A separated beam dump and polarization monitor for e^-e^- operation was also proposed.

(b) The (SmCo_5) permanent magnet group studied magnetic field mapping, designs for adjusting the field strengths of SmCo_5 quadrupoles, and (with the Final Focus group) the tolerances required from the permanent magnet quadrupoles.

The results of these studies are a significant advance on the work in the SLC Conceptual Design Report -- "the Red Book". The detailed reports of the seven subgroups follow in Sections II through VIII of this report.

II. THE COLLIDER FINAL FOCUS SYSTEM

A. Introduction

The function of the final focus system (FFS) is to transform the beam envelope at the end of the collider arc to the small size needed for high luminosity beam collisions at the interaction region. The minimum beam size achievable is determined by the emittance and momentum spread of the beam and the optical quality of the final focus optics. In particular, the second-order chromatic aberrations resulting from the finite momentum spread in the beam must be reduced to an acceptable level.

Two basic approaches have been used to achieve the above objectives.¹ The first is to design an optical system having small path length differences between the monoenergetic trajectories so that no chromatic corrections are needed. The second method is to correct for the second-order chromatic aberrations by introducing dipoles and sextupoles into the solution. The ultimate performance is then determined by the residual third order geometric and/or chromatic aberrations introduced by the sextupoles.

The beam parameters which dominate the design of the FFS are the beam emittance, ϵ , the maximum design energy, E (max), the momentum spread of the beam, dp/p , the rms beam size at the interaction point, σ^* , and the maximum beam disruption angle, θ_d , resulting from the beam-beam collisions.

The following values for these beam parameters are assumed for the purpose of this report:

$$\epsilon = 3 \times 10^{-10} \text{ rad-meters}$$

$$E \text{ (max)} = 60 \text{ GeV}$$

$$(dp/p) < \pm 0.5\%$$

$$\theta_d < 2.5 \text{ mrad for } \sigma^* = 1.2 \text{ microns}$$

$$(\theta_d < 1.0 \text{ mrad for } \sigma^* = 1.8 \text{ microns}).$$

B. Beam Optics

1. The Basic Building Blocks for the FFS

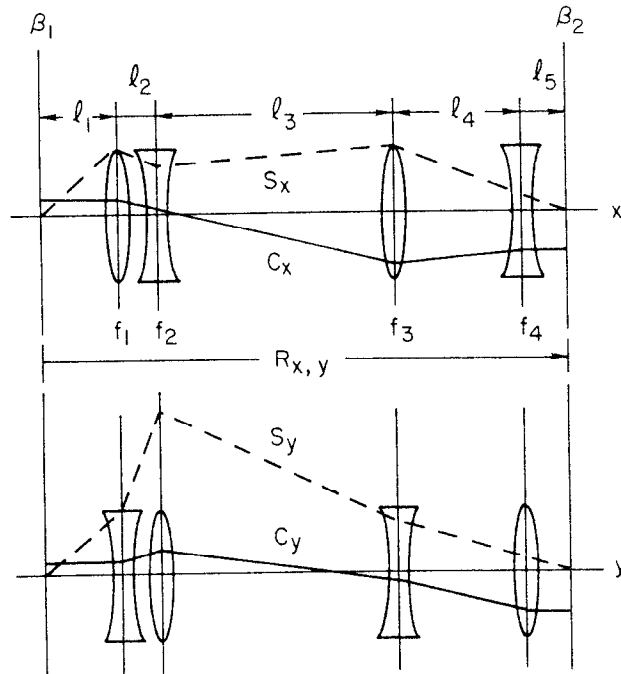
Telescopic modules, similar to the one illustrated in Fig. 1, are used as the basic building blocks for the design of the final focus systems discussed in this report. The telescopic systems used provide simultaneous parallel to parallel and point to point imaging in both transverse planes. A sequence of several such modules has the important property that it minimizes the maximum amplitudes of the characteristic sine-like and cosine-like trajectories, which are two independent solutions of the second-order differential equation describing the linear optics. Since higher order aberrations are a function of the amplitudes of these trajectories, then using a sequence of telescopic modules for the FFS tends to minimize the magnitude of the higher order optical distortions. The first-order transformation matrix, as shown in Fig. 1, is particularly simple; the notation used is that of TRANSPORT:²

$$\begin{array}{ll}
 (x|x_0) = R_{11} = C_x & (y|y_0) = R_{33} = C_y \\
 (x|x'_0) = R_{12} = S_x & (y|y'_0) = R_{34} = S_y \\
 (x'|x_0) = R_{21} = C'_x & (y'|y_0) = R_{43} = C'_y \\
 (x'|x'_0) = R_{22} = S'_x & (y'|y'_0) = R_{44} = S'_y
 \end{array}$$

The matrix elements R_{11} and R_{33} are equal to the optical magnifications, M :

$$R_{11} = M_x = \sqrt{(\beta_2/\beta_1)_x} \quad ; \quad R_{33} = M_y = \sqrt{(\beta_2/\beta_1)_y}$$

for the telescopic module, where 1 and 2 are the beginning and end points of the module. For the x-plane the condition $R_{12}=0$ is equivalent to the point to point imaging property and $R_{21}=0$ is equivalent to parallel to parallel imaging. When both R_{12} and R_{21} are equal to zero, the orientation of the phase ellipse is an invariant, i.e., the Courant-Snyder parameter alpha is the same at the end of the system as it is at the beginning. For example, an upright ellipse transforms to another upright ellipse (i.e., waist to waist imaging). For this case the monoenergetic beam envelope size of the beam is given by:³



$$R_{x,y} = \begin{bmatrix} \begin{bmatrix} -M_x & 0 \\ 0 & -\frac{1}{M_x} \end{bmatrix} & 0 \\ 0 & \begin{bmatrix} -M_y & 0 \\ 0 & -\frac{1}{M_y} \end{bmatrix} \end{bmatrix} = \begin{bmatrix} -\sqrt{(\beta_2/\beta_1)_x} & 0 \\ 0 & -\sqrt{(\beta_2/\beta_1)_x} \\ -\sqrt{(\beta_2/\beta_1)_y} & 0 \\ 0 & -\sqrt{(\beta_2/\beta_1)_y} \end{bmatrix}$$

12-80
3814840

A TELESCOPIC MODULE

Fig. 1. Example of a telescope module.

$$\sigma_x = \sqrt{\beta_x \epsilon}$$

and the angular spread is:

$$\sigma_{x'} = \sqrt{\epsilon / \beta_x} \quad .$$

Analogous relations apply to the y-plane optics.

2. Computational Tools Available for the Design

The following computer programs have been used to assist in the design of the final focus systems: TRANSPORT,² TURTLE,⁴ GIOS,⁵ and a differential ray tracing program.⁶

TRANSPORT is a second-order matrix multiplication program for designing the first and second-order optics of a proposed system. It is used to determine the quadrupole strengths needed for the first-order optics and the sextupole strengths required to minimize the second-order chromatic distortions introduced by the quadrupoles.

TURTLE is an efficient ray tracing program that uses the second-order matrices from TRANSPORT to represent each element of the system. Individual rays are traced through each element separately so that higher-order cross coupling terms between elements are not truncated in the computation, in contrast to TRANSPORT which truncates each matrix multiplication to second order. For example, the third order cross coupling between sextupoles is not truncated as the rays are traced through the system. The TURTLE results are displayed in the form of histograms which show the density distribution of N rays traced through the system as a function of any of the phase space coordinates.

GIOS is a matrix multiplication program, similar to TRANSPORT, except that it has third-order capability in the x-plane. GIOS provides an efficient computation of the third order aberration coefficients in the x-plane.

Ultimately all of the FFS solutions are checked by a differential ray tracing program. This program includes the fringing fields of all of the magnetic elements comprising the system. Its main purpose is to provide an independent check on the results obtained with TURTLE and GIOS and to provide information on other higher order distortions not calculated by TURTLE or GIOS.

3. Chromatic Aberration Theory

The second-order chromatic aberrations introduced by the quadrupoles are a dominant factor in the design of a final focus system. If midplane symmetry is preserved in a beam transport system, then the following second-order chromatic aberrations may be non-zero. The allowed aberrations for the x-plane are $(x, x\delta)$, $(x, x'\delta)$, and $(x, \delta\delta)$, and for the y-plane $(y, y\delta)$, and $(y, y'\delta)$ are allowed, where δ means dp/p . Using TRANSPORT notation, the above aberration coefficients have the following equivalents. $T(1\ 16) = (x, x\delta)$, $T(1\ 26) = (x, x'\delta)$, $T(1\ 66) = (x, \delta\delta)$, $T(3\ 36) = (y, y\delta)$, and $T(3\ 46) = (y, y'\delta)$. Of these, $(x, x\delta)$ and $(y, y\delta)$ are unimportant for the FFS because of the small values of the phase space parameters x and y of the beam and because telescopic modules are used as the basic building blocks. $(x, \delta\delta)$ is identically zero for an all quadrupole FFS and can be made to vanish for a system containing dipoles by choosing the appropriate optical arrangement of the dipoles.

This leaves $(x, x'\delta)$ and $(y, y'\delta)$ as the two principal second-order chromatic aberrations limiting the performance of the FFS. Both aberrations can be made to vanish by the introduction of dipoles and sextupoles into the optics of the system. From Ref. 7 or Ref. 8 the magnitude of these two aberrations, before sextupole corrections are made, can be calculated by an integral over the length of the FFS. The result is the following:

$$T_{126} = M_x \int (s'_x)^2 ds = \sqrt{\left(\frac{\beta_2}{\beta_1}\right)_x} \int_1^2 (s'_x)^2 ds = \sqrt{\left(\frac{\beta_1}{\beta_2}\right)_x} \int_2^1 (s'_x)^2 ds$$

$$T_{346} = M_y \int (s'_y)^2 ds = \sqrt{\left(\frac{\beta_2}{\beta_1}\right)_y} \int_1^2 (s'_y)^2 ds = \sqrt{\left(\frac{\beta_1}{\beta_2}\right)_y} \int_2^1 (s'_y)^2 ds$$

(1)

where 1 and 2 are the beginning and the end points of the FFS. Note that the values of these particular aberration coefficients are independent of the direction of the integration.

The integrals in the above equations are related to the second-order path length differences between the monoenergetic particles and the central trajectory, normalized to the square of their initial angle, as follows:

$$\frac{2\Delta\ell}{(x'_0)^2} = \frac{2}{(x'_0)^2} \int_1^2 [1 - \cos x'(s)] ds \approx \int_1^2 \left[\frac{x'(s)}{x'(0)} \right]^2 ds = \int_1^2 (s'_x)^2 ds$$

$$\text{where } \frac{\Delta\ell}{(x'_0)^2} = T_{522} \quad .$$

So

$$2T_{522} = \int_1^2 (s'_x)^2 ds$$

and similarly:

$$2T_{544} = \int_1^2 (s'_y)^2 ds$$

(2)

where T(5 22) and T(5 44) represents the TRANSPORT notation used for these path length aberration coefficients. For a "non-corrected" system, the overall beam size is minimized by equating the monoenergetic beam size at the interaction point to the magnitude of the second order chromatic distortion. For telescopic systems having waist to waist imaging, this condition yields the equation:

$$\sigma_x^* = \sqrt{\beta_x^* \epsilon} = \left(x'_L \frac{\Delta p}{p} \right) T_{126} = \left(\sqrt{\frac{\epsilon}{\beta_L}} \right)_x \left(\frac{\Delta p}{p} \right) \sqrt{\left(\frac{\beta_L}{\beta^*} \right)_x} \int_*^L (s'_x)^2 ds$$

where "*" is at the interaction point (IP), and "L" is at the (lattice) input to the final focus. Simplifying, one obtains:

$$\beta_x^* = \left(\frac{\Delta p}{p} \right) \int_*^L (s'_x)^2 ds = 2 \left(\frac{\Delta p}{p} \right) T_{522}$$

and similarly:

$$\beta_y^* = 2 \left(\frac{\Delta p}{p} \right) T_{544}$$

(3)

where for the above equations T(5 22) and T(5 44) are evaluated from the IP to the collider arc using TRANSPORT.

If no second-order chromatic corrections are made to the system, the above equations define the practical lower limits for β^* that may be achieved. (Note that the effective rms beam size is $\sqrt{2}$ larger than the monoenergetic beam size because both the monoenergetic beam size and the 'chromatic beam size' are contributing to the total beam size at the interaction point.)

For a chromatically corrected system, the magnitudes of T(5 22) and T(5 44), evaluated with the sextupoles turned off, are a measure of the degree of success to be expected from a system when the sextupoles are turned on. That is, the smaller their values are, the better the system will perform. This has been substantiated by comparing the results for the final focus systems that have been studied to date.

4. Third Order Aberrations

If a system is chromatically corrected to second-order then the third order aberrations introduced by the sextupoles are the principal source of the residual optical distortions limiting the system's performance. For the final focus systems considered in this report, the dominant third order aberrations in the x-plane are the geometrical terms $(x,x'x'x')$ and $(x,x'y'y')$ and the chromatic terms $(x,x'\delta\delta)$ and $(x,y'y'\delta)$. The magnitude of these aberration coefficients were evaluated by the computer program GIOS, and independently with the differential ray tracing program. Similar aberrations exist in the y-plane.

The ratios of the relative magnitudes of the third order chromatic aberrations to the third order geometric aberrations is a function of the strength of the dipoles used for the second order chromatic corrections. By adjusting the dipole and sextupole strengths in inverse proportions, the third order optical distortions can be minimized without disrupting the second order chromatic correction. This minimum value for the third order occurs when the angular dispersion introduced by the dipoles is approximately equal to the monoenergetic angular spread in the beam (at the dipole). This is expressed by the equation:

$$d'_x \left(\frac{\Delta p}{p} \right) = \sqrt{\frac{\epsilon}{\beta_D}}$$

(4)

and

$$d'_x = \alpha$$

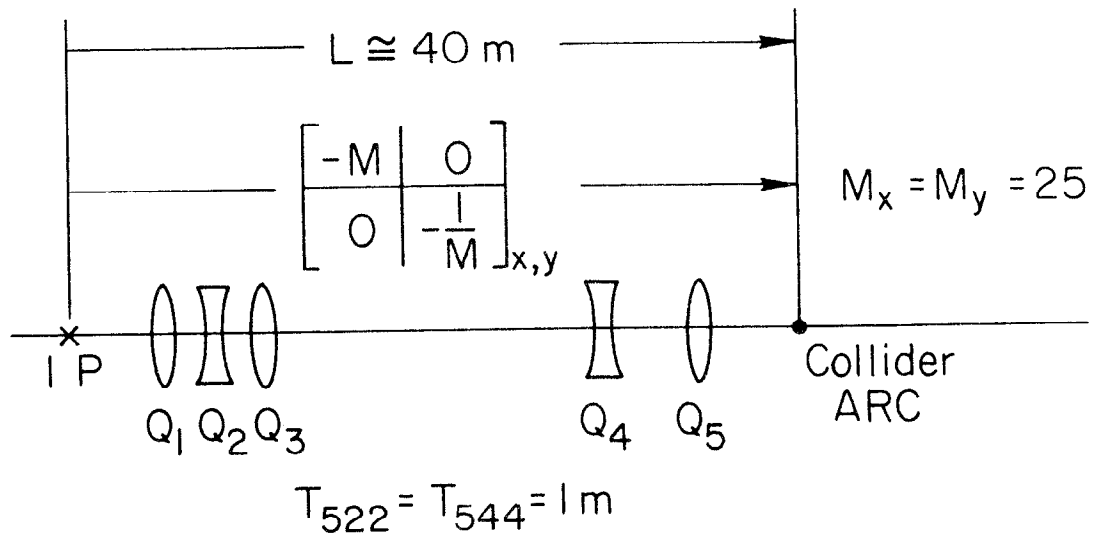
where α is the angular dispersion introduced by the dipole, and β_D is the value of β_x at the dipole. The final adjustment of the strengths of the dipoles is obtained by observing, in computer simulations, the relative optical distortions introduced by the sextupoles for a monoenergetic beam vs those for a beam having a momentum spread of dp/p . It is typically found that the optimum value for α is within 20 percent of that given by the above equation.

C. Possible FFS Solutions

Three types of final focus solutions have been studied, the MICROQUAD, the REDBOOK, and the MINIQUAD. The microquad system is designed to have small values for the second-order path length matrix elements $T(5\ 22)$ and $T(5\ 44)$. It has no chromatic corrections. The redbook solutions have a drift of 3-4 meters from the IP to the first quadrupole in the system. This results in relatively large values for $T(5\ 22)$ and $T(5\ 44)$, so second order chromatic corrections are necessary. The miniquad solution has a small drift (25 cm) to the input face of the first quadrupole. This results in relatively modest values for $T(5\ 22)$ and $T(5\ 44)$. But, in addition, it has second-order chromatic corrections. As a consequence it yields the smallest rms beam size at the IP among the three types of systems that have been studied. A tabulation of $T(5\ 22)$ and $T(5\ 44)$ for the three systems is given in Table I.

1. The Microquad Final Focus System

The microquad FFS, shown in Fig. 2, is composed entirely of an array of quadrupoles, forming a single telescopic system, which transforms the beam envelope at the end of the collider arc to a size suitable for high luminosity beam collisions at the interaction point. There are no dipoles or sextupoles used in this system. The first order optics are adjusted to transform the beta function at the end of the collider arc, β_L , to the



12-81

MICROQUAD FFS

4177A82

Fig. 2. Microquad final focus system.

TABLE I
Path Length Comparisons for the three different final focus systems

Systems	$T_{522}(\text{m})$	$T_{544}(\text{m})$	Function
MICROQUAD FFS	1.0 m	1.0 m	β matching only
MINIQUAD and IMINIQUAD FFS	4.7 6.9 ~0	4.5 7.2 ~0	β matching only β matching + chromatic section sextupoles off sextupoles on
Superconducting Redbook FFS	3.8 7.9 ~0	13.2 35 ~0	β matching only β matching + chromatic section sextupoles off sextupoles on

desired value of β^* at the IP. The minimum practical β^* that can be achieved is determined by the second-order chromatic aberration's ($x, x'\delta$) in the x-plane and ($y, y'\delta$) in the y-plane. If the monoenergetic beam size at the IP is equated to the chromatic distortions caused by the above aberrations, then the minimum practical β^* is given by Eq. (3) above. The smallest values of $T(5\ 22)$ and $T(5\ 44)$ that have been achieved to date for the microquad FFS is 1 meter. If $dp/p = \pm 0.5\%$, this yields a value for β^* of 10 mm. The resultant rms beam envelope size at the IP, including the contribution from the chromatic aberrations, is then obtained by folding the monoenergetic beam envelope with the chromatic beam envelope at the IP. The result, extracted from a TURTLE calculation, is shown in Fig. 3 to have an rms value of 2.0 microns.

For the microquad FFS the values of $T(5\ 22)$ and $T(5\ 44)$ were adjusted to be equal and minimized using the TRANSPORT program. This was achieved by placing the strongest practical quadrupole as near to the interaction point as is feasible and immediately following it with other quadrupoles so as to minimize the path length differences in both the x and y transverse planes. Although a trial and error method was used the process

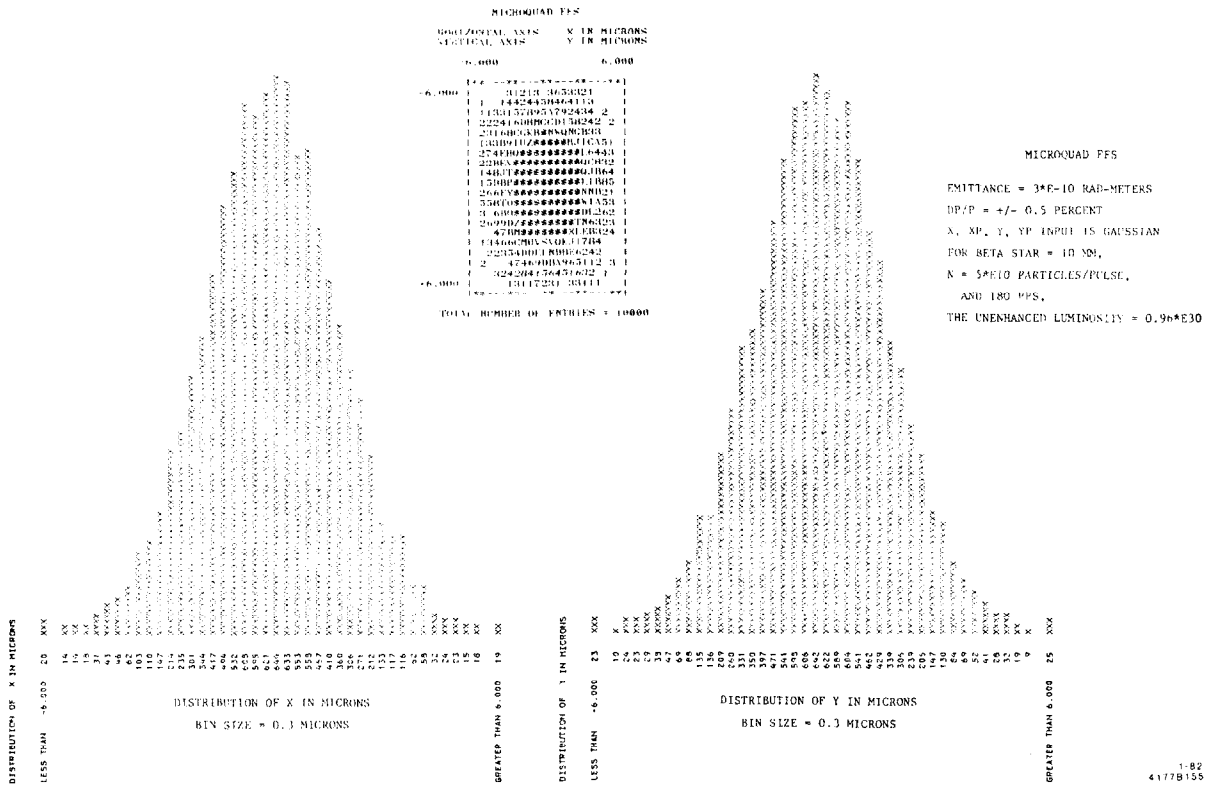


Fig. 3. Microquad FFS beam distribution at the IP.

converged rapidly. The array of quadrupoles, constituting the system, is given in Table II. The first quadrupole has an aperture of ± 0.8 mm and a field strength at the pole of 13 kG. It is believed that this can be achieved with SmCo_5 permanent magnet quadrupoles. The subsequent 2 or 3 quadrupoles are also assumed to be constructed in a similar manner since they must all be located inside the detector. Another possible method of fabrication is to make these elements superconducting iron-free quadrupoles.

The principle limitation to the minimum achievable β^* of the microquad FFS is the magnitude of the angular spread in the disrupted beam resulting from the beam-beam interaction. This is called the disruption angle, θ_d . For a β^* of 10 mm, θ_d is less than 1 mr. This determines the size of the aperture of all of the quadrupoles in the microquad FFS array. For the SmCo_5 permanent magnet material, the peak pole field that is presently obtainable is 14-15 kG. This combined with θ_d then determines the maximum strength quadrupole that can be fabricated. The present microquad system has been designed at this limit.

TABLE II
Microquad FFS component values at 50 GeV

ELEMENT		LENGTH	POLE FIELD	APERTURE RADIUS
P = 50 GeV/c		meters	kGauss	mm
(THE INTERACTION POINT IS HERE. BETA STAR = 10 mm)				
DRIFT		0.20000;		
QUAD	"Q1 "	0.30000	13.00000	0.80000;
DRIFT		0.02500;		
QUAD	"Q2 "	0.31000	-12.91507	1.50000;
QUAD	"Q2 "	0.45000	-12.91507	2.50000;
DRIFT		0.07500;		
QUAD	"Q3 "	0.26000	12.96884	3.25000;
QUAD	"Q3 "	0.31000	12.96884	4.00000;
DRIFT		24.72841;		
QUAD	"Q4 "	1.00000	-3.51325	20.00000;
DRIFT		3.47814;		
QUAD	"Q5 "	1.00000	2.91105	20.00000;
DRIFT		5.00000;		
(BEGINNING OF THE COLLIDER ARC)				

2. Redbook Type Solutions for the Final Focus

Another class of FFS solutions is illustrated in Fig. 4. These are the "redbook type," so called because the first of these was reported in the red colored SLAC linear collider conceptual design report, Ref. 9. (Note that for the redbook optics only the IP is on the right, of Fig. 4, and the collider lattice, input to the final focus, is on the left.) The distinguishing feature of this class of final focus systems is that they provide a sufficient drift space between the interaction point and the first quadrupole in the system to permit all of the components of the FFS to be external to the detector. This implies a large value for the sum of the path length matrix elements;⁹ that is:

$$(T(5\ 22) + T(5\ 44)) > 2(L(1) + L(2))$$

where $L(1)$ is the distance to the center of the first quadrupole from the interaction point, and $L(2)$ is the distance between centers of the first and second quadrupoles. Because of this the optical distortions are expected to be greater than those of the miniquad system. This conclusion is substantiated by the ray tracing results.

Four telescopic modules are used for this solution. The first two modules are identical but arranged in mirror symmetry as illustrated in Fig. 4. These first two modules form the second-order chromatic correction system. The third and fourth modules match the β^* at the IP to the collider arc. Contained within each of the first two modules are two sextupoles, one for the x-plane and one for the y-plane, which correct for the principal second-order chromatic aberrations $T(1\ 26) = (x, x'\delta)$ and $T(3\ 46) = (y, y'\delta)$. Dipoles are inserted to introduce an appropriate dispersion function. The first dipole is positioned between modules 1 and 2, a second between modules 3 and 4, and a third one at the end of module 4 next to the collider arc. The strength of the first dipole is chosen so as to provide the proper balance between the residual third-order geometric and chromatic aberrations, see Eq. (4). This occurs when the chromatic beam size is approximately equal to the monoenergetic beam size at the correction sextupoles. The second and third dipoles are chosen so as to make the dispersion function symmetrical about the first

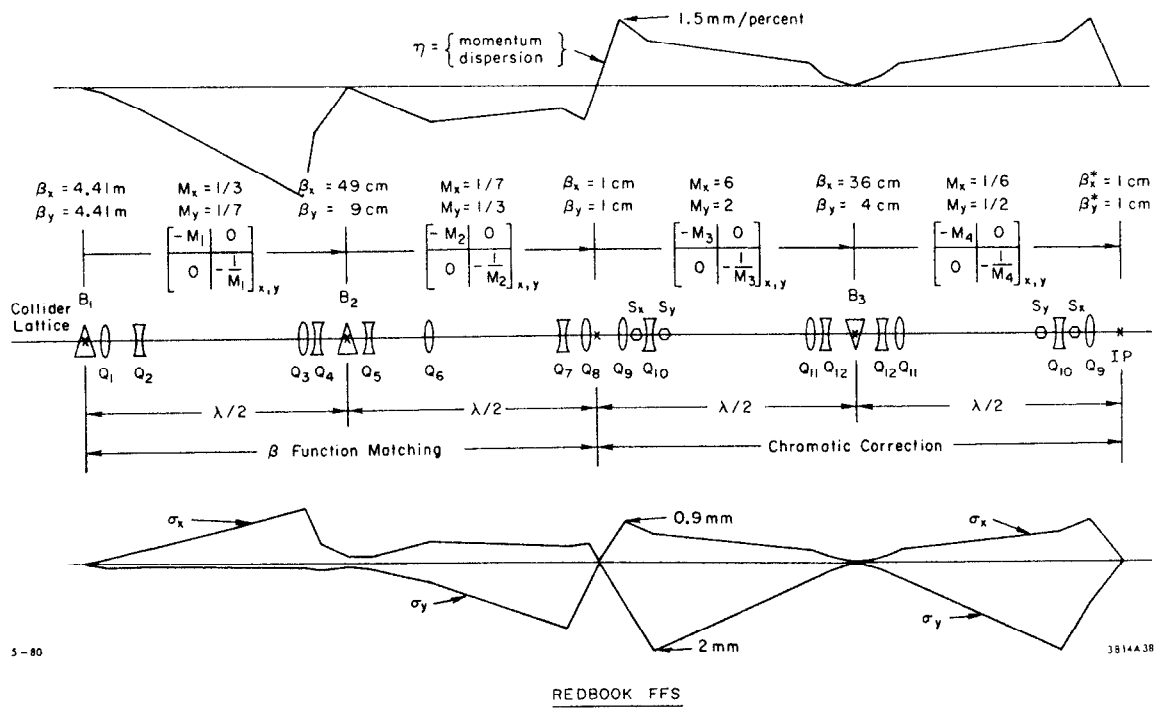


Fig. 4. "Redbook" type final focus system.

dipole and to make the dispersion vanish to second order in dp/p at the interaction point.

Two such systems have been studied. The first, using room temperature magnets, was reported in Ref. 9. This system was designed for a $\beta^* = 10$ mm. A second system using superconducting quadrupole elements has been designed for a monoenergetic β^* of 5 mm. A TRANSPORT listing of these systems is given in Tables IIIa,b. The superconducting quadrupoles are required for the 5 mm β^* because the disruption angle stay-clear is 2.5 mr. This increases the required aperture of all of the quadrupoles and hence the pole tip field. While the field requirements are modest for superconducting quadrupoles, they are clearly excessive for normal room temperature elements. Histograms of the results obtained for these systems are shown in Figs. 5(a),(b). As can be seen, the results are inferior to those obtained for the miniquad FFS. While it is believed that some improvement can be achieved for systems of this type, it is not expected that they can compete with the quality of the miniquad solutions described below.

3. The Miniquad Final Focus System

The optical arrangement of the miniquad FFS is shown in Fig. 6. It consists of four telescopic half wave modules. The first and fourth modules match the beta function at the IP to the collider arc. The second and third modules are used for the second-order chromatic corrections of the FFS.

Beginning at the interaction point, the first module has optical magnifications of 5 and 3 in the x and y planes respectively. These particular values were chosen so as to minimize the total length of the FFS system and so that the emittance growth introduced by the dipoles B_1 , B_2 and B_3 is acceptable for an effective β^* of 5 mm and for a beam energy of 60 GeV.

The second and third modules, used for the chromatic correction system, each have unity magnifications in the x and y transverse planes. These two modules each consist of a FODO array of four identical quadrupole singlets (with interspersed dipoles and sextupoles). These modules are placed either in mirror or sequential symmetry with respect

TABLE IIIa

Redbook FFS (room temp quads) component values at 50 GeV

P = 50 GeV/c		ELEMENT	LENGTH	POLE FIELD	APERTURE RADIUS
			meters	kGauss	mm
(COLLIDER ARC ENDS HERE)					
		DRIFT	-0.50000;		
20.0			180.00000;		
		BEND	"B1 "	1.00000	13.18819 (BEND LEFT 0.453 deg)
20.0			-180.00000;		
		DRIFT	0.50000;		
		QUAD	"Q1 "	1.00000	2.20953 10.00000;
		DRIFT	3.95809;		
		QUAD	"Q2 "	1.00000	-2.34909 10.00000;
		DRIFT	16.15611;		
		QUAD	"Q3 "	1.00000	6.26167 10.00000;
		DRIFT	1.00000;		
		QUAD	"Q4 "	2.00000	-5.44032 10.00000;
20.0			180.00000;		
		BEND	"B2 "	4.00000	12.75000 (BEND LEFT 1.752 deg)
20.0			-180.00000;		
		QUAD	"Q5 "	1.00000	-2.25699 10.00000;
		DRIFT	5.56604;		
		QUAD	"Q6 "	1.00000	2.51495 10.00000;
		DRIFT	11.67978;		
		QUAD	"Q7 "	1.00000	-7.11579 10.00000;
		DRIFT	1.00000;		
		QUAD	"Q8 "	2.00000	7.52838 10.00000;
		DRIFT	1.00000;		
		DRIFT	3.00000;		
		QUAD	"Q9 "	2.00000	8.56019 20.00000;
		SEXTUPOLE	"SX "	0.25000	7.29741 20.00000;
		DRIFT	0.75000;		
		QUAD	"Q10 "	1.50000	-7.42714 20.00000;
		SEXTUPOLE	"SY "	0.50000	-4.55515 20.00000;
		DRIFT	16.08057;		
		QUAD	"Q11 "	1.00000	6.97730 20.00000;
		DRIFT	1.37589;		
		QUAD	"Q12 "	1.00000	-7.27472 20.00000;
		DRIFT	1.00000;		
		BEND	"B3 "	2.00000	13.33333 (BEND RIGHT 0.916 deg)
		DRIFT	1.00000;		
		QUAD	"Q12 "	1.00000	-7.72472 20.00000;
		DRIFT	1.37589;		
		QUAD	"Q11 "	1.00000	6.97730 20.00000;
		DRIFT	16.08057;		
		SEXTUPOLE	"SY "	0.50000	-4.55515 20.00000;
		QUAD	"Q10 "	1.50000	-7.42714 20.00000;
		DRIFT	0.75000;		
		SEXTUPOLE	"SX "	0.25000	7.29741 20.00000;
		QUAD	"Q9 "	2.00000	8.56019 20.00000;
		DRIFT	3.00000;		
(THE INTERACTION POINT IS HERE. BETA STAR = 10 mm)					

TABLE IIIb

Redbook FFS (superconducting quads) component values at 50 GeV

ELEMENT		LENGTH	POLE FIELD	APERTURE RADIUS
P = 50 GeV/c		meters	kGauss	mm
(COLLIDER ARC ENDS HERE)				
DRIFT		-0.50000;		
20.0		180.00000;		
BEND		1.00000	15.66006 (BEND LEFT 0.538 deg)	
20.0		-180.00000;		
DRIFT		0.50000;		
QUAD	"Q1 "	0.20000	28.16000	20.00000;
DRIFT		2.17201;		
QUAD	"Q2 "	0.20000	-29.84869	20.00000;
DRIFT		17.64505;		
QUAD	"Q3 "	0.65000	33.98247	20.00000;
DRIFT		0.25000;		
QUAD	"Q4 "	0.80000	-34.84401	20.00000;
DRIFT		0.25000;		
20.0		180.00000;		
BEND		5.00000	15.55970 (BEND LEFT 2.673 deg)	
20.0		-180.00000;		
DRIFT		0.25000;		
QUAD	"Q5 "	0.20000	-23.91441	20.00000;
DRIFT		7.35839;		
QUAD	"Q6 "	0.20000	31.98665	20.00000;
DRIFT		7.27932;		
QUAD	"Q7 "	0.75000	-35.74924	20.00000;
DRIFT		0.25000;		
QUAD	"Q8 "	1.75000	36.33745	20.00000;
DRIFT		0.15000;		
DRIFT		4.50000;		
QUAD	"Q9 "	0.75000	37.48129	35.00000;
SEXTUPOLE	"SX "	0.75000	4.77022	35.00000;
DRIFT		0.25000;		
QUAD	"Q10 "	0.60000	-37.33879	35.00000;
SEXTUPOLE	"SY "	0.75000	-6.00123	35.00000;
DRIFT		18.52466;		
QUAD	"Q11 "	0.70000	36.93974	70.00000;
DRIFT		0.97768;		
QUAD	"Q12 "	0.70000	-36.74609	70.00000;
DRIFT		0.50000;		
BEND		5.00000	8.49325 (BEND RIGHT 1.459 deg)	
DRIFT		0.50000;		
QUAD	"Q12 "	0.70000	-36.74609	70.00000;
DRIFT		0.97768;		
QUAD	"Q11 "	0.70000	36.93974	70.00000;
DRIFT		18.52466;		
SEXTUPOLE	"SY "	0.75000	-6.00123	35.00000;
QUAD	"Q10 "	0.60000	-37.33879	35.00000;
DRIFT		0.25000;		
SEXTUPOLE	"SX "	0.75000	4.77022	35.00000;
QUAD	"Q9 "	0.75000	37.48129	35.00000;
DRIFT		4.50000;		
(THE INTERACTION POINT IS HERE. BETA STAR = 5 mm)				

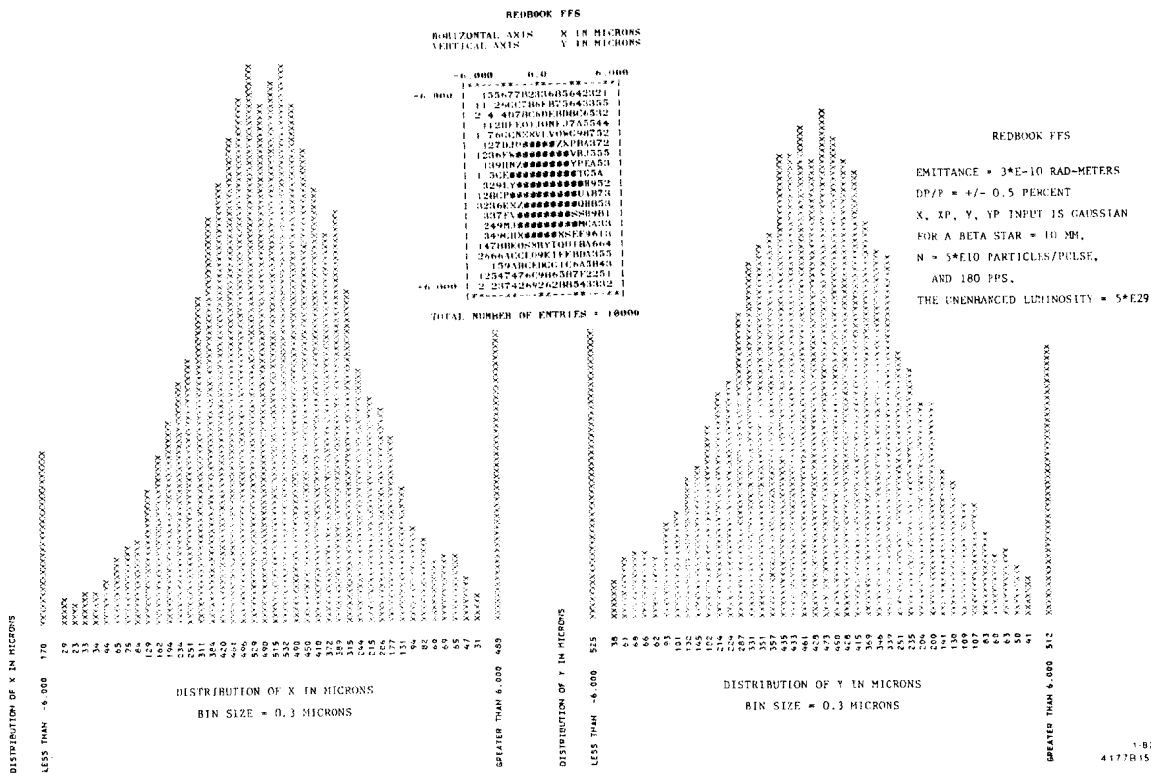


Fig. 5(a). "Redbook" type FFS beam distribution at the IP for conventional quadrupole optics.

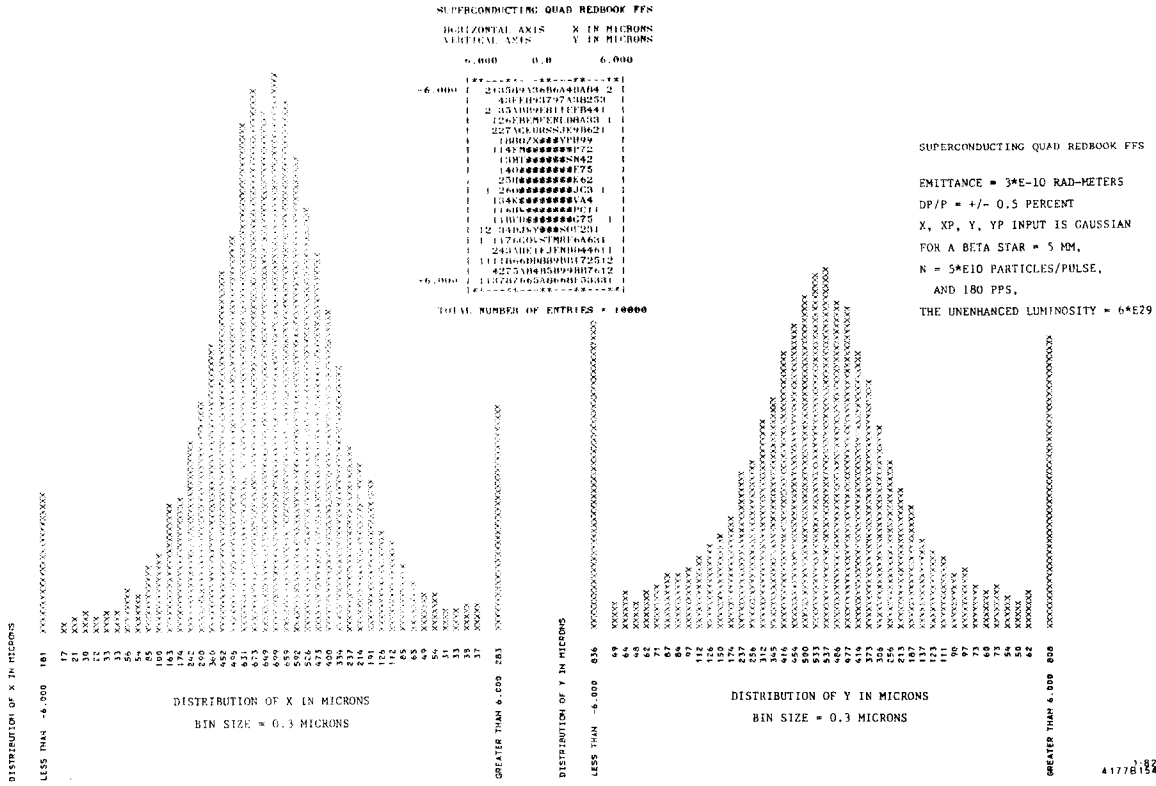


Fig. 5(b). "Redbook" type FFS beam distribution at the IP for superconducting quadrupole optics.

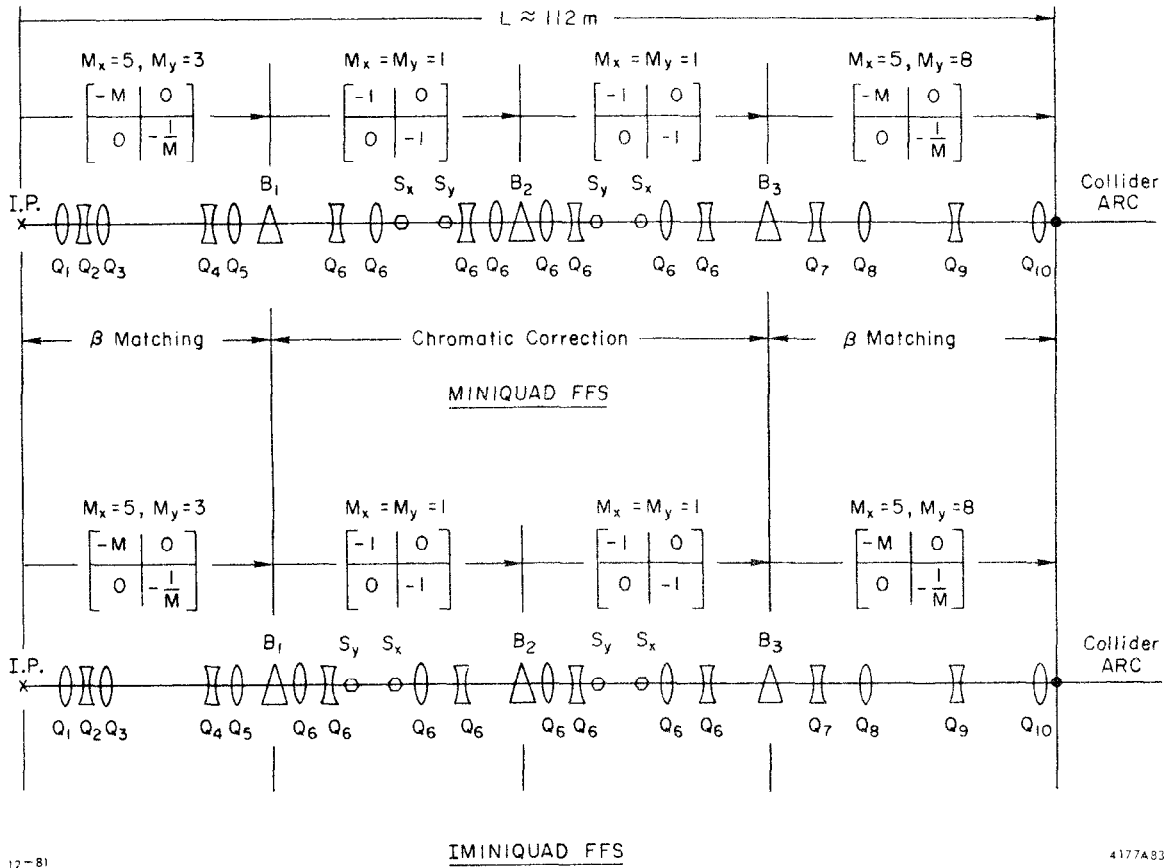


Fig. 6. Miniquad and Iminiquad final focus systems.

to each other, depending upon the optical properties desired. In the "miniquad" system mirror symmetry is used in which case the dominant optical distortions will tend to be third order geometric aberrations. In the "Iminiquad" system sequential symmetry is used and the dominant optical distortions will tend to be third order chromatic aberrations. Dipoles are introduced at the junction of modules 1 and 2, 2 and 3, and 3 and 4. The first and third dipoles are of the same strength and the second dipole, located between modules 2 and 3 has twice the strength of the others. This arrangement produces a symmetric momentum dispersion about the junction 23. Sextupoles pairs are introduced, in each transverse plane, at the locations shown. Each sextupole from a given pair is positioned so that the momentum dispersion is the same at each member of the pair. The R_{12} and the R_{34} matrix elements, the sine-like functions, have the same magnitude but opposite sign at each of the conjugate elements of a given sextupole pair. This arrangement of the sextupole pairs results in a natural cancellation of the second-order geometric aberrations which would otherwise be troublesome. The strengths of the sextupole pairs are then adjusted to eliminate the second-order chromatic aberrations, $T(1\ 26)$ and $T(3\ 46)$, which are the main source of the optical distortions.

The function of the fourth module is to complete the beam envelope matching to the collider arc. This module is shown in Fig. 6 as a telescopic system, similar to module 1, however considerable flexibility exists in the design of this module because the chromatic corrections have already been achieved in modules 2 and 3.

The overall length required to match from a β^* of 5 mm at the IP to a β_L of 4 meters at the collider arc is approximately 115 meters.

TRANSPORT listings of the miniquad and Iminiquad components are given in Tables IVa and IVb respectively.

4. Discussion of the Miniquad Systems

The miniquad FFS has been so named because the first three quadrupoles, located close to the interaction point, have small apertures of (± 10 mm). The input face of the first quadrupole is 25 cm from the IP. The subsequent two quadrupoles are closely spaced to each other. The

TABLE IVa
Miniquad FFS component values at 50 GeV

ELEMENT		LENGTH	POLE FIELD	APERTURE RADIUS
P = 50 GeV/c		meters	kGauss	mm
(THE INTERACTION POINT IS HERE. BETA STAR = 5 mm)				
DRIFT		0.25000;		
QUAD	"Q1 "	1.67000	8.00000	10.00000;
DRIFT		0.25000;		
QUAD	"Q2 "	1.65000	-8.15489	10.00000;
DRIFT		0.50000;		
QUAD	"Q3 "	1.80000	8.15371	20.00000;
DRIFT		11.60082;		
QUAD	"Q4 "	1.50000	-9.76219	50.00000;
DRIFT		2.77432;		
QUAD	"Q5 "	1.50000	7.38666	60.00000;
BEND	"B1 "	5.00000	4.71782 (BEND 0.810 deg)	
DRIFT		5.50000;		
QUAD	"Q6 "	0.75000	-11.74542	20.00000;
DRIFT		2.00000;		
QUAD	"Q6 "	0.75000	11.74542	20.00000;
SEXTUPOLE	"SX "	0.50000	1.99776	20.00000;
DRIFT		10.00000;		
SEXTUPOLE	"SY "	0.50000	-4.54254	12.00000;
QUAD	"Q6 "	0.75000	-11.74542	20.00000;
DRIFT		2.00000;		
QUAD	"Q6 "	0.75000	11.74542	20.00000;
BEND	"B2 "	6.00000	7.86303 (BEND 1.620 deg)	
QUAD	"Q6 "	0.75000	11.74542	20.00000;
DRIFT		2.00000;		
QUAD	"Q6 "	0.75000	-11.74542	20.00000;
SEXTUPOLE	"SY "	0.50000	-4.54254	12.00000;
DRIFT		10.00000;		
SEXTUPOLE	"SX "	0.50000	1.99776	20.00000;
QUAD	"Q6 "	0.75000	11.74542	20.00000;
DRIFT		2.00000;		
QUAD	"Q6 "	0.75000	-11.74542	20.00000;
DRIFT		7.00000;		
BEND	"B3 "	2.00000	11.79454 (BEND 0.810 deg)	
QUAD	"Q7 "	1.50000	-11.32348	10.00000;
DRIFT		0.75000;		
QUAD	"Q8 "	1.00000	8.38917	10.00000;
DRIFT		12.08835;		
QUAD	"Q9 "	0.50000	-8.01564	20.00000;
DRIFT		10.06006;		
QUAD	"Q10 "	0.50000	5.49547	20.00000;
DRIFT		1.00000;		
(THE COLLIDER ARC BEGINS HERE)				

TABLE IVb

Iminiquad FFS component values at 50 GeV

ELEMENT		LENGTH	POLE FIELD	APERTURE RADIUS
P = 50 GeV/c		meters	kGauss	mm
(THE INTERACTION POINT IS HERE. BETA STAR = 5 mm)				
DRIFT		0.25000;		
QUAD	"Q1 "	1.67000	8.00000	10.00000;
DRIFT		0.25000;		
QUAD	"Q2 "	1.65000	-8.15489	10.00000;
DRIFT		0.50000;		
QUAD	"Q3 "	1.80000	8.15371	20.00000;
DRIFT		11.60082;		
QUAD	"Q4 "	1.50000	-9.76219	50.00000;
DRIFT		2.77432;		
QUAD	"Q5 "	1.50000	7.38666	60.00000;
BEND	"B1 "	5.00000	4.71782	(BEND 0.810 deg)
DRIFT		0.50000;		
QUAD	"Q6 "	0.75000	11.74542	20.00000;
DRIFT		2.00000;		
QUAD	"Q6 "	0.75000	-11.74542	20.00000;
SEXTUPOLE	"SY "	0.50000	-4.54254	12.00000;
DRIFT		10.00000;		
SEXTUPOLE	"SX "	0.50000	1.99776	20.00000;
QUAD	"Q6 "	0.75000	11.74542	20.00000;
DRIFT		2.00000;		
QUAD	"Q6 "	0.75000	-11.74542	20.00000;
DRIFT		5.00000;		
BEND	"B2 "	6.00000	7.86303	(BEND 1.620 deg)
QUAD	"Q6 "	0.75000	11.74542	20.00000;
DRIFT		2.00000;		
QUAD	"Q6 "	0.75000	-11.74542	20.00000;
SEXTUPOLE	"SY "	0.50000	-4.54254	12.00000;
DRIFT		10.00000;		
SEXTUPOLE	"SX "	0.50000	1.99776	20.00000;
QUAD	"Q6 "	0.75000	11.74542	20.00000;
DRIFT		2.00000;		
QUAD	"Q6 "	0.75000	-11.74542	20.00000;
DRIFT		7.00000;		
BEND	"B3 "	2.00000	11.79454	(BEND 0.810 deg)
QUAD	"Q7 "	1.50000	-11.32348	10.00000;
DRIFT		0.75000;		
QUAD	"Q8 "	1.00000	8.38917	10.00000;
DRIFT		12.08835;		
QUAD	"Q9 "	0.50000	-8.01564	20.00000;
DRIFT		10.06006;		
QUAD	"Q10 "	0.50000	5.49547	20.00000;
DRIFT		1.00000;		
(THE COLLIDER ARC BEGINS HERE)				

purpose of this is to minimize the second-order path length differences $T(5\ 22)$ and $T(5\ 44)$ and hence the second-order chromatic distortions of the system. This in turn minimizes the strength of sextupoles needed for the chromatic correction. And as a consequence, the residual third-order aberrations introduced by the sextupoles are kept small. All of this leads to achieving a small beam spot size at the interaction point. The disadvantage of this design is that the first two or three quadrupoles must be located inside the detector system. This implies that materials having a magnetic permeability other than unity are undesirable. As a consequence these quadrupoles must be permanent magnets made from SmCo_5 , or iron free superconducting magnets, or iron free pulsed magnets.

For the miniquad systems the values of the second-order path length matrix elements, with the sextupoles turned off, have been determined using TRANSPORT. For beta matching only, $T(5\ 22) = T(5\ 44) = 4.6$ meters and when the chromatic correction section is added to this, the result is $T(5\ 22) = T(5\ 44) = 7$ meters. This is a substantial improvement over the Redbook type solutions which have a drift distance of 3 to 4 meters from the IP to the face of the first quadrupole, see Table I. The net result is that the miniquad system is capable of achieving a significantly better luminosity at the IP.

The quality of the beam spot at the interaction point is shown in Fig. 7(a) for the miniquad system and in Fig. 7(b) for the Iminiquad FFS. As can be seen from these histograms, the Iminiquad result is definitely superior to the microquad, redbook, and miniquad final focus solutions.

D. Conclusions and Summary

The Iminiquad final focus system has been selected as the preferred solution for the following reasons:

- (a) It provides the best luminosity at the interaction point among all of the systems studied to date, see the comparisons in Table V.
- (b) The chromatic correction system used in the miniquad solutions is the easiest to adjust because all of the quadrupoles in this region are identical.

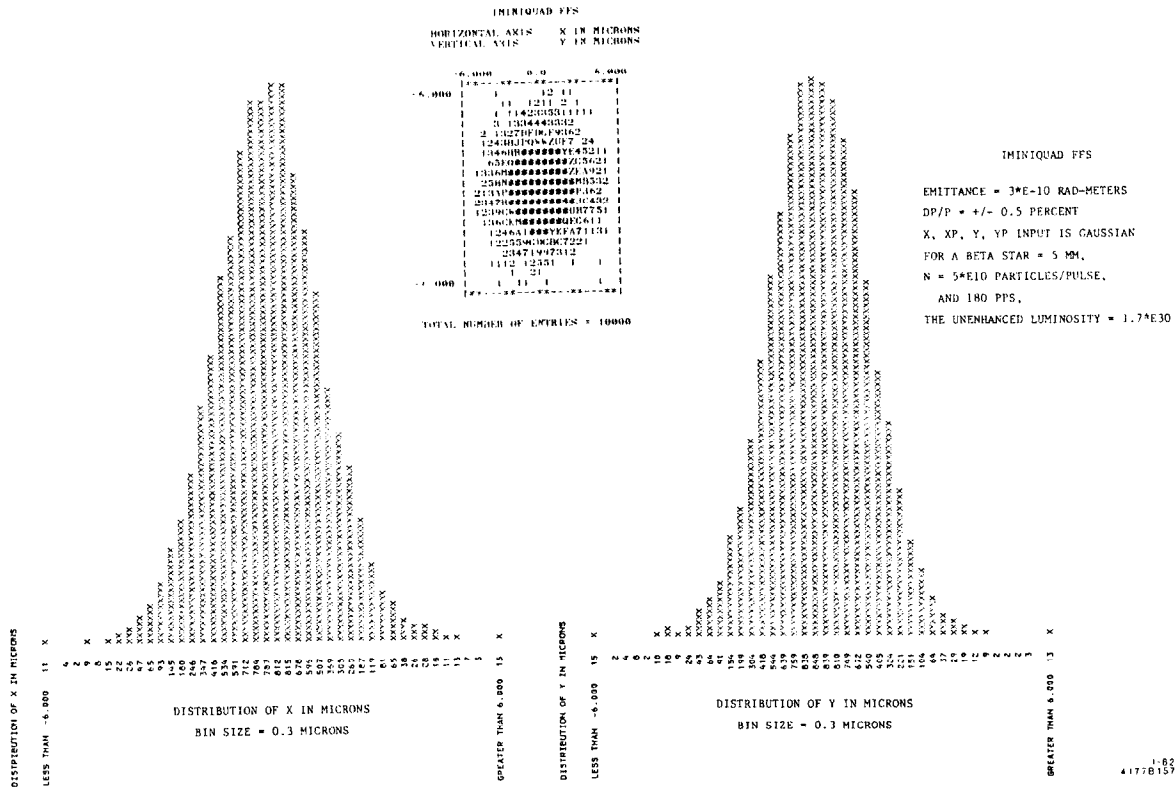


Fig. 7(b). Iminiquad FFS beam distribution at the IP.

TABLE V

Unenhanced luminosity comparisons at 50 GeV for the three different final focus systems assuming 5×10^{10} particles/bunch and 180 collisions/sec.

System	\mathcal{L}_0 (unenhanced Luminosity) $\text{cm}^{-2}\text{sec}^{-1}$
Microquad	9.6×10^{29}
Red Book	5.0×10^{29}
S. C. Redbook	6.0×10^{29}
Miniquad	1.2×10^{30}
Iminiquad	1.7×10^{30}

- (c) The symmetry employed in the chromatic correction region provides a natural cancellation for the $(x, \delta\delta)$ chromatic aberration. Thus all of the second-order chromatic corrections are completed at the end of this section.
- (d) The alignment tolerances are less severe than for the redbook type solutions. This is because the asymmetries in the x and y beam envelopes in the miniquad solutions are smaller. The rotational alignment tolerances for the miniquad FFS are discussed in Appendix A.

Disadvantages of the miniquad solutions include the following:

- (a) The first two or three quadrupoles are inside the detector. This complicates the tuning procedure if permanent magnet quadrupoles are used. This is discussed briefly in Appendix B.
- (b) To shield the interaction region from the synchrotron radiation from the last hard bend,¹⁰ a larger field strength "soft bend" must be used in the miniquad FFS than in the redbook type FFS.

References

1. K. L. Brown, F. Bulos and J. A. J. Matthews, SLC Workshop Note 65.
2. K. L. Brown, D. C. Carey, Ch. Iselin and F. Rothacker, TRANSPORT a computer program for designing charged particle beam transport systems, SLAC-91 (1973 rev.), NAL-91, and CERN 80-04.
3. K. L. Brown, Beam Envelope Matching for Beam Guidance Systems, SLAC-PUB-2370 (August 1980), and Nucl. Instrum. Methods 187, 51-65 (1981); presented at the Conference on Charged Particle Optics, Giessen, West Germany, September 8-12, 1980.
4. D. C. Carey, K. L. Brown and Ch. Iselin, TURTLE a computer program for simulating charged particle beam transport systems, including decay calculations, FERMILAB Report NAL-64 (December 1971), and CERN 74-2 (February 1974).
5. GIOS is a computer program developed by Wollnik and Matsuda in Giessen, West Germany and in Japan, it is not in published form as yet.
6. The differential ray tracing program referred to in this report has been developed by Jim Spencer at SLAC. No formal report on this program has been published.
7. K. L. Brown, A First- and Second-Order Matrix Theory for the Design of Beam Transport Systems and Charged Particle Spectrometers, SLAC Report No. 75, or Adv. Part. Phys. 1, 71-134 (1967).
8. K. G. Steffen, High-Energy Beam Optics, Interscience Monographs and Texts in Physics and Astronomy, Vol. 17, John Wiley and Sons, New York (1965).
9. SLC Conceptual Design Report, SLAC Report 229 (1980).
10. E. S. Miller and J. C. Sens, SLC Workshop Note 53.
11. R. Gluckstern and R. Holsinger, NIM (1981).
12. J. Matthews, SLC "IR Group" Minutes, June 25, 1981.

APPENDIX A
ROTATION TOLERANCES

Initial studies have shown that rotational tolerances for some of the quads in the MINI and RB type FFS solutions may be uncomfortably stringent. It was decided to use TURTLE to investigate the effect of tolerances on the expected luminosity.

Using the proper beam parameters from the lattice, the number of particles passing through angular rings at the IR were determined from TURTLE. The first ring was a circle of radius = 0.5 μ , and the width of the successive rings was kept constant also at 0.5 μ .

With a round spot at the IR the densities going around a ring remain constant. Hence the fractional density, $d_f(k)$, in ring k is:

$$d_f(k) = n_k / N_0 A_k$$

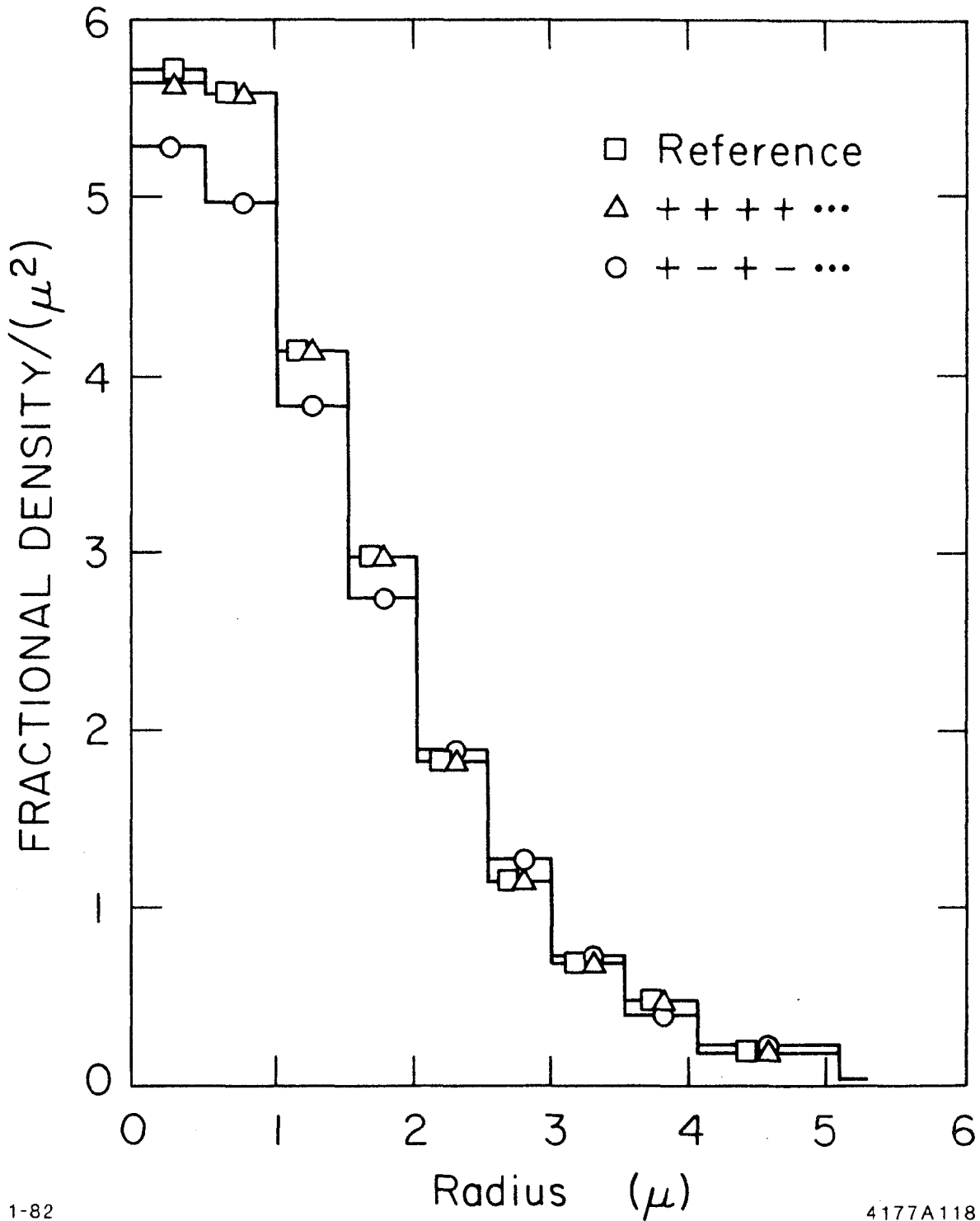
where n_k is the number of particles in ring k, N_0 is the total number of particles at the input of FFS, and A_k is the area of ring k. Hence

$$d_f^2(k) \times A_k \propto \mathcal{L}(k)$$
$$\sum_k d_f^2(k) A_k \propto \sum_k \mathcal{L}(k)$$

where $\mathcal{L}(k)$ is the contribution of (unenhanced) luminosity from ring k. The $\sum_k \mathcal{L}(k)$ can easily be obtained for the rings inside any radius r.

To investigate rotational tolerances, one can rotate any number of magnets and use this method to find the effect on (unenhanced) luminosity. The miniquad FFS was selected for this study. Azimuthal alignment tolerances (about the beam axis, z, direction) of 0.1 mrad were assumed. All the sensitive quadrupoles in the miniquad optics (10 elements) were rotated by 0.1 mrad: first all in the same direction, and secondly alternately at +0.1 mrad, -0.1 mrad, etc.

Figure A-1 and Table A-I show the results. It is clear that same sign rotations have no effects, and that alternate rotations reduce the unenhanced luminosity 10-20% depending on the radius r inside which $\sum \mathcal{L}$ was performed.



1-82

4177A118

Fig. A-1. Beam fractional e^+ densities per square micron at the IP for the miniquad FFS, and for the miniquad FFS with quadrupole azimuthal alignment errors of ± 0.1 mrad.

TABLE A-I

" $\sum_k \mathcal{L}(k)$ " as a function of radius for no misalignment, +++... misalignment, and +-+... misalignment of ten quadrupoles in the miniquad FFS.

Radius (microns)	" $\sum_k \mathcal{L}(k)$ "		
	no misalignment (10^{-4})	+++... (10^{-4})	+-+... (10^{-4})
1.5	168.1	166.8	137.7
3.0	250.8	251.2	218.1
5.0	258.3	258.8	226.4
10.0	258.5	259.0	226.8

Note: To convert to the unenhanced luminosity, \mathcal{L}_0 , for the SLC:

$$\mathcal{L}_0 = \frac{N^2 \times \sum_k \mathcal{L}(k) \times 180 \text{ (pulses/sec)}}{10^{-8} (\mu^2 \rightarrow \text{cm}^2)} \text{ cm}^{-2} \text{ sec}^{-1}$$

where N is the number of e^\pm /bunch.

APPENDIX B
TUNABILITY OF PERMANENT MAGNET QUADRUPOLES

Unlike electromagnetic quads, permanent quads present some difficulties when one wishes to tune them for various beam momenta. As shown in Ref. 11, by dividing the quads into five sections, grouping the sections in mirror image pairs around the single central section then rotating the pairs and central section alternately in opposite directions, one can "tune" the quadrupoles as a function of momentum without introducing x-y coupling in the beam.

We have verified¹² this method using TRANSPORT and TURTLE. A suitable mechanism for making a precise rotation of the sections, and incorporating such a mechanism in the structure and support of the magnet is under investigation.

III. BEAM POSITION MONITORING

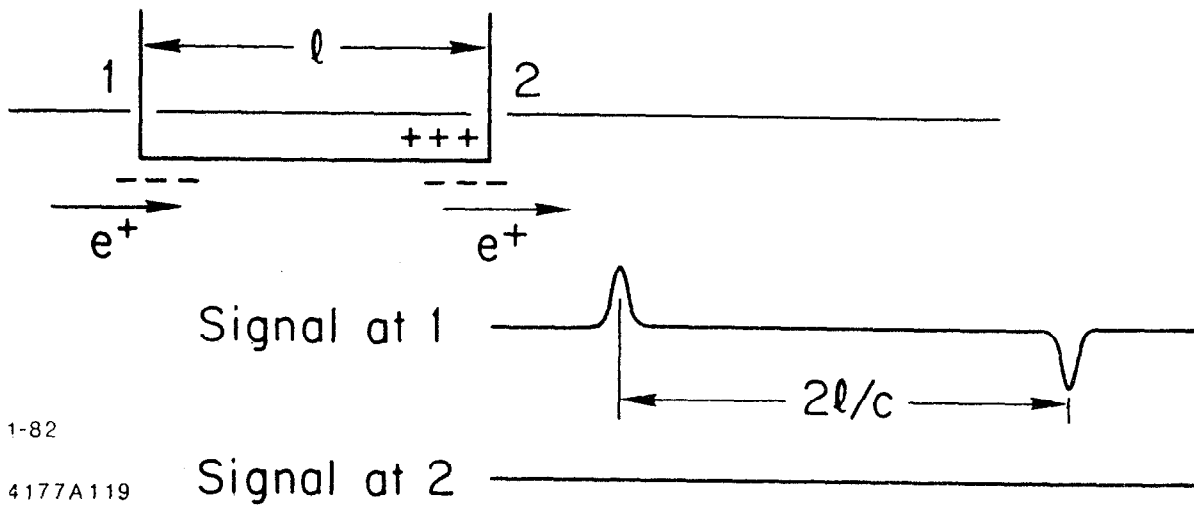
A. Introduction

The SLC beams will consist of pulses that are about $2\frac{1}{2}$ microns in diameter and 2000 microns in length; they are needles whose diameter is about that of the smallest human cells. If the beam is imagined to be magnified to the diameter of an ordinary sewing needle, the beam pipe is then magnified to the diameter of a haystack. Two approaches are proposed for finding the needles in the haystack. The first¹ proposes a strip line monitor to guide steering over the range of several millimeters beam separation down to five microns. The second² proposes to use synchrotron radiation from the beam-beam interaction to cover the range of 100 microns down to a fraction of a micron. As soon as reasonably intense beams can be focused into the interaction region, the two methods in combination should make it feasible to produce almost perfect head-on collisions without much further effort.

B. Strip Line SLC Beam Position Monitor Near the Interaction Point

The question addressed in this section is how well one can determine the positions of the e^+ and e^- beams by strip lines near the interaction point. We then propose¹ a system which should be useful for beam monitoring with emphasis on the relative position of the two beams as opposed to their absolute position. Five micron accuracy should be achievable so that the useful range overlaps that of a beamstrahlung monitor.

A brief description of strip-line operation is in order. Referring to Fig. 1 a beam of charged particles very short compared to the length of the strip line passes end 1 of the strip line and induces a charge. A pulse of opposite sign is transmitted down line 1 to the electronics. The induced charge travels down the strip line towards end 2 at the speed of the beam. As the beam passes end 2 we may think of a second charge being induced equal and opposite to the first. This sends a second pulse down line 1 equal and opposite to the first and delayed from it by $2 \ell/c$. There is no net charge on end 2 of the line once the beam has passed. Hence there is no signal on line 2 independent of the termination of the



1-82

4177A119

Fig. 1. Strip line position monitor pulse shapes for strip lines of length " l ".

strip line at that end. For a beam in the opposite direction line 2 sees a signal but not line 1. Strip lines are often terminated by shorting them to ground at the downstream end. However this is not necessary. In the proposed system the strip lines are matched to coax at both ends. The electronics at each end detects one of the beams but not the other.

A proposed strip-line system is illustrated in Fig. 2. The dimensions are meant to be indicative of an actual system but by no means a final design. The two sets of lines, one on each side of the interaction point, measure two x positions for the beam and by interpolation give the position at the interaction point. Lines 1, 3, 5 and 7 detect a beam traveling towards the right; 2, 4, 6 and 8 a beam traveling towards the left.

To calibrate the system a fine wire is strung down the axis. A pulse is applied to it and the pulse height ratios q_1/q_3 , q_2/q_4 , q_5/q_7 , and q_6/q_8 are measured. The wire must be straight to the desired accuracy. On the other hand while the wire should be placed as close to the axis as practicable the position need not be super-precise because we are interested primarily in the relative position of the beams. Put another way, the measured ratios above determine 4 points on a straight line. When we work with actual beams the 4 ratios measurements will tell us displacements of the beams from this straight line and thus their relative position.

The arguments above assume an idealized system. In a real system there are a number of differences. First no electronics is available which has a large enough band width to follow the induced pulse. In addition there is no way of generating a calibrating pulse narrow enough to simulate the induced pulse. Also the pulse width of the induced pulse will be broadened by the coax connecting the strip line to the electronics. The strip-line system even if made to high accuracy must be assumed to become misaligned by small amounts due to mechanical strains since the two sets of electrodes are connected only by the beam pipe which must be kept thin for optimal detector design.

In the idealized system one beam is measured at 1 and 5, the other at 2 and 6. The effect of mechanical misalignments could be eliminated

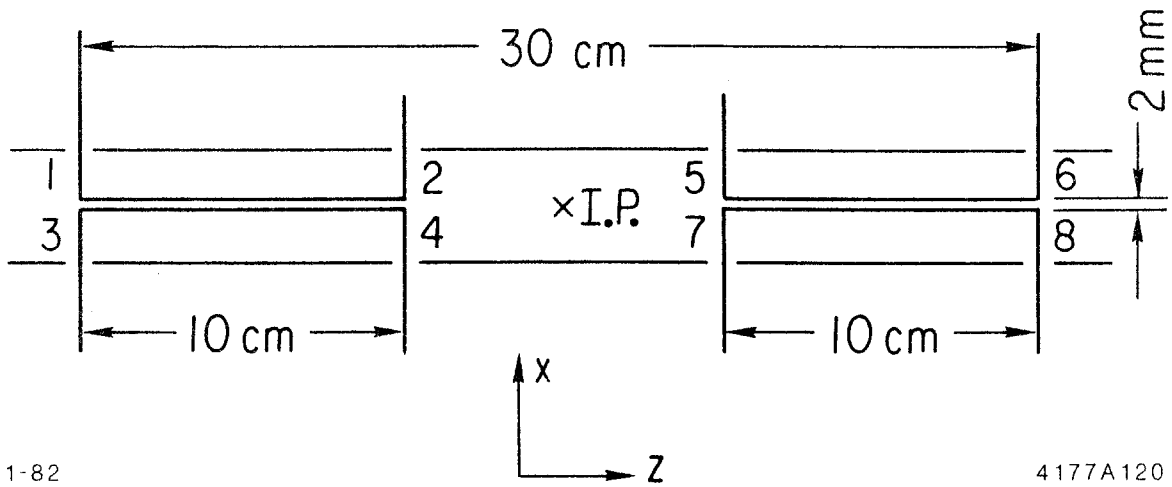


Fig. 2. Strip line position monitors at the SLC interaction point.

if measurements on both beams were made at the same place on the strip lines -- for example, halfway between 1 and 2, and 5 and 6.

In a real system we are not measuring at points 1 and 5 or 2 and 6 because of limited frequency response. If the beam does not move parallel to the strip line there will be changes in the induced charge as the beam changes its x position relative to the strip line. Thus we can take advantage of the limited frequency response of the system by adjusting the strip-line length and the electronic response time so that we are sampling the integrated induced charge halfway down the strip lines (at $t = \ell/c$ after the beginning of the pulse). Then the x positions of the two beams are being measured at the same z and alignment errors are eliminated.

The ultimate accuracy of the system will depend on four factors:

(1) Stability and Noise Level of Electronics

A reasonable guess is that this can be done to ~ 1 part in 10^{-3} so that if the strip-line separation is 2 mm it will contribute 2 micron position uncertainty. The accuracy quoted is based on sector 1 experience as to pulse-to-pulse repeatability. Other factors will contribute larger errors than this so an increase in strip-line separation can be tolerated without noticeably affecting overall accuracy.

(2) Strip Line Alignment

While standard optical techniques would allow this to be done 1 micron lack of mechanical rigidity will limit the attainable accuracy to 10 or 20 times that.

(3) Pulse Sampling Position

Item 2 is not a limitation provided we sample the induced charge at the center of the strip lines. How closely this can be done must be determined experimentally.

(4) Strip Line Matching

A good match between strip line and coax is essential since the line is short and reflections could effect measured pulse heights.

C. Monitoring the Separation Between Beams with Synchrotron Radiation

In order to correct for errors in beam positioning, those errors must first be detected. A method is needed that is sensitive to very tiny beam offsets. In order to crudely estimate what happens when the collision deviates slightly from perfect overlap, let us temporarily approximate the Gaussian transverse distribution of the beams with a uniform cylindrical distribution of transverse radius $R = 2\sigma$. L , the luminosity, is the same as for a Gaussian distribution. Suppose one cylinder is shifted by $D \ll R$ relative to the other, see Fig. 3.

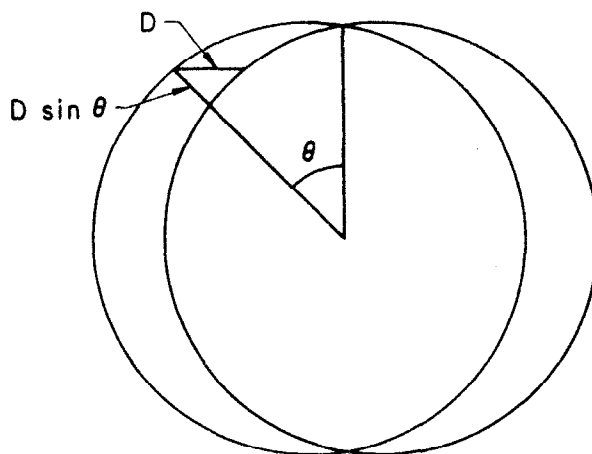


Fig. 3. Geometry for the "uniform cylindrical distribution" model for SLC beams' particle distribution.

Then the area that is removed from the overlap is:

$$\Delta \text{Area} \approx \int_0^{\pi} (D \sin \theta) R d\theta = 2RD \quad ,$$

and the luminosity is decreased by:

$$\frac{\Delta L}{L} = \frac{2RD}{\pi R^2} = \frac{2D}{\pi R} = \frac{D}{\pi \sigma} \quad .$$

With "standard" beam parameters:

$$N_+ = N_- = 5 \times 10^{10} \quad (e^\pm/\text{bunch})$$

$$E = 50 \text{ GeV} \quad (e^\pm \text{ beam energies})$$

$$\sigma_x = \sigma_y = \sigma = 1.3\mu \quad (\text{transverse beam standard deviation})$$

$$\sigma_z = 1 \text{ mm} \quad (\text{longitudinal beam standard deviation})$$

the luminosity will be decreased by about 25% when the SLC beams miss one another by one micron. Conventional strip or microwave monitors should permit steering the two beams to within about 50 microns.³ Although improvements in such monitoring will surely be made,^{1,4} it is unlikely that accuracy to the one micron level will be achieved by the time the SLC is built.

The demagnification of the focusing system implies that if the position of the beam changes at the beginning of the focusing system, that change will be decreased by a factor of 30 at the interaction point. It might be thought that this demagnification means that we need only monitor the beam position to 30 microns at the beginning of the focusing system in order to get 1 micron accuracy at the end. But this demagnification does nothing to bring the two small beam spots together. The location of each beam at the interaction point can be moved around independently by small motions of the final focus magnets.

One micron accuracy is even difficult to obtain destructively by temporarily putting a wire in the beam. A single beam pulse would blast a hole through the wire that is many times the beam diameter.

Bhabhas into the detector can be used to monitor luminosity, but they will come in too slowly to be used to conveniently steer the beams into collision.⁵

This section is devoted to discussing the monitoring of relative beam positions at the interaction point by means of synchrotron radiation emitted by the beams as they pass one another; for more details see Ref. 2. The magnetic fields around the SLC beam can get into the hundreds of kG range. This field from, say, the positron beam will bend the electrons' path. Since the electric forces contribute the same as the

magnetic, the force on the electrons is twice that from the magnetic field alone. When the beams collide head on, the resulting acceleration of the electrons causes them to radiate on the average roughly 35 MeV each (assuming no beam pinch). The synchrotron photons have energies of the order of 100 MeV, again ignoring beam pinch. With of the order of 5×10^{10} electrons per bunch, there should be no problem detecting the collision of the two beams. As C. Prescott has pointed out, one way of steering the beams into collision is to move them relative to one another in a raster pattern to find where the radiation is maximized. But for ease in steering, we are also interested in measuring the separation between the beams when they completely miss. Furthermore, when the beams are colliding, it would be helpful to know how far off they are from perfect overlap and what direction they need to be moved. These measurements must be made in the face of the synchrotron radiation caused by the magnetic fields of the final focus.

If the two beams miss completely with a separation r microns, $r \gg$ beam diameter, the average radiated energy per electron is:

$$\text{Energy/electron} = 6.58805 \times 10^{-23} \frac{N_+^2 E^2 \left[1 - e^{-r^2/2\sigma^2}\right]^2}{\sigma_z r^2} \quad (1)$$

with output energy/electron in MeV, E in GeV, σ_z in mm, and r in microns. With the "standard" beam parameters this results in roughly $400/r^2$ MeV/electron. With 5×10^{10} electrons, even at 100 micron separation, there will be 2×10^9 MeV radiated. For $r \gg$ beam diameter, the critical energy of this synchrotron radiation is:

$$\langle \epsilon_c \rangle = 4.1618 \times 10^{-12} \frac{N_+ \left[1 - e^{-r^2/2\sigma^2}\right] E^2}{\sigma_z r} \text{ MeV} \quad (2)$$

and with the "standard" beam parameters $\epsilon_c = 520/r$ MeV; again, E is in GeV, σ_z in mm, and r in microns. 9% of the photons have energy $> \epsilon_c = 5.2$ MeV at $r = 100$ microns, and some photons have considerably more energy. Roughly

$$.8 \sqrt{\epsilon/\epsilon_c} e^{-\epsilon/\epsilon_c}$$

of the radiated energy is in the form of photons with energy $\epsilon \gg \epsilon_c$. If it weren't for the backgrounds, it would be easy to use this radiated energy as a means of estimating r . In order to estimate the backgrounds, we must have some idea of where the monitor would be. Figure 4 shows the beam and its radiation near the interaction point. The final focus solution chosen is one close to the main candidate ("Mini") as of this writing. In this solution, and most of the others considered, the synchrotron radiation from the beam-beam interaction leaves the beam pipe around 30 meters from the interaction point. Unless something special is done, this radiation will hit a quadrupole shortly after it leaves the pipe. Thus at least part of the monitor must be after the first bend, roughly 30 meters from the interaction point. If the whole monitor is at 30 meters, it must be 7.5 cm in radius in order to contain the synchrotron radiation from the entire 2.5 mrad of the disrupted beam. This detector must somehow avoid being sensitive to background synchrotron radiation from the magnets within 30 meters of the interaction point. These magnets cause about $0.053B\Delta\theta$ MeV per electron to be radiated (B in kG, $\Delta\theta$ = number of mrad by which the beam is bent). For example, the bending magnet shown in Fig. 4 has about 4.7 kG field and causes about 14 mrad bend. It will produce about 3.5 MeV/electron, far more than the 0.04 MeV/electron signal from a 100 micron miss. Here are some suggestions for dealing with this background:

(1) Give up the idea of detecting radiation from distant misses, and use the monitor only for finding head-on collisions, where the signal is about 35 MeV/electron.

(2) Have a soft bend that is strong enough to make the hard bend radiation miss the monitor. The final focus solution of Fig. 4 has such a strong soft bend along with an S-bend in order to minimize background into the experiment. Of course, this method doesn't completely eliminate the problem, for now we have background in the monitor from the soft bend.

(3) Measure the background when the beams are steered \gg 100 microns apart, and subtract it. For the monitor to work at 100 micron separation,

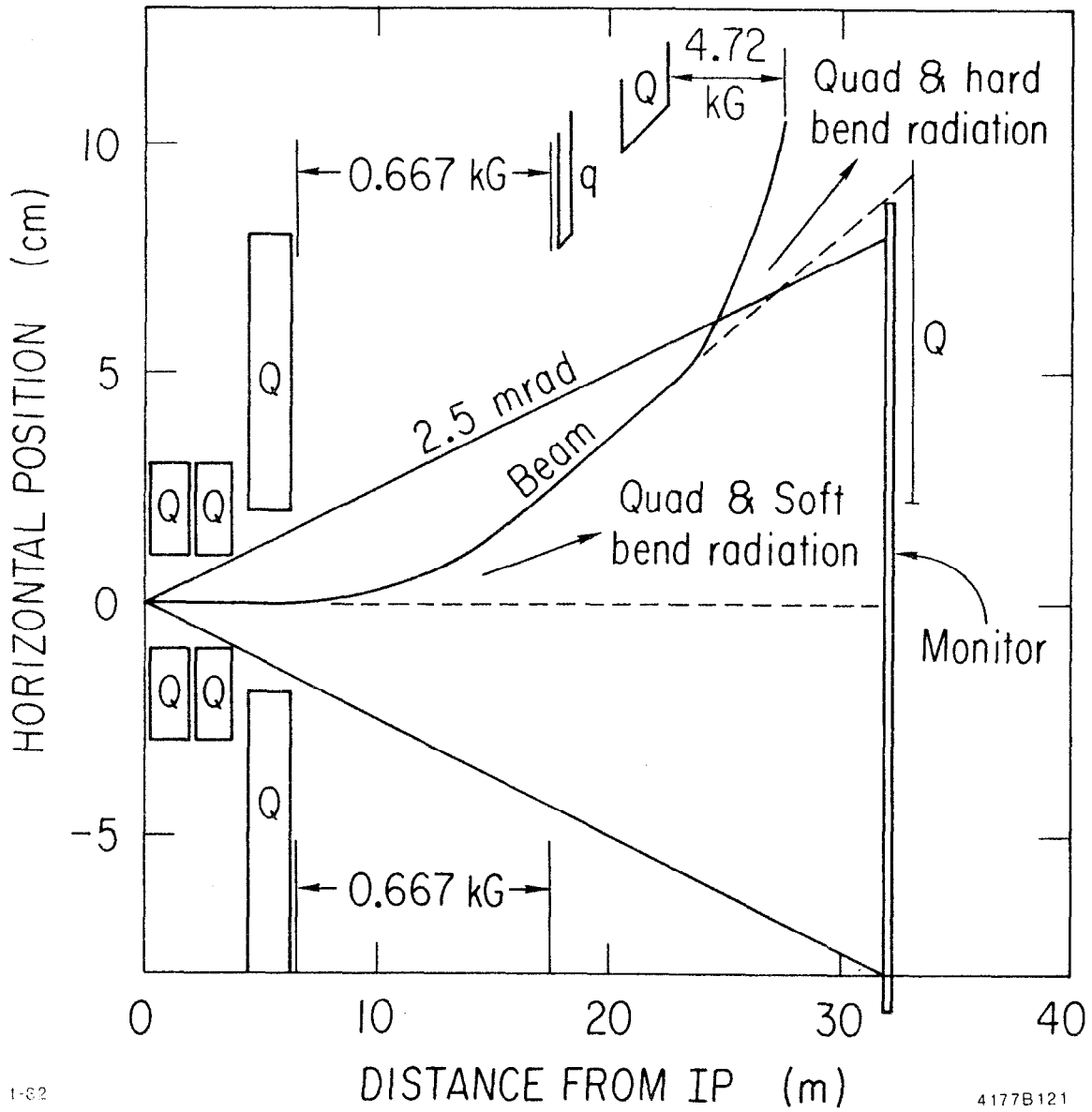


Fig. 4. Mini-quad optics near the interaction point showing the beamstrahlung monitor at 32 meters from the IP.

this subtraction would have to be done to about 1% accuracy, and would have to include the electron beam intensity as a proportionality constant. Even with poorer accuracy, this method would still work with small enough separations because the energy in the signal is proportional to $1/r^2$.

(4) Have the monitor consist of more than one piece. Part of the monitor can be placed before the bending magnet.

(5) Make the detector insensitive in the plane of the bending magnet's synchrotron radiation.

(6) Design the monitor so that it is much more sensitive to the photons from beam-beam interactions than to those from the magnets. In this section we will concentrate on this last method, which could be used in conjunction with other methods.

The critical energy for a 50 GeV electron beam radiating in a magnetic field of B kG is about $0.17B$ MeV. This amounts to about 0.8 MeV in the last bend of the proposed final focus, as compared to 5.2 MeV for the beam-beam interaction at 100 micron separation. A detector based on scintillator would be sensitive to 0.8 MeV photons, and such photons cannot be blocked out without also blocking 5.2 MeV photons. We propose using a detector based on Cherenkov radiation. By choosing the material, the energy to which the detector is sensitive can be tuned; see, for example, Table I. With lead before a Freon 12 gas Cherenkov counter, some of the photons in an $\epsilon_c = 5.2$ MeV synchrotron beam would have high enough energy to convert into an e^+e^- pair, one of which has more than the 10.5 MeV needed to radiate. But a negligible fraction of an $\epsilon_c = 0.8$ MeV spectrum could radiate in this manner.

To show that the Cherenkov radiation can be easily detected, here's an order of magnitude estimate of its amount for 100 micron beam separation:

Suppose 1% of the photons of energy $\epsilon > 4\epsilon_c = 20.8$ MeV can result in an electron or positron with over 10.5 MeV moving through the Freon. About 3% of the synchrotron energy will have $\epsilon/\epsilon_c = y > 4.2$. These photons will typically have energy near $4\epsilon_c$; so they will number about $0.03 \times (2 \times 10^9 \text{ MeV}) / (20.8 \text{ MeV}) \approx 3 \times 10^6$. Phototubes are sensitive over roughly a 1 eV photon energy range; so Table I implies roughly 1/2 photon

TABLE I

Electron Cherenkov thresholds (T_{\min}) and rates of Cherenkov radiation ($dN/dxd\epsilon$) for $\beta = 1$ and various materials.²

Material	$(n-1 = \delta) \times 10^3$	T_{\min} (MeV)	$\left. \frac{dN}{dxd\epsilon} \right _{\beta=1}^{CV}$ photons/cm-eV
He (STP)	0.035	60.6	0.026
Air (STP)	0.293	20.6	0.22
Freon 12 (26°C, 1 Atmosphere)	1.80	10.5	0.80
Silica Aerogel	25-75	0.9-1.8	18-50
Lucite	490	0.178	203

per cm emitted by electrons of energy greater than threshold. With 10% photocathode efficiency, 5% photon collection efficiency, and 3 cm of radiation path, a phototube would have about 250 photoelectrons leaving the cathode. The above estimate can be in error by two orders of magnitude and the monitor will still work. On the other hand, a background with $\epsilon_c = 0.8$ MeV has fraction roughly 6×10^{-6} above 10.5 MeV, so is effectively eliminated. Similar considerations lead us to conclude that synchrotron background from quadrupoles will also be eliminated.

If the electron beam passes slightly to the right of the positron beam during the collision, it will be deflected to the left and there will be an excess of synchrotron radiation in the left half of the monitor. Now the excess number of electrons that pass to the right is given by, see Fig. 3:

$$\left(\frac{\Delta \text{Area}}{\text{Area}} \right) N_- = \left(\frac{D}{\pi \sigma} \right) N_- = \left(\frac{\Delta L}{L} \right) N_-$$

and the number that pass on the left is decreased by the same amount. This results in an asymmetry:

$$\text{Asymmetry} = \frac{N_{\text{right}} - N_{\text{left}}}{N_{\text{right}} + N_{\text{left}}} = \frac{2\Delta L}{L} .$$

Consequently, the left right asymmetry will be roughly twice the fractional decrease in luminosity caused by the incomplete overlap. For quantitative work, it would be best to determine empirically the function relating the left right asymmetry to the distance between the two beams. But it is clear that this asymmetry is a sensitive measure of the goodness of overlap. The Cherenkov gas volume should thus be segmented into, say, 4 pieces -- up down and right left. Each segment should have its own phototube. Because there will be so much Cherenkov radiation in this detector, no great effort need be made to get light into the phototubes. If the inside of the box is reasonably reflective, the phototube can simply look into the gas volume from the side. The glass faces of the tubes should be well protected from ionizing radiation, else they might give off Cherenkov radiation of their own, or even become opaque from the radiation damage.

When the SLC first turns on, the beam intensity may well be a factor of ten below the design intensity. This would lead to a factor of more than 100 loss in luminosity. Under such circumstances, how would the above described monitor behave?

Equations (1) and (2) show that the synchrotron radiation per electron will be unchanged if the beam separation is also decreased by a factor of ten. At ten microns beam separation with 1/10 design beam intensity, about 25 photoelectrons per collision will leave the photocathode of the above described monitor. A raster scan in ten micron steps can then search for beam at a rate that would cover one square millimeter per minute.

With a tenth of design beam intensity, could the asymmetry in the synchrotron radiation angular distribution be used for fine steering at the sub-micron level? Ten times lower intensity would result in electromagnetic fields that are ten times smaller at a given position. Angular deflections would therefore also be reduced by roughly a factor of ten (not exactly, because the beam shape during collision depends on intensity). If the disruption angle before reducing intensity a factor of ten is about 2 mrad, then it will be about 0.2 mrad afterwards. A 0.2 mrad disruption angle means that at most 0.2 mrad angular deflection is given to particles that cross the oncoming beam off-center. 0.2 mrad at 30

meters corresponds to 0.6 cm deflection. Multiple scattering of the Cherenkov radiating electrons will tend to obscure the asymmetries if the monitor is more than a centimeter thick. Furthermore, the beam divergence before disruption is 0.3 mrad. Thus, although the above described monitor should still give some help in fine steering, it will be marginal at 1/10 beam intensities.

What happens at 1/100 of design beam intensity? Even for head on collisions, the critical energy will be reduced to 1.6 MeV, well below the 10.5 MeV threshold of Freon-12. The monitor will not work. But in place of the Freon, silica aerogel can be used. Aerogel gives off an order of magnitude more light and is sensitive to an order of magnitude lower electron energy than Freon-12. It is therefore sensitive to almost an order of magnitude lower beam intensity. To be more precise, with similar assumptions on thickness and light collection efficiency, the photocathode of an aerogel monitor would produce about seven photoelectrons for a ten micron beam separation at 1% of design intensity ($< 10^{-4}$ design luminosity). While it is true that an aerogel monitor would glow in hard bend synchrotron radiation, it should be easy to avoid that background. Lower beam intensities lead to smaller beam disruption angles; so the monitor can be made smaller. Even with a much smaller soft bend than is assumed in Fig. 1, the monitor can be kept well away from the hard bend radiation. Still greater sensitivity can be attained with lucite in place of the Freon-12, but then even the soft bend will cause trouble unless that field is well below the 0.667 kG of Fig. 4.

Since glass is easily damaged by radiation, we can expect silica aerogel to eventually suffer a similar fate. While aerogel may be needed for initial beam studies, as soon as beam intensities approach design levels, it should be replaced with Freon.

References

1. D. I. Meyer, SLC Workshop Note No. 33, anticipates five micron accuracy with a stripline monitor.
2. S. Yellin, SLC Workshop Note No. 47.
3. SLAC Linear Collider Conceptual Design Report, page 64, SLAC-229 (1980).
4. SLAC has made a prototype microwave monitor which, with planned improvements, is expected to achieve about seven micron accuracy (Steve Shapiro, private communication). Steve Williams (private communication) says that with a physical separation of 2 cm, present strip line monitors could achieve 10 microns resolution if their resolution were limited only by the statistical electronic noise observed on the bench. A smaller separation could achieve a proportionately smaller resolution.
5. D. Koltick and J. Va'Vra, SLC Workshop Note No. 8.

IV. LUMINOSITY MONITORING

A. Introduction

At SLC energies the photon and weak neutral boson will interfere strongly. It is important, if we are to calibrate the effect of the Z^0 , to study reactions that are essentially free of Z^0 effects. To this end two "QED" processes, small angle Bhabha scattering and $e^+e^- \rightarrow \gamma\gamma$, have been considered as the basis for a luminosity monitor.

In the angular range of 10 to ~ 60 mrad, we find that the Z^0 contributes $< 0.5\%$ (even for polarized beams) to the purely QED Bhabha rate in a "traditional" luminosity monitor. The event rates in a small angle Bhabha monitor, ~ 1 Hz for $\mathcal{L} \sim 1 \times 10^{30} \text{ cm}^{-2} \text{ sec}^{-1}$, are adequate for luminosity monitoring but inadequate for beam steering.

On the other hand, the "observable" cross section for $e^+e^- \rightarrow \gamma\gamma$ corresponds to ~ 10 units in "R", and may be too low to serve as a luminosity monitor in the Z^0 region.

B. Effects of the Z^0 on Bhabha Scattering

The expected Bhabha rate as a function of angle from the beam (see Appendix) is given in Table I. As can be seen, the Bhabha rate drops rapidly with angle (as θ^{-4}). The effect of the Z^0 is less than 10% over the SLC energy range in the angular region below 200 milliradian. The maximum effect of the Z^0 on Bhabha scattering occurs just off the peak; these are the results given in Table I. The effect of the longitudinal e^- beam polarization is also shown. The change in cross section at these angles, due to the Z^0 and polarization, is small. From Table I we can see that designing a luminosity monitor that extends beyond 50 or 60 milliradians receives very little increased flux.

While the upper angular limit of a luminosity monitor is set by the decreasing rate, the lower limit is set by apertures due to quadrupoles in the final focus. The Redbook and micro-quadrupole solutions allow viewing of the interaction region to just below 15 milliradians. This then sets the angular region to be covered by a luminosity monitor; a lower limit of 15 milliradians and an upper limit of 50 milliradians.

TABLE I

The maximum effect of the Z^0 on the Bhabha scattering rate occurs just off the resonance's peak. The effect, in percent, of the Z^0 is given for $h_- = 0$, no beam polarization, and for $h_- = \pm 1$, full electron beam polarization.

milliradian		$\frac{\sigma(Z^0, \gamma) - \sigma(\gamma)}{\sigma(\gamma)} \%$			
θ_{\min}	θ_{\max}	Bhabha Rate	$h_- = 0$	$h_- = +1$	$h_- = -1$
10	20	9.44 Hz	0.03%	0.02%	0.03%
20	30	1.75	0.09	0.07	0.11
30	40	0.61	0.19	0.15	0.22
40	50	0.28	0.32	0.26	0.37
50	60	0.15	0.47	0.39	0.55
60	70	0.09	0.67	0.55	0.78
70	80	0.06	0.89	0.74	1.04
80	90	0.04	1.15	0.95	1.34
90	100	0.03	1.43	1.19	1.68
100	110	0.02	1.76	1.45	2.06
110	120	0.02	2.11	1.75	2.48
120	130	0.01	2.50	2.07	2.93
130	140	0.01	2.92	2.42	3.43
140	150	0.008	3.38	2.79	3.98
150	160	0.007	3.90	3.20	4.56
160	170	0.006	4.41	3.63	5.19
170	180	0.005	4.97	4.09	5.86
180	190	0.004	5.58	4.59	6.58
190	200	0.003	6.23	5.11	7.35

$E_{\text{c.m.}} = 91.0 \text{ GeV} \quad ;$

$M_{Z^0} = 92.3 \text{ GeV}$

$\mathcal{L} = 10^{31} \text{ cm}^{-2} \text{ sec}^{-1} \quad ;$

$\Gamma_{Z^0} = 2.5 \text{ GeV}$

This is about the angular bite a 15 cm lead glass block would give if placed four meters from the interaction point (see Fig. 1).

The effect of the Z^0 on such a luminosity monitor is shown in Fig. 2. As shown, the Z^0 contributes less than 1/2% to the rate in such a counter. The event rates in the proposed luminosity monitor are compared to the Z^0 and $e^+e^- \rightarrow \mu^+\mu^-$ (total cross section) rates in Fig. 3.

C. e^+e^- Annihilation into Two Photons as a Luminosity Monitor

The reaction $e^+e^- \rightarrow \gamma\gamma$ is a candidate for a luminosity monitor since the Z^0 should have a small effect on this channel. This can be seen as follows.

Being neutral, the Z^0 has no direct coupling to photons. The coupling is due to higher order loop graphs like Fig. 4. Because the quantum numbers are incompatible, the Z^0 has no coupling, even through higher order, to two photons. The only way the Z^0 can contribute is through the decay to three photons in such a way as to mimic two photons in the detector. A strong upper limit is found by simply assuming that all three photon production mimics two photons and the internal loop graphs lead to a cross section as large as the first order Z^0 graphs, Fig. 4. Then

$$\sigma_{Z^0 \rightarrow \gamma\gamma} \lesssim \sigma_{Z^0} \alpha^3 .$$

If we now compare this to the two-photon annihilation cross section on the Z^0 resonance we find:

$$\frac{\sigma_{Z^0 \rightarrow \gamma\gamma}}{\sigma_{e^+e^- \rightarrow \gamma\gamma}} \lesssim \frac{M_Z}{\pi \Gamma_Z \alpha \ln(2\gamma)} \times \alpha^3 \lesssim 5 \times 10^{-5} .$$

This shows we can neglect the Z^0 when considering $e^+e^- \rightarrow 2\gamma$.

The total cross section for $e^+e^- \rightarrow 2\gamma$ can be written:^{2,3}

$$\sigma_{\gamma\gamma} = \frac{\pi\alpha^2}{E^2} \left[\ln(2\gamma) - \frac{1}{2} \right] ,$$

where E is the energy/beam. When this is compared to the total Z^0 cross section on resonance we find

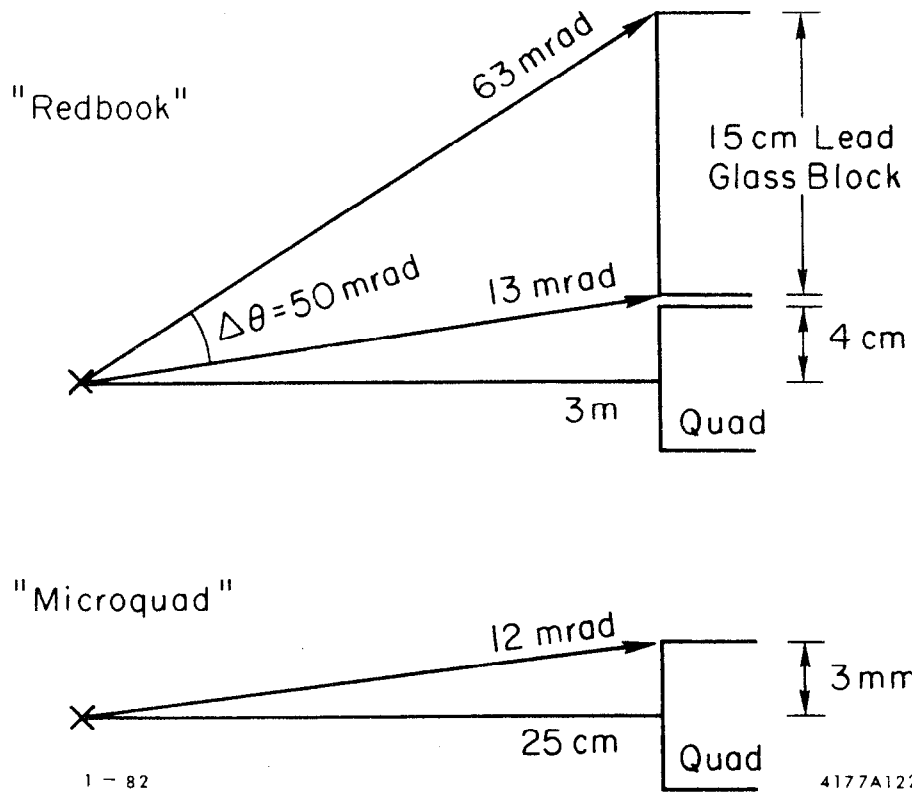


Fig. 1. Both the redbook design and the Micro-quadrupole design presently allow the interaction region to be viewed to angles smaller than 15 milliradians.

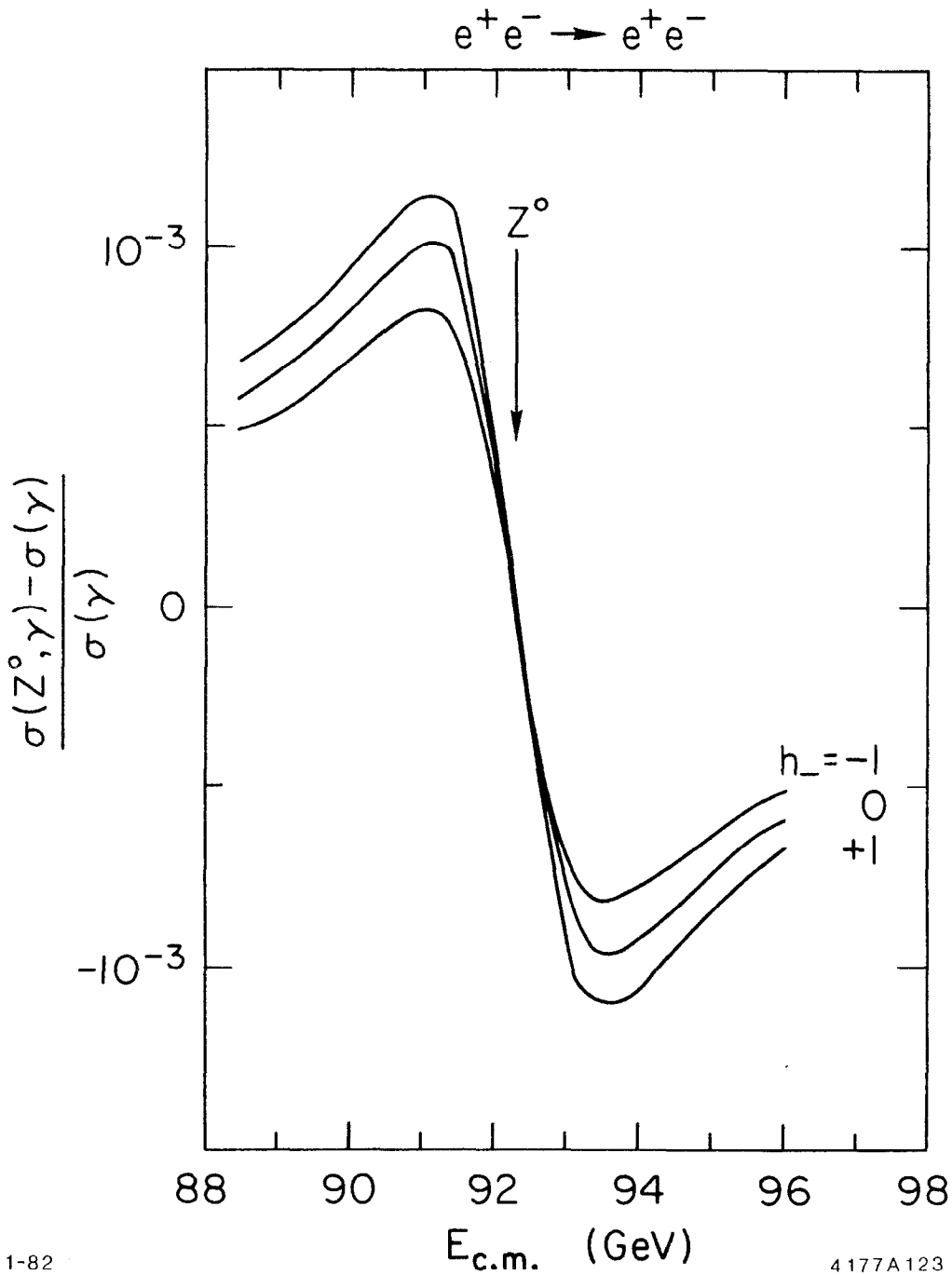
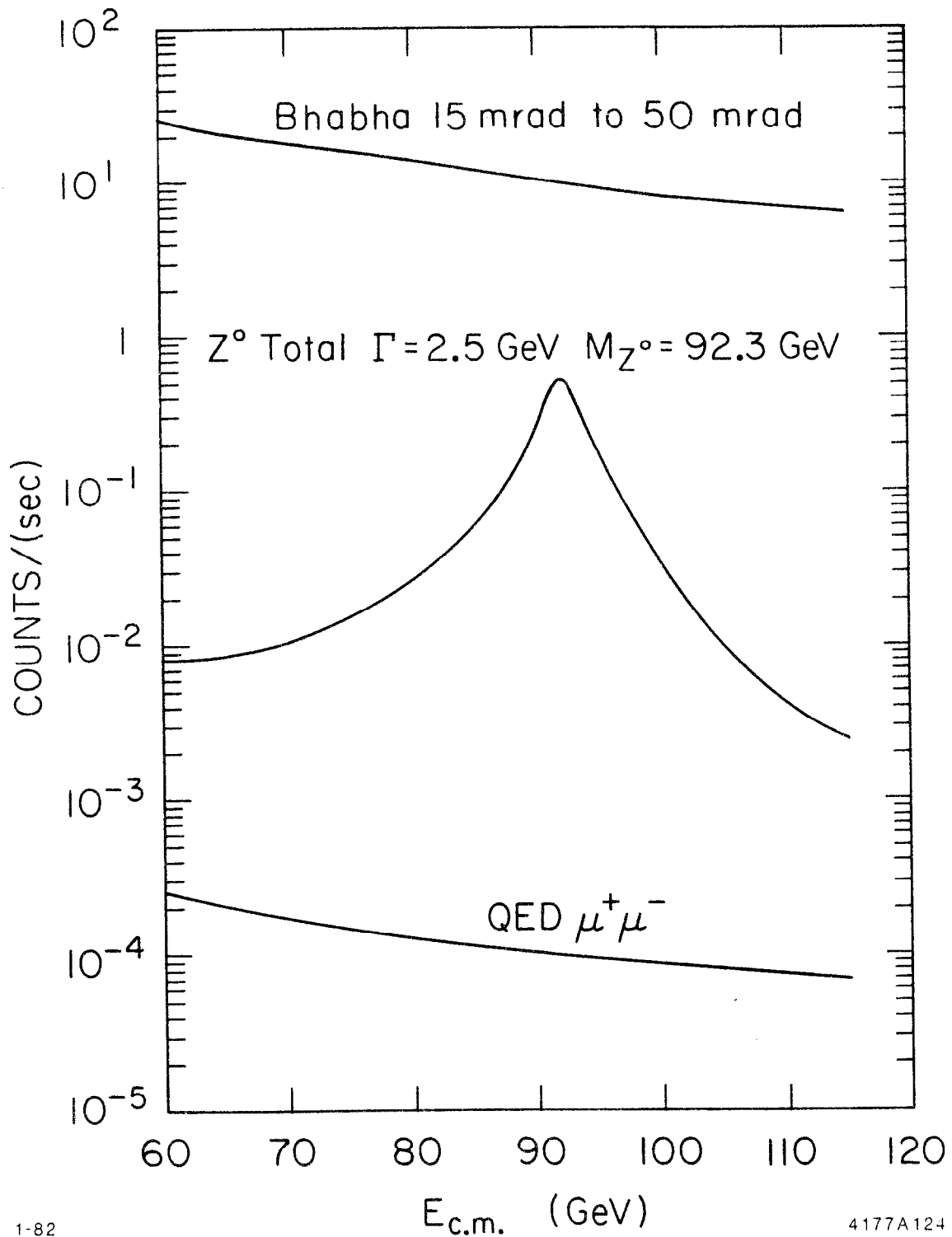


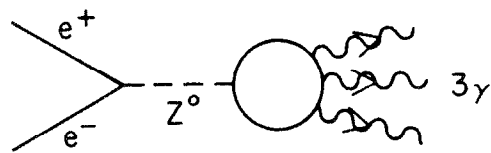
Fig. 2. The effect of the Z^0 and beam polarization on the Bhabha scattering rate. $\sigma(\gamma)$ is the QED cross section and $\sigma(Z^0, \gamma)$ is the electroweak cross section. The cross sections have been integrated over the luminosity monitor extending from 15 to 50 milliradians in θ and 0 to 2π in ϕ .



1-82

4177A124

Fig. 3. Relative event rates for the proposed Bhabha monitor, the Z^0 total cross section, and the QED cross section for $e^+e^- \rightarrow \mu^+\mu^-$. Rates are given as a function of the center of mass energy for a luminosity of $10^{31} \text{ cm}^{-2}\text{sec}^{-1}$.



1 - 82

4177A125

Fig. 4. Graph used to put an upper limit on the Z^0 "contribution" to $e^+e^- \rightarrow \gamma\gamma$.

$$\frac{\sigma_{\gamma\gamma}}{\sigma_{Z^0}} \sim 7.6 \times 10^{-3} .$$

The rate for the two photon process is thus two orders of magnitude below the Z^0 rate. Although the rate for $e^+e^- \rightarrow 2\gamma$ is low, because this process is free of the Z^0 it will be interesting to experimentally check it at high energies as a test of QED.

The differential cross section in the center-of-mass is:³

$$\frac{d\sigma}{d\Omega} = \frac{\alpha^2}{4E^2} \left[\frac{1 + \beta^2 + \beta^2 \sin^2 \theta}{1 - \beta^2 \cos^2 \theta} - \frac{2\beta^4 \sin^4 \theta}{(1 - \beta^2 \cos^2 \theta)^2} \right] .$$

If we now integrate this cross section over a detector which has 2π acceptance in ϕ but a limited acceptance in θ , we find:

$$\sigma \Big|_{\theta_a}^{\theta_b} = \frac{\pi\alpha^2}{2} \frac{1}{E^2} \left[\frac{(1 - \beta^2)^2 \cos \theta}{1 - \beta^2 \cos^2 \theta} - \frac{1}{2} \left(\frac{3 - \beta^4}{\beta} \right) \ln \left(\frac{1 + \beta \cos \theta}{1 - \beta \cos \theta} \right) + \cos \theta \right] \Big|_{\theta_a}^{\theta_b} .$$

Figure 5 shows this function with $\theta_a = 0$ as θ_b is varied. We find that the cross section is strongly peaked at small angles. 20% of the total rate is at angles below 100 microradians; 40% is below 1 milliradian.

If the $e^+e^- \rightarrow \gamma\gamma$ rate, into a luminosity monitor extending from 15 to 50 mrad, is compared to the Bhabha rate into the same monitor¹ then:

$$\frac{\sigma_{e^+e^- \rightarrow \gamma\gamma}}{\sigma_{\text{Bhabha}}} \sim 3 \times 10^{-5} .$$

This shows that we may neglect the two photon process as a background in a standard Bhabha luminosity monitor.

D. Conclusions

(1) While it is obvious from Fig. 3 that, at a rate of 10 Hz at the Z^0 , the monitor will not be useful for machine feedback and correction processes, nevertheless, it will be an important physics tool because the Z^0 contribution is less than 1/2% of the monitors observed rate.

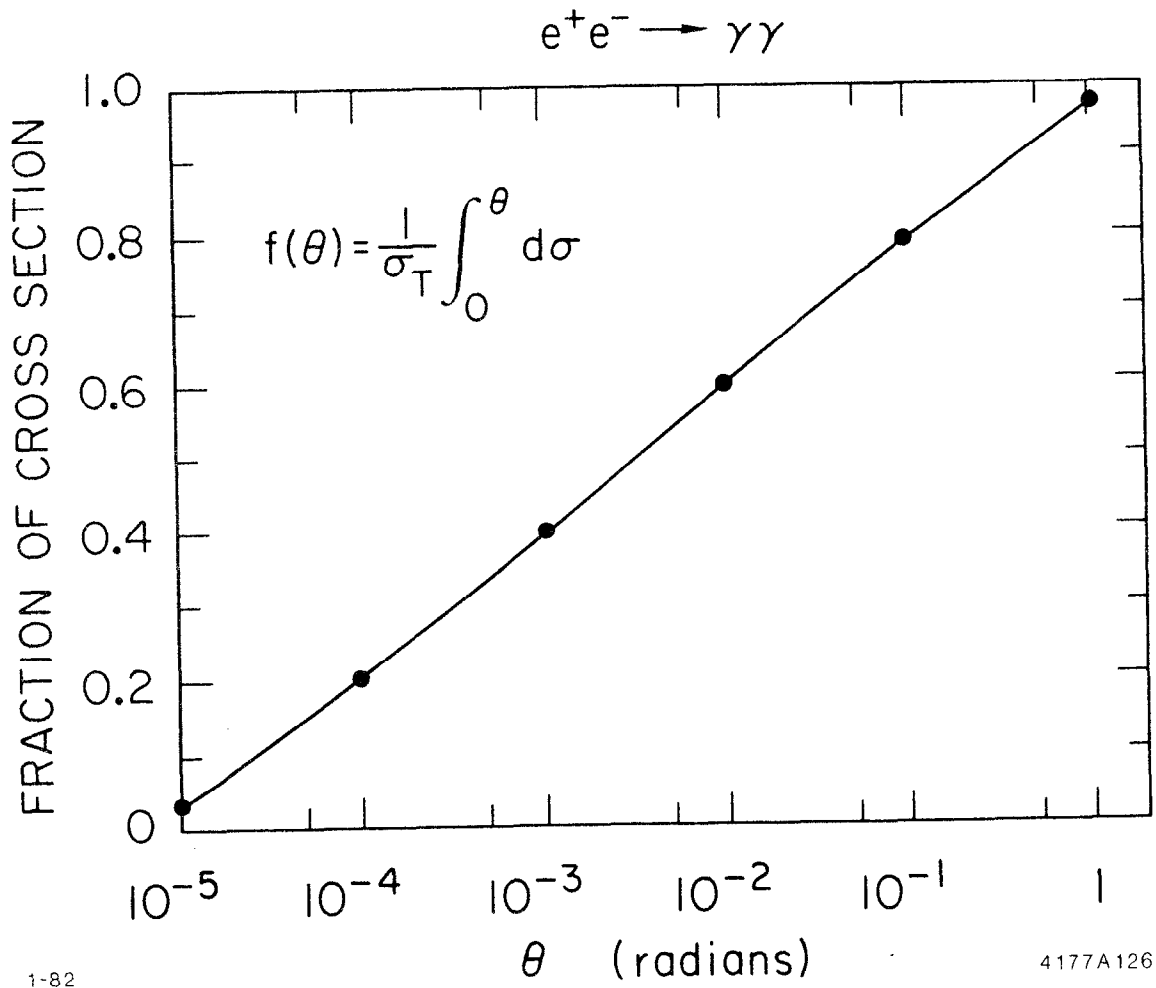


Fig. 5. Fraction of $e^+e^- \rightarrow \gamma\gamma$ cross section between $\theta = 0$ and $\theta = \theta$.

(2) It is important that we view the interaction region between 15 and 50 milliradians and have full azimuthal acceptance. This will allow the monitor to have a counting rate ~ 10 times larger than the total Z^0 rate.

(3) We note that for the "mini-quad" optics the angular region between 15 and 50 milliradians is blocked by the quadrupole nearest to the interaction point. This suggests that $e^+e^- \rightarrow \gamma\gamma$ at large angles may provide the best luminosity monitor even though the rates will be very low.

References

1. D. Koltick and J. Va'Vra, SLC Workshop Note No. 8.
2. D. Koltick, SLC Workshop Note No. 66.
3. W. Heitler, Quantum Theory of Radiation, Oxford (1966).
4. R. Budny, Phys. Lett. 55B, 227 (1975).

APPENDIX

The first order QED calculation of $e^+e^- \rightarrow e^+e^-$ yields the following equation:

$$\frac{d\sigma}{d\Omega} = \frac{\alpha^2}{8s} \left[\frac{4s^2}{t^2} + (1 - \cos\theta)^2 + (1 + \cos\theta)^2 \left(1 + \frac{s}{t}\right)^2 \right] . \quad (1)$$

The first order electroweak calculation has been done by R. Budny.⁴ For the case of transverse polarized beams, the result is:

$$\begin{aligned} \frac{d\sigma}{d\Omega} = \frac{\alpha^2}{8s} \left[4B_1 + (1 - \cos\theta)^2 B_2 + (1 + \cos\theta)^2 B_3 \right. \\ \left. + \lambda_+ \lambda_- \sin^2\theta \left\{ \cos(2\phi) B_4 + \sin(2\phi) B_5 \right\} \right] \end{aligned} \quad (2)$$

where λ is the transverse polarization of the beam. The B terms contain the weak couplings constants, and the Z^0 mass and width. The B terms are written below.

From Eq. (2) it can be seen that if only one beam is transversely polarized there will be no transverse polarization effects in the scattering rate. If both beams are transverse polarized, then the counting rate for a detector is not altered if the detector fills up 2π in ϕ , i.e., is a torus centered on the beam pipe. This shows we need not consider the effects of transverse polarization to study the effects of the Z^0 on Bhabha scattering. Setting the polarization to zero we find

$$\frac{d\sigma}{d\Omega} = \frac{\alpha^2}{8s} \left[4B_1 + (1 - \cos\theta)^2 B_2 + (1 + \cos\theta)^2 B_3 \right] . \quad (3)$$

For the case of longitudinal polarization we find after integration in ϕ

$$\begin{aligned} \frac{1}{\sin\theta} \frac{d\sigma}{d\Omega} = \frac{\pi\alpha^2}{4s} \left[(1 + h_- h_+) (4B_1) + (1 - h_- h_+) \left\{ (1 - \cos\theta)^2 B_2 \right. \right. \\ \left. \left. + (1 + \cos\theta)^2 B_3 \right\} + (h_- - h_+) (1 + \cos\theta)^2 B_6 \right] \end{aligned} \quad (4)$$

where h is the longitudinal polarization. From this equation, it can be seen that there are effects on the scattering rate which depend on the amount of longitudinal polarization. In the case $h_+ = h_- = 0$, Eq. (4) becomes identical to Eq. (3).

TERMS DEFINED

$$B_1 = |C_1|^2 \quad ; \quad B_2 = |C_2|^2 \quad ; \quad B_3 = \frac{1}{2} \left\{ |C_3 + C_4|^2 + |C_5 + C_6|^2 \right\}$$

$$B_4 = \text{Re} \left\{ C_2^* (C_3 + C_4 + C_5 + C_6) \right\} \quad ; \quad B_5 = \text{Im} (C_3 - C_5)$$

$$B_6 = \frac{1}{2} \left\{ |C_3 + C_4|^2 - |C_5 + C_6|^2 \right\}$$

$$C_1 = \frac{s}{t} \left[1 + (g_V^2 - g_A^2) Q \right] \quad ; \quad C_2 = 1 + (g_V^2 - g_A^2) R \quad ; \quad C_3 = \frac{s}{t} \left[1 + (g_V + g_A)^2 Q \right]$$

$$C_4 = 1 + (g_V + g_A)^2 R \quad ; \quad C_5 = \frac{s}{t} \left[1 + (g_V - g_A)^2 Q \right] \quad ; \quad C_6 = 1 + (g_V - g_A)^2 R$$

$$s = 4E_{\text{beam}}^2 \quad ; \quad t = -2E_{\text{beam}}^2 (1 - \cos\theta)$$

$$R = \frac{1}{e^2} \frac{s}{(s - M^2)^2 + M^2 \Gamma^2} \left\{ (s - M^2) - iM\Gamma \right\}$$

$$Q = \frac{1}{e^2} \frac{t}{(t - M^2)^2 + M^2 \Gamma^2} \left\{ (t - M^2) - iM\Gamma \right\}$$

$$g_L = \frac{e}{\sin\theta_\omega \cos\theta_\omega} \left[T_{3L} - q \sin^2\theta_\omega \right] \quad ; \quad g_V = g_R + g_L$$

$$g_R = \frac{e}{\sin\theta_\omega \cos\theta_\omega} \left[T_{3R} - q \sin^2\theta_\omega \right] \quad ; \quad g_A = g_R - g_L$$

Values Used:

$$M_{Z^0} = 92.3 \text{ GeV}/c^2 \quad ; \quad \Gamma_{Z^0} = 2.5 \text{ GeV}/c^2 \quad ; \quad \sin^2\theta_\omega = 0.23$$

$$\alpha = 2.07 \times 10^{-32} \text{ GeV}^2\text{-cm}^2$$

V. BEAM DUMPING

A. Introduction

It will be the primary function of the beam dumping system to transport both undisrupted and disrupted beams to a location where the beam power (~ 70 kW) can be safely dissipated and adequate radiation shielding can best be provided. An important but secondary function will be to provide the proper beam conditions that will allow measurement of the electron beam polarization using Møller scattering. This latter consideration contributes the greatest complexity to the solution. The feasibility of meeting these objectives has been demonstrated for a particular final focus (F-F) optics, specifically that known as the "mini-quad" solution.¹ Preliminary examination shows that most of the general features and many of the details of this solution will apply to other F-F configurations that include bends.

B. Description

With the exception of slight differences caused by the different momenta of the electron and positron beams and the second order effects to be discussed below, the centroid of each beam will retrace the trajectory of the opposing beam. Extraction is accomplished by perturbing this orbit with a fast kicker magnet followed by a septum magnet, see Fig. 1. At the septum magnet the beam receives the final angular kick to remove it from the F-F transport channel. This bend is in the plane perpendicular to the F-F bends; thus for these bends in the horizontal plane, as now assumed, the extracted beam will exit above the F-F bend plane. An opposite sign bend of equal magnitude will then turn the beam parallel to the F-F channel and remove the angular dispersion caused by the kicker and septum. The spatial dispersion here and at the dump is determined wholly by vertical distance between the two transport lines. As described below, this dispersion is removed only for the electron beam.

In the case of the unpolarized positron beam, additional optical elements are not necessary but may be desirable. The positron beam can be allowed to drift to the dump while retaining a reasonable size.

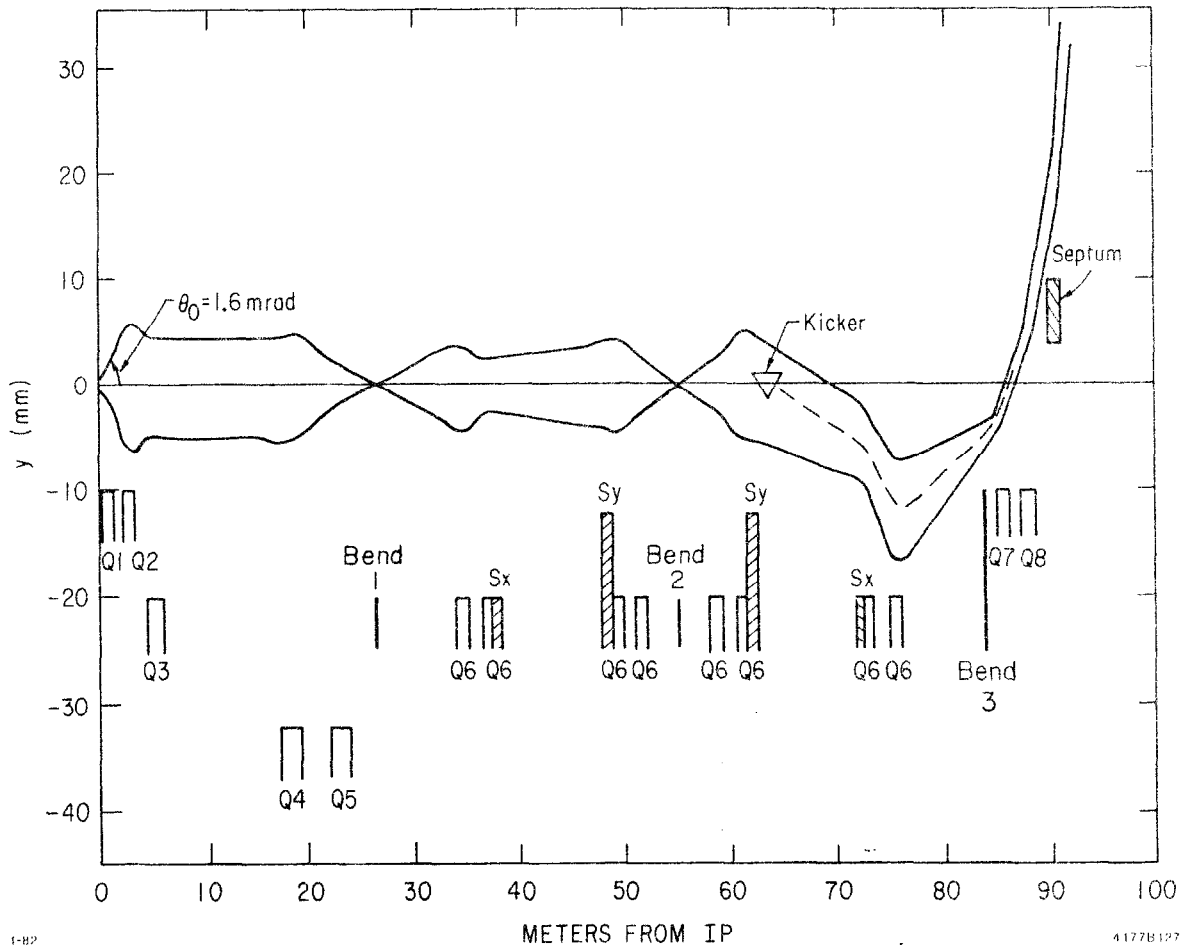


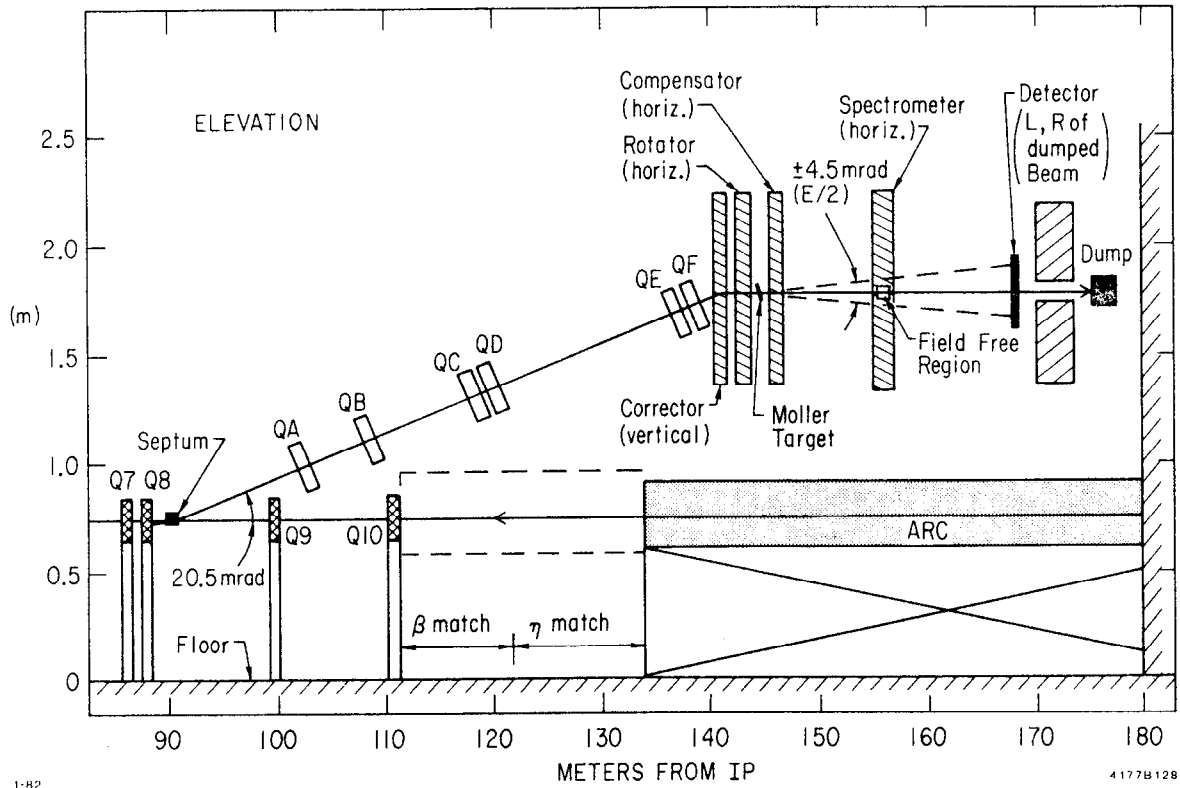
Fig. 1. Disrupted Beam Envelope (vertical plane) for the mini-quad optics; 1.6 mrad corresponds to the peak of the angular distribution.

Natural separation of the dump and F-F beamlines will occur at the commencement of the arc magnets (~134 meters from the IR) so by placing the dump 160 meters from the IR, separation adequate for shielding etc. is achieved.

In the electron beam, quadrupoles are placed between the septum magnet and the reverse bend magnet (called Corrector, see Figs. 2 and 3) to match the second order phase space projections of β , α , η and η' to those values required for polarization measurements. The beam then passes through two opposite polarity horizontal bending magnets which sandwich the Møller scatterer. These magnets are called the "Rotator" and "Compensator" and have the purpose of removing remnant transverse spin components in the horizontal plane (see Polarization below). The unscattered beam passes through a field free region of the Møller spectrometer magnet to the dump. The addition of matching elements and the polarimeter have the net effect of pushing the electron dump approximately 16 meters further downstream. This places the dump 175 meters from the IR, a distance in excess of that required for sufficient separation of beams. This solution, however is considered to be an existence proof; further study will be required to yield a shorter path.

C. Beam Parameters

During acceleration the positron beam leads the electron beam by 59 ns.² The theoretical curve of energy gain vs time for SLED II³ indicates the energy gain for the electrons will be 350 MeV greater than that of the positrons for both beams near 50 GeV. Assuming 5×10^{10} positrons, passage of the leading beam will leave a residual excitation of the fundamental mode that the electrons will see as a deaccelerating field (see Appendix A of Ref. 3 for discussion of longitudinal wake fields). This beam loading effect will decrease the electron energy by 850 MeV. The combined effects will leave the positrons with 500 MeV or +1% higher energy than the electrons. The F-F transport lines will be matched to each beam's momentum, thus calculated orbits for dumping the beams included a momentum shift of +1% (-1%) for positrons (electrons). When the beams undergo disruption, energy is lost to synchrotron radia-



1-82

4177B128

Fig. 2. Beam dump optics (elevation view) showing the septum magnet, beam dump line, elements of the polarimeter, and the location of the beam dump.

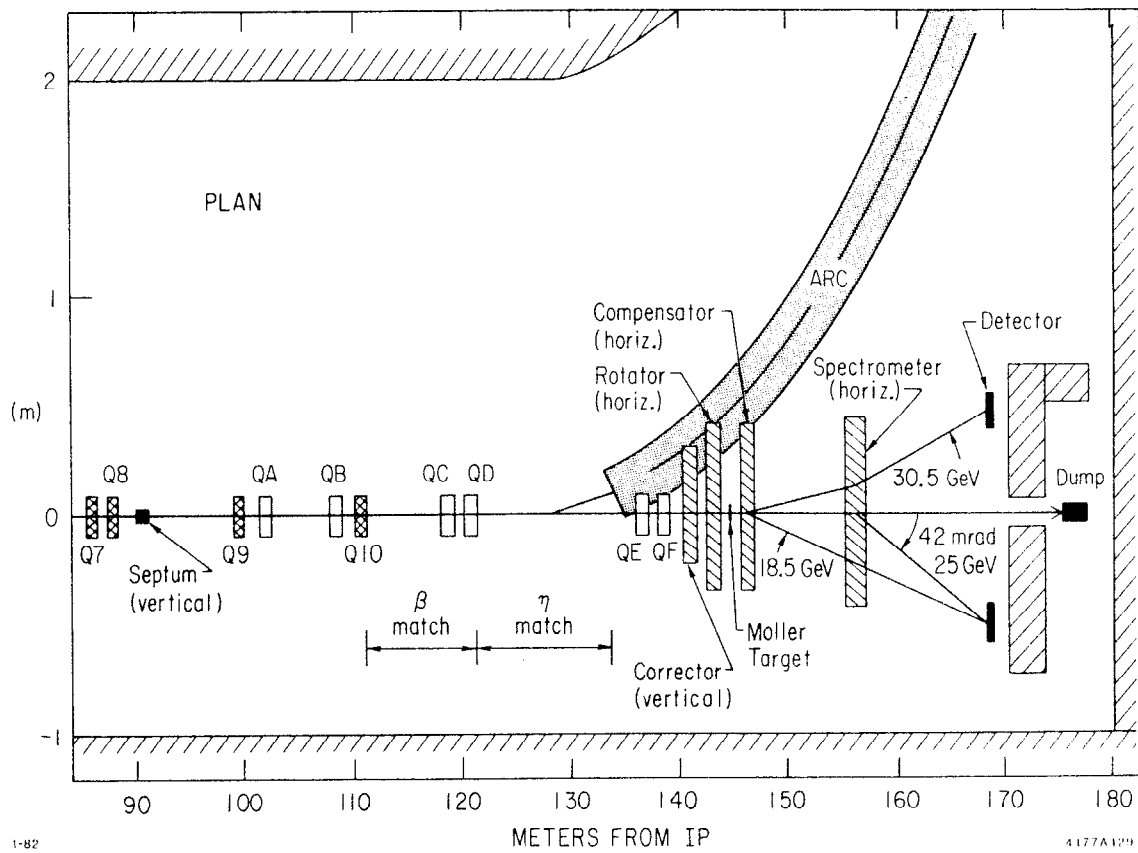


Fig. 3. Beam dump optics (plan view).

tion. The change in energy has been estimated for the beam parameters cited in Ref. 4 (5 mm beta*) to be -0.2%. Low energy tails in the disrupted beams have not been included, instead a Gaussian distribution with an appropriate shift of the mean and a width of 0.6% has been used.

Angular distributions for disrupted beams as calculated by R. Hollebeek⁴ have been included using a modified version of a ray tracing program, TURTLE.⁵

Summary of Beam Parameters (50 GeV)

	x-y (mm)	x'-y' (mrad)	dP (%)	rms (%)
Undisrupted beam e ⁺ (-)	0.001	0.245	+ (-) 1	0.5
Disrupted beam e ⁺	0.001	2.2*	+ 0.8	0.6
e ⁻	0.001	2.2*	- 1.2	0.6

* Hollebeek's distribution.

D. Polarization

The measurement of the longitudinal polarization of the beam at the IR using a polarimeter in the exhaust electron beam requires that the spin precess an integral multiple of π while traversing the 140 meters of intervening transport system. The fact that precession in horizontal and vertical bends is non-commutative require careful consideration of the ordering of the optical elements. With the exception of the small precession introduced by the kicker magnet the combination of large bends in the exhaust beam can be represented as (reading left to right):

$$H_{F-F} V_{SEPT} V^{-1} H_{ROT} = H_{F-F} H_{ROT} = n\pi$$

where V represents precession due to vertical bends, H_{F-F} that due to the F-F bends and H_{ROT} supplies the degree of freedom to satisfy the equality.

The F-F bend will remain fixed for all energies so the additional bend in the rotator magnet would imply large changes in the position of the beam at the dump. To compensate for this change in direction an additional magnet is needed downstream of the Møller target. This "compensator" magnet returns the beam to its original direction but with

an offset equal to the product of the rotator bend angle and the distance separating the magnets. The magnitude of this offset determines the minimum size of the field free region in the spectrometer magnet. The detail of the design of a practical spectrometer magnet will then determine the limit on the length and bend of the rotator magnet which in turn will determine the "band width" of energies where polarization can be measured. The scattered beam will also pass through the compensator; thus that magnet becomes part of the spectrometer. Field strengths and geometry for the compensator and spectrometer must be matched to allow measurement of the scattered beam momentum over the entire "band width".

For the particular F-F optics studied reasonable field strengths and geometry for first order trajectories can be obtained. However, ambiguities introduced by the azimuthal symmetry in the kinematics of Møller scattering will effect the acceptance and resolution of the polarimeter. In conjunction with the polarimeter group, examination is continuing to decide the efficacy of this system.

Before proceeding here are some practical relationships:

$$\begin{aligned} \theta_{\text{PREC}} &= \gamma \left(\frac{g-2}{g} \right) \theta_{\text{BEND}} \quad ; \quad \frac{g-2}{g} = 1.15965 \times 10^{-3} \\ &= 2.269E \theta_{\text{BEND}} \quad (\text{E in GeV}) \\ &= 0.69 B\ell \quad (B\ell \text{ in T-m, } \theta \text{ in radians}) \quad . \end{aligned}$$

It is worth remembering that for 50 GeV, $\theta_{\text{PREC}} = 113.5\theta_{\text{BEND}}$ and for all energies a field-length product of 2.3 T-m will precess the spin by $\pi/2$.

We have arbitrarily picked the field-length product of the rotator to match this condition of 90 degree spin rotation to calculate bandwidth and offsets for two examples of F-F optics:

	$\theta_{\text{F-F}}$	θ_{PREC} (50 GeV)	Bandwidth (GeV)
Mini-quad	3.24 ^o	368 ^o	37-61
Superconducting	1.38 ^o	157 ^o	29-86

It should be noted that it is possible to bias the midpoint of the bandwidth by addition of a bias magnet bending in the same plane as the F-F bends. Such a bend would be placed between the last vertical bend and the rotator and would have the effect of swinging the geometry of the polarimeter and the dump with respect to the direction of the F-F beam. The dispersion caused by this bend would have adverse effects and so this possibility has not been pursued.

The maximum error caused by neglecting spin precession in the kicker magnet may be estimated by seeing how much the kick angle has been magnified before the last F-F bend. Usually this term is close to unity and so the worst case error would be estimated to be less than twice the precession caused by the kicker itself. (This case would represent that energy for which a vertical precession is followed by a precession of 180 degrees in the horizontal plane.) Of course, the magnification of the kick angle becomes very large at the septum magnet but this magnification occurs between the last F-F bend and the septum and so can be completely corrected.

These considerations are valuable for designing the polarimeter beam but once designed it is necessary to check the results including all second order effects. A ray trace program called SPINTURT⁶ is being developed and has been used to calculate spin distributions at the Møller target for the 'mini-quad' dumping scheme. These distributions are shown in Figs. 4 and 5 for beam energies of 50 GeV and 36.7 GeV respectively.

E. Second Order Envelope

The phase space projections of $x-x'$ and $y-y'$ were investigated using second order TRANSPORT and TURTLE programs. The area of these emittance projections increases by orders of magnitude as functions of the disruption polar angle $\theta = \sqrt{(x')^2 + (y')^2}$. Since the second order optics is determined by the F-F optics, the only parameters free to be specified for the dumped beam will be the tolerance levels for higher order multipoles in the bends and focusing elements.

Using TURTLE these projections were measured at the point where the F-F and dumped beams separate. These emittances were used as input

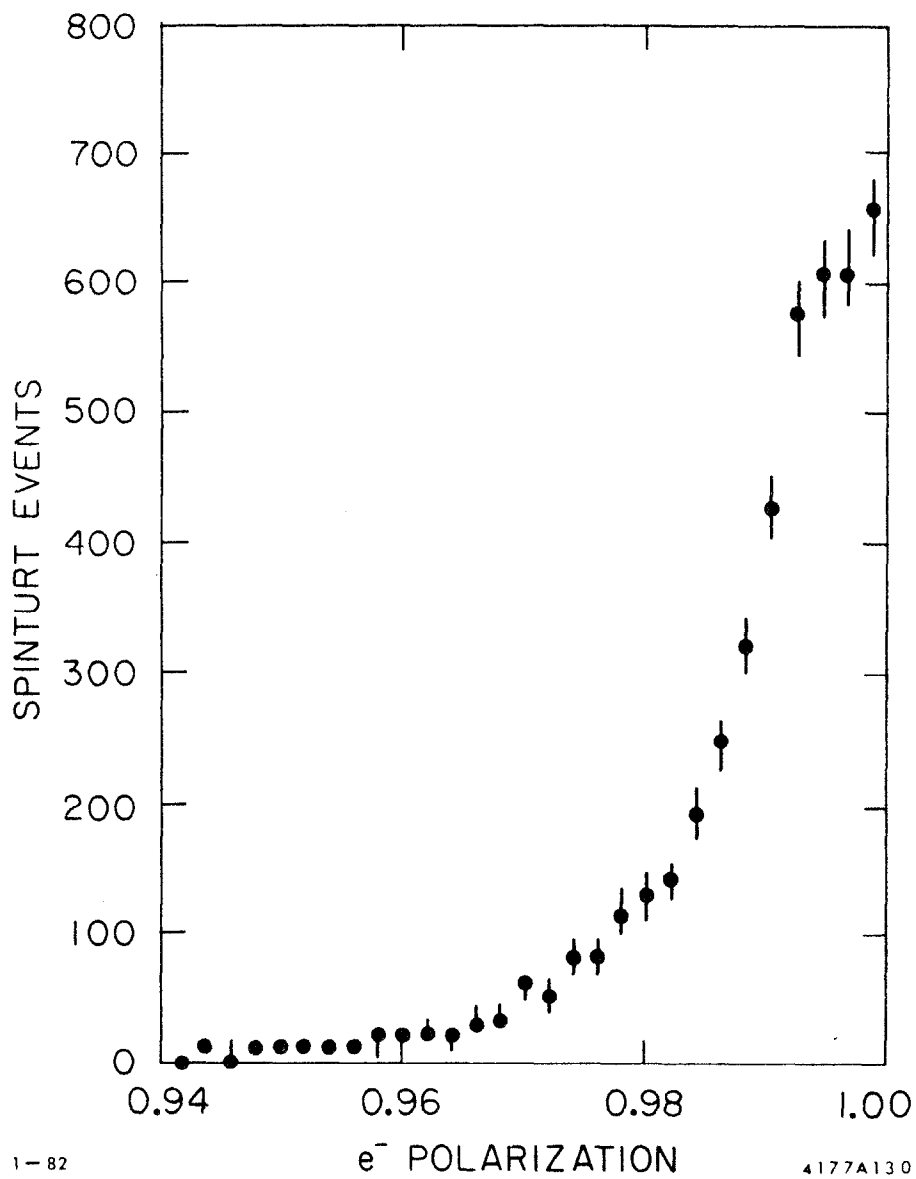


Fig. 4. e^- polarization at the Møller target relative to the central ray spin direction for 50 GeV beam energy. The central ray spin direction cosines are (+0.003, -0.145, +0.989) relative to the beam direction cosines (0,0,1).

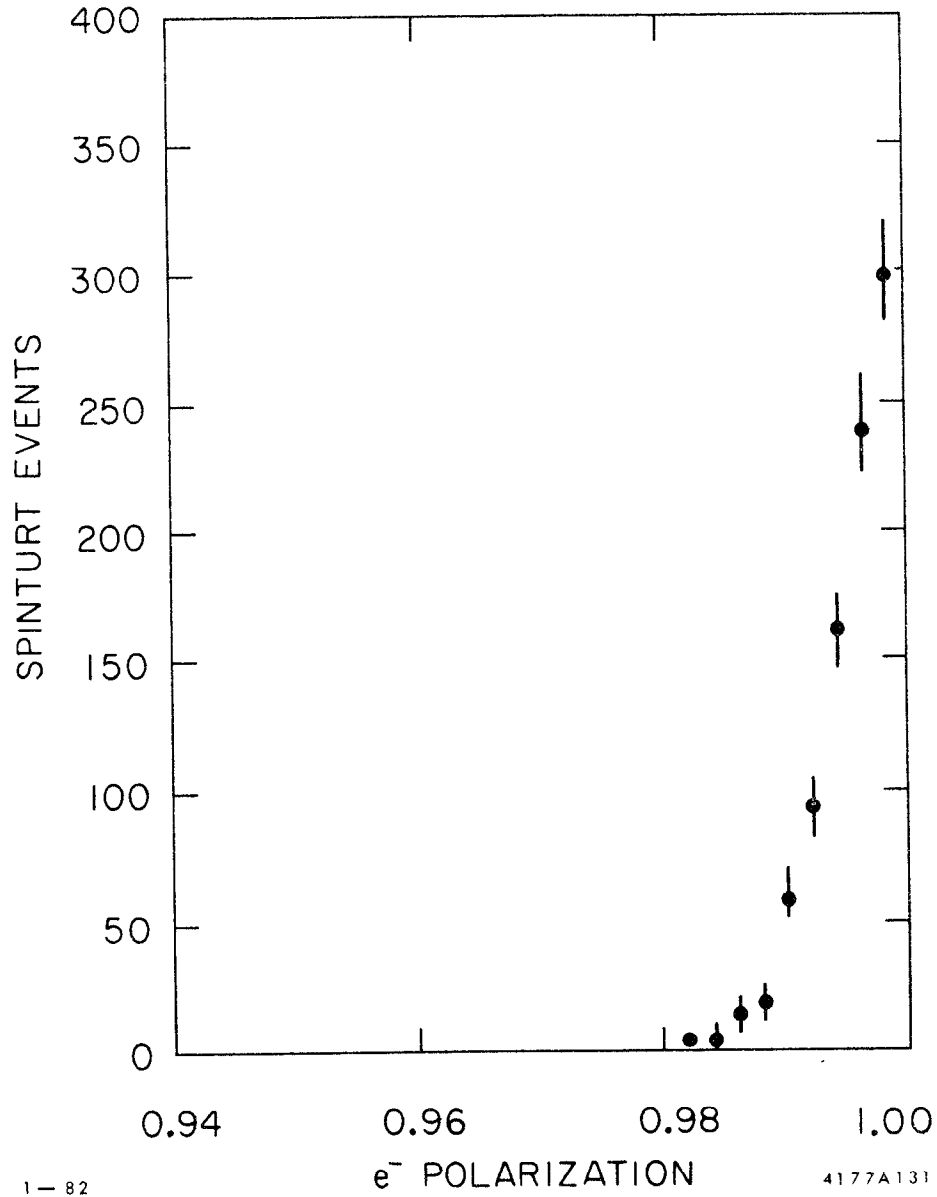


Fig. 5. e^- polarization at the Møller target relative to the central ray spin direction for 36.7 GeV beam energy. Central ray spin direction cosines are $(-0.05, -0.09, +0.995)$ relative to the beam direction cosines $(0,0,1)$.

to first order TRANSPORT to fit a matching section for the desired conditions at the Møller target. The fit conditions required erect ellipses in both the $x-x'$ and $y-y'$ planes, $\sigma_x = \sigma_y = 1$ mm, $\sigma_{x'} = \sigma_{y'} = 0.1$ mr and $\eta_x = \eta_y = \eta'_x = \eta'_y = 0$. These conditions correspond to the estimated upper limit⁷ for suitable parameters for polarization measurements.

Finally the result was checked using second order TURTLE with the disrupted beam parameters as input. The result of this calculation was $\sigma_x = 1.5$ mm, $\sigma_y = 1.6$ mm, $\sigma_{x'} = 0.12$ mr and $\sigma_{y'} = 0.13$ mr. Scatter plots of $x-y$, $x-x'$ and $y-y'$ at the target are shown in Figs. 6-8. In these figures the solid lines roughly indicate the half maximum level of the distributions. No significant correlations remain that can be removed by first order optics. As mentioned in the Polarization section, only detailed study of the polarimeter will determine the suitability of this beam.

Second order matching sections may be feasible, but at this time second order calculations with TRANSPORT and TURTLE do not agree in detail so they have not yet been attempted.

F. Extraction

Extraction is accomplished by perturbing the orbit with a fast kicker magnet allowing this perturbation to be magnified by the F-F optics, and finally separating the beams with a 15 mr bend in a septum magnet. The following conditions must be satisfactorily balanced to make this scheme work:

- (1) The distance between the kicker magnets and the IR must be sufficient to allow for attainable kicker rise times.
- (2) The kick angle must be less than or equal to that required to keep the second order beam envelope within the defining apertures of the F-F section between the kicker and the septum. This angle must be attainable.
- (3) The location of both magnets must be chosen such that the first order transfer matrix element $\langle y|y' \rangle$ is maximized between these magnets. The beam size also must be small compared to the offset at the septum.

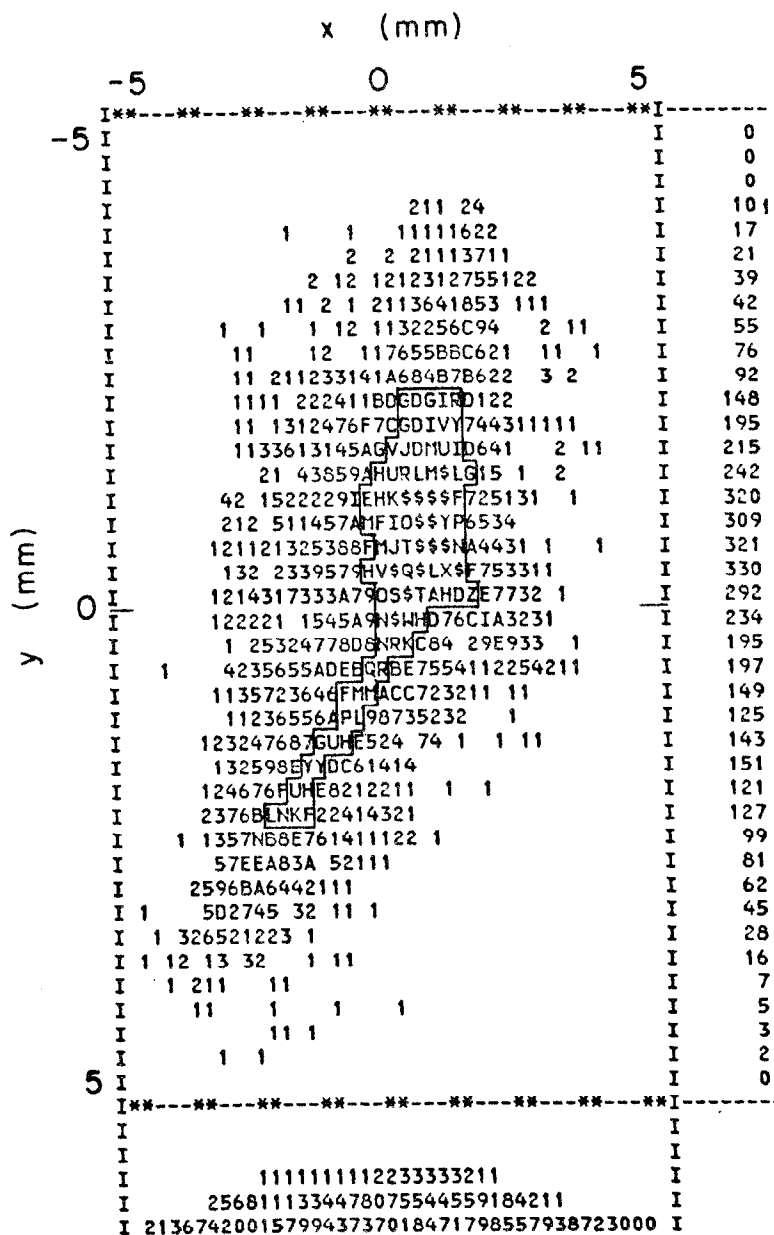


Fig. 6. Disrupted beam distribution at the Møller target:
 $\sigma_x = 1.5$ mm and $\sigma_y = 1.6$ mm.

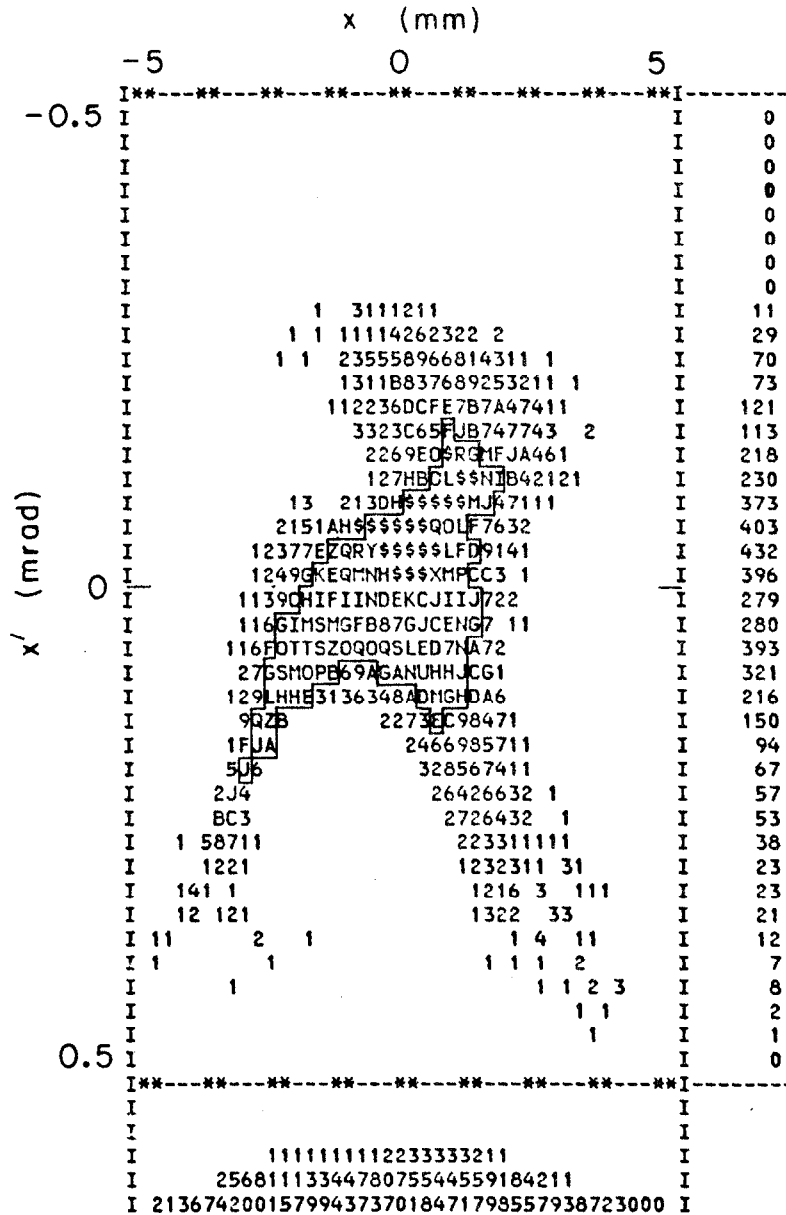


Fig. 7. Disrupted beam distribution at the Møller target:
 $\sigma_x = 1.5$ mm and $\sigma_{x'} = 0.12$ mrad.

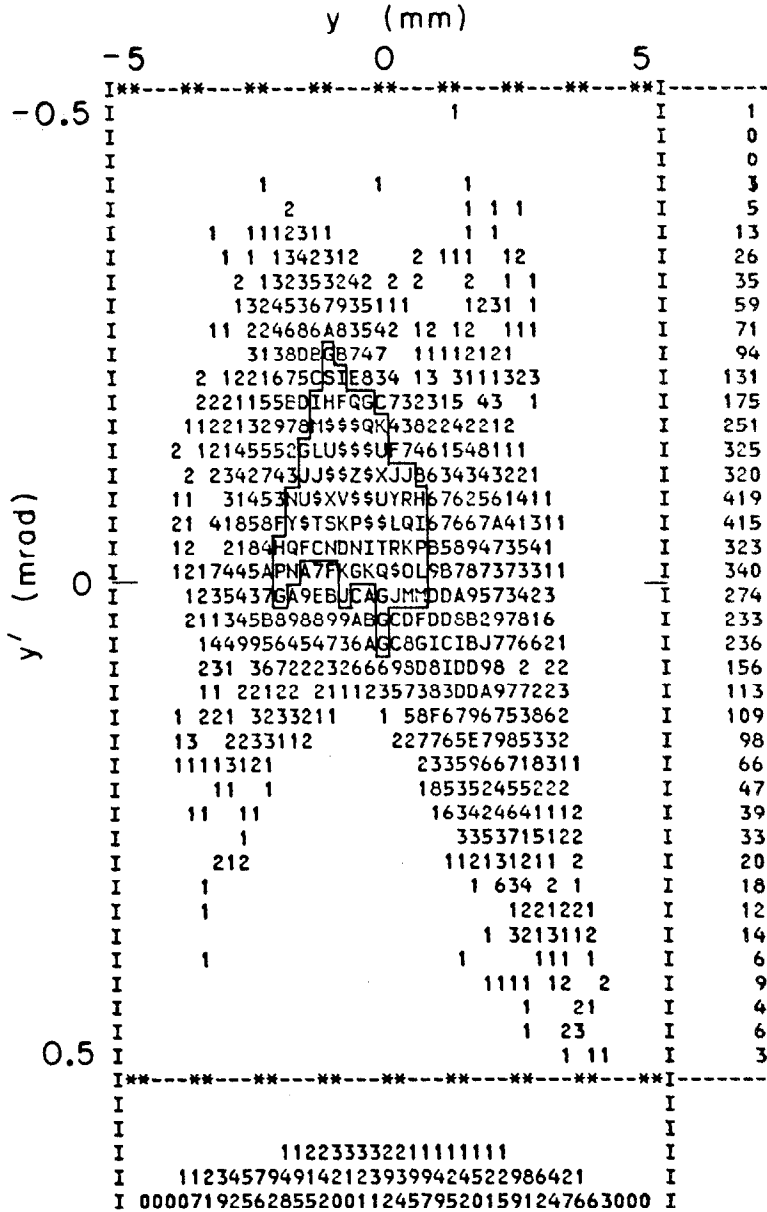


Fig. 8. Disrupted beam distribution at the Møller target:
 $\sigma_y = 1.6$ mm and $\sigma_{y'} = 0.14$ mrad.

(4) The location of the septum magnet must be chosen so that it is followed by sufficient drift space for the dumped beam to clear the following F-F element.

Each of the F-F solutions that included bend magnets was examined: in all cases extraction can be accomplished in the plane perpendicular to the F-F bend plane. The kick angle for all cases was close to 0.6 mr which is the exact value required for the mini-quad solution. The required parameters of 0.1 T-m and ~300 ns rise time are being examined,⁸ but appear to be feasible for a transmission line pulsed magnet.

Figure 9 shows a scatter plot of the beam envelope at the entrance face of the septum magnet. The beam is offset from the F-F beam by ~15 mm which will allow a current sheet of approximately 5 mm in the septum magnet. Similar magnets are being designed for the Damping Ring.

G. Beam Dumps

Two beam dumps are required to absorb and dissipate the spent beams after they leave the IR hall. The dumps are to safely handle the full design power of the SLC for both electrons and positrons. Beam parameters are: $E_0 = 50$ GeV, $N = 5 \times 10^{10}$ e⁻/bunch, PRR = 180 Hz. The resulting average power is $P_{av} \approx 70$ KW, and $I_{av} = 1.4$ μ A.

The proposed beam dump design is a SLAC sphere dump.⁹ The required dump diameter for adequate attenuation of the radial shower is ~25 cm, allowing for the expected excursion of the beam centroid. If the packed bed is made up of aluminum spheres, the dump will comfortably handle both the primary (undisrupted) and the disrupted beams. The dump window and the shell are also of aluminum. The window is ~0.5 cm thick, and absorbs 3 watts. Shower maximum for 50 GeV in aluminum occurs at $T_{max} = 6.2$ r.l., and shower multiplicity is $\Pi_{max}^{e^-} \approx 150$. The rate of energy deposition at T_{max} is:

$$P_{max}^1 = -\rho \frac{dE}{dx} I_{av} \Pi_{max}^{e^-} = 4.45 \times 10^6 \times 1.4 \times 10^{-6} \times 150 = 930 \text{ W/cm} .$$

The smallest expected spot size of the primary beam can be safely attenuated in a bed of 1 cm diameter water-cooled spheres. Approximately 15 r.l. (≈ 175 cm) are needed to attenuate the longitudinal shower to a

level where solid aluminum can be introduced. The packed bed is to be followed by 5 r.l. of solid aluminum (~45 cm), and then by ~30 r.l. of a higher Z material such as copper (~45 cm). This amounts to 50 r.l., and will adequately attenuate the longitudinal cascade; the resulting total dump length is 265 cm (\approx 8.7 ft.).

The desirable water velocity over the surface of the spheres is ~1 m/sec (~3 ft/sec). For a good packing factor (.74 hcp), the required flow rate is ~4 l/sec (65 gpm). This is dictated by heat transfer consideration rather than by bulk temperature rise, which is a modest 4°C. The pressure drop in the dump for this flow rate is ~7 psig.

For an average packing factor of 70%, approximately 11% of the incident beam power is directly dissipated in the cooling water. This causes radiolysis and results in evolution of free hydrogen at a rate¹⁰ of 0.3 l/(MW-sec), or 2.3×10^{-3} l/sec. After saturation, the radiolytically-evolved hydrogen collects principally in the gas space of the surge tank of the water system. For the required flow rate, and the size of system, the surge tank might have a gas space of 100l. The lower explosive limit (LEL) of H₂ in air is 4%. For practical operation, the concentration must never exceed 2%, and the trip level of the hydrogen sensors in the SLAC H₂-recombiner circuits is set at 1%. Thus, for this system, the trip level will be reached in ~7 minutes, and LEL in about 1/2 hour. One, therefore, should have a small hydrogen recombiner. The water system, of course, must be a radioactive water system, separated from the LCW system by a heat exchanger. Also required is a demineralizer/deionizer.

If space is at a premium, an entirely new beam dump could be designed which consists of water-cooled copper sheets, tailored in thickness to the demands placed on the material by the electromagnetic cascade. The downbeam end of the dump would be solid copper followed by a high-Z material like tungsten. Such a dump might be ~75 cm long, and would be more costly to produce than the aluminum sphere dump described above.

H. Shielding

Access to the collider areas, soon after beam operation has ceased, requires that the dump be shielded by the equivalent of a $\sim 1/2$ m of concrete. The same amount of shielding is required between the dump and the components of the radioactive water systems requiring periodic maintenance. A substantial amount of shielding, perhaps as much as 3 meters of concrete, will be necessary upstream of the dump to reduce background to the polarimeter and the IR hall.

Figure 10 shows a vertical cross-section at the final focus. Note that for 50 GeV beams, the muons from the electron dump are just barely contained within the earth. Calculations of radiation levels show that the muons must be completely ranged out to satisfy the site boundary conditions. At 70 GeV, we would have to bore further into the hill to provide room to add lead or depleted uranium behind the dump. Bending the beam down before it enters the dump is also a possible solution, but would require ~ 10 T-m, which is impractical. On the positron (north) side, the natural terrain is adequate to stop even 70 GeV muons.

References

1. T. Fieguth, L. Keller and D. Walz, SLC Workshop Note 67.
2. G. A. Loew, Stanford Linear Accelerator Report, CN-32 (1981).
3. SLAC Linear Collider Conceptual Design Report, SLAC-229 (1980).
4. R. Hollebeek, Stanford Linear Accelerator Report, CN-39 (1981).
5. K. L. Brown and C. Iselin, European Organization for Nuclear Research, CERN 74-2 (1974).
6. D. Burke and R. Stroynowski, private communication (1981).
7. C. Prescott, private communication (1981).
8. F. Bulos, private communication (1981).
9. D. R. Walz and L. R. Lucas, Stanford Linear Accelerator Center, SLAC-PUB-555; also IEEE Trans. Nucl. Sci. NS-16, No. 3, 613 (1969).
10. D. R. Walz and E. J. Seppi, Stanford Linear Accelerator Center SLAC-TN-67-29 (1967); also IEEE Trans. Nucl. Sci. NS-14, No. 3, 923 (1967).

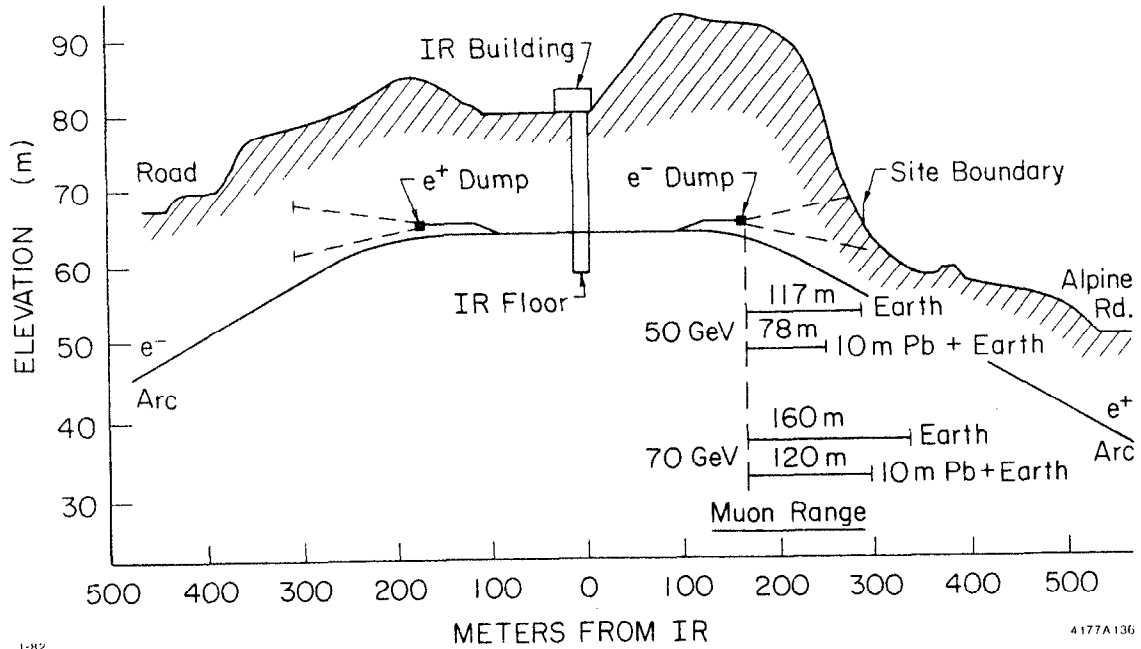


Fig. 10. Cross section of the SLC at the final focus showing the muon ranges. Earth shielding will satisfy boundary dose limit for 50 GeV muons; 70 GeV requires "high-Z" material behind the dump.

VI. BACKGROUNDS AT THE SLC

A. Introduction

In this section the detector backgrounds due to synchrotron radiation¹ from the final bending magnets and quadrupoles are evaluated along with the backgrounds from the beamstrahlung dump,¹ from beam-gas processes,² and from large angle synchrotron radiation.^{3,4} The two photon reaction $e^+e^- \rightarrow e^+e^-\mu^+\mu^-$ background to muon pair production at the Z^0 is also studied.⁵ Background estimates for the processes:⁶

- i) e^\pm beamstrahlung interactions ($e\gamma \rightarrow e\gamma$, $e\gamma \rightarrow eee$),
- ii) $\gamma\gamma$ beamstrahlung photon interactions ($\gamma\gamma \rightarrow ee$), and
- iii) two photon interactions ($e^+e^- \rightarrow e^+e^-X$)

are being reanalyzed,⁷ and are not presented here.

References

1. E. S. Miller and J. C. Sens, SLC Workshop Note 53.
2. D. Koltick, SLC Workshop Note 49.
3. D. B. Smith, SLC Workshop Note 69/SCIPP Internal Memo, 81/1.
4. D. Stork, SLC Workshop Note 68.
5. W. G. J. Langeveld, SLC "IR Group" Minutes, June 25, 1981.
6. SLAC Linear Collider Conceptual Design Report, Appendix E, SLAC-229 (1980).
7. D. B. Smith, SLC Workshop Note in preparation (SCIPP Internal Memo, 82/10; Collider Note 158).

B. Synchrotron Radiation and Disrupted Beam Backgrounds at the SLC Interaction Point

1. Introduction

In the following we evaluate the main sources of background in two configurations of the final focus system: the configuration with superconducting quadrupole magnets (SC-QUADS) and the configuration with mini-quadrupoles (MQ-QUADS). Both schemes are characterized by a β^* of 5 mm at the IP. The layout of the first few magnets in the vicinity of the IP is indicated in Table I. In the SC configuration the backgrounds have been calculated for two possible detectors, each filling 4π around the IP, with the exclusion of 30 mrad and 200 mrad cones, respectively, around the beampipe. In the MQ configuration there is no room for a detector extending to very small angles, hence only the 200 mrad case has been considered.

Backgrounds from various sources have been estimated in the Conceptual Design Report (SLAC-229, Appendix E). The main sources are synchrotron radiation (SR) from the bends, SR from the primary beams in the quadrupoles, and backscattering resulting from beam-beam interaction. Beam gas scattering resulting in bremsstrahlung photons and degraded electrons has been considered in Ref. 1. The contribution of two photon events to a two-pion topology at the Z^0 peak has been considered in Ref. 2.

In the following the SLC has been assumed to have 5×10^{10} electrons per beam, at 50 GeV. The disrupted beam stay-clear angle has been taken to be 2.5 mrad.

2. Positioning of the Masks

In either final focus scheme a soft bend is placed between the IP and the nearest hard bend in order to deflect the primary beam and let the SR generated in the hard bend be intercepted by a primary mask, M1. The minimum aperture of this mask is chosen such that the disrupted beam and the associated photons are not intercepted. By placing the mask as close as possible to the interaction region, and by making the soft bend magnet as long as the layout of the lattice will permit, the soft bend field required to intercept all the hard bend radiation is kept to

Table I. Magnet Layout Near the Interaction Point for Superconducting (SC) and Mini (MQ) Quadrupole Final Focus Optics

	SC-QUADS				MQ-QUADS		
	Length (m)	(Poletip) Field (KG)	Aperture Radius (mm)		Length (m)	(Poletip) Field (KG)	Aperture Radius (mm)
INTERSECTION	-	-	-	INTERSECTION	-	-	-
DRIFT SPACE	4.5	-	-	DRIFT	0.25	-	-
QUAD	0.75	37.48	35	QUAD	1.67	8.00	10
SEXTUPOLE	0.75	4.77	35	DRIFT	0.25	-	-
DRIFT	0.25	-	-	QUAD	1.65	-8.15	10
QUAD	0.60	-37.34	35	DRIFT	0.50	-	-
SEXTUPOLE	0.75	-6.00	35	QUAD	1.80	8.15	20
DRIFT	0.26	-	-	DRIFT	0.30	-	-
SOFT BEND	18.00	0.266	-	SOFT BEND	11.00	0.667	-
DRIFT	0.26	-	-	DRIFT	0.30	-	-
QUAD	0.70	36.94	70	QUAD	1.50	-9.76	50
DRIFT	0.98	-	-	DRIFT	2.77	-	-
QUAD	0.70	-36.75	70	QUAD	1.50	7.39	60
DRIFT	0.50	-	-	HARD BEND	5.00	4.72	-
HARD BEND	5.00	8.49	-	DRIFT	5.50	-	-
DRIFT	0.50	-	-	QUAD	0.75	-11.72	20
QUAD	0.70	-36.75	70				

a minimum. This in turn will minimize the critical energy of the SR generated in the soft bend and thereby diminish or eliminate background due to photo-produced neutrons in the detector.

Table II indicates the number of SR photons per electron and their critical energy for the two magnet configurations. For the SC-QUADS the primary mask is placed at 8.3 m; for the MQ-QUADS at 7 m from the IP. As shown in Ref. 3, a critical energy of ~ 1 MeV for the hard bend SR results in $\sim 8 \times 10^4$ neutrons per crossing in Pb; they would be stopped in a thickness of ~ 1 m.

A secondary mask, M2, is placed closer in and intercepts part of the soft bend SR (SBSR). It need not be more than a few cm thick since the SB critical energy is well below the threshold for producing neutrons. We assume that all SR from the soft bend of the same side of the IP hitting the face of this mask is fully absorbed. This then leaves the edge scattering from the same side and the backscattering of the SBSR from the opposite side to be considered as the remaining sources of soft bend background.

The reflected and edge scattered photons from M2 will in part escape along the beam line, in part scatter coherently on the core of the quadrupoles between M2 and IP or reflect from the face of the quads at the opposite side of the IP, and in part reach the detector directly. In order to eliminate the latter category, we assume the detector to be lined with shielding material arranged to prevent single bounce photons from reaching the detector, without intercepting direct (first order) photons from the soft bend. With the detector lining (M3) in place, no soft-bend photon can then reach the detector without having scattered at least twice.

3. Scattering and Fluorescence on the Masks

At the energies characteristic for the soft bend, 40-100 KeV, incoherent, backward Compton scattering and photoelectric absorption, followed by fluorescence are the main contributors to scattering off the interior of M2. Edge scattering off M2 is mostly coherent, forward, Compton scattering. A fraction of the photons from M2 strikes M3 and reaches the detector via a coherent, small angle scatter on the lining.

Table II. Synchrotron Radiation from Hard Bend and Soft Bend
Dipoles Nearest the Interaction Point.

Configuration	γ/e	Critical Energy K_c (KeV)
<u>SC-QUADS</u>		
Hard Bend	24	1302
Soft Bend	3.0	44
<u>MQ-QUADS</u>		
Hard Bend	14.6	783
Soft Bend	4.5	111

We thus have four sources of soft bend photons into the detector: reflection and fluorescence from the M2 interior, and small angle scattering and fluorescence from the M2 edge, all followed by small angle scattering from the lining M3.

The probability factors, F , for the four two-bounce processes above are each governed by the ratio σ/σ_a , i.e., by the product of the probability for scattering or fluorescence (σ) and the probability for the photon not to get lost through absorption ($1/\sigma_a$) on the way into or out of the mask material. The factors F are derived in Appendix A. The derivations are similar to the ones in a note by R. Larsen,⁴ the difference being that the F 's calculated in Appendix A are convolution integrals over the energy dependence of the scattering on M2 and M3.

For the first source, reflection off the face of M2 and scattering off M3 we have (Eq. A1 in the Appendix)

$$F_1 = \frac{0.15}{n_T} \int_0^\infty \left(\frac{\mu_s}{\mu_a} (K) \right)_{\text{INCOH}} \left(\frac{\mu_s}{\mu_a} (K') \right)_{\text{COH}} \frac{dn}{dK} dK \quad . \quad (1)$$

Here, the first and second factors in the integral are the probabilities for incoherent scattering of a photon on M2 and coherent scattering on M3. The coefficient μ_s is respectively the mass coefficient for incoherent Compton, and coherent (Rayleigh) scattering for bound electrons, μ_a is the photoelectric mass absorption coefficient. The numerical values have been taken from Ref. 5 and are reproduced in Table III. The photon energy K' for backward scattering is related to K by

$$\frac{K'}{m_e} = \frac{\alpha}{1+2\alpha} ; \quad \alpha = \frac{K}{m_e} ; \quad m_e = \text{electron mass} \quad . \quad (2)$$

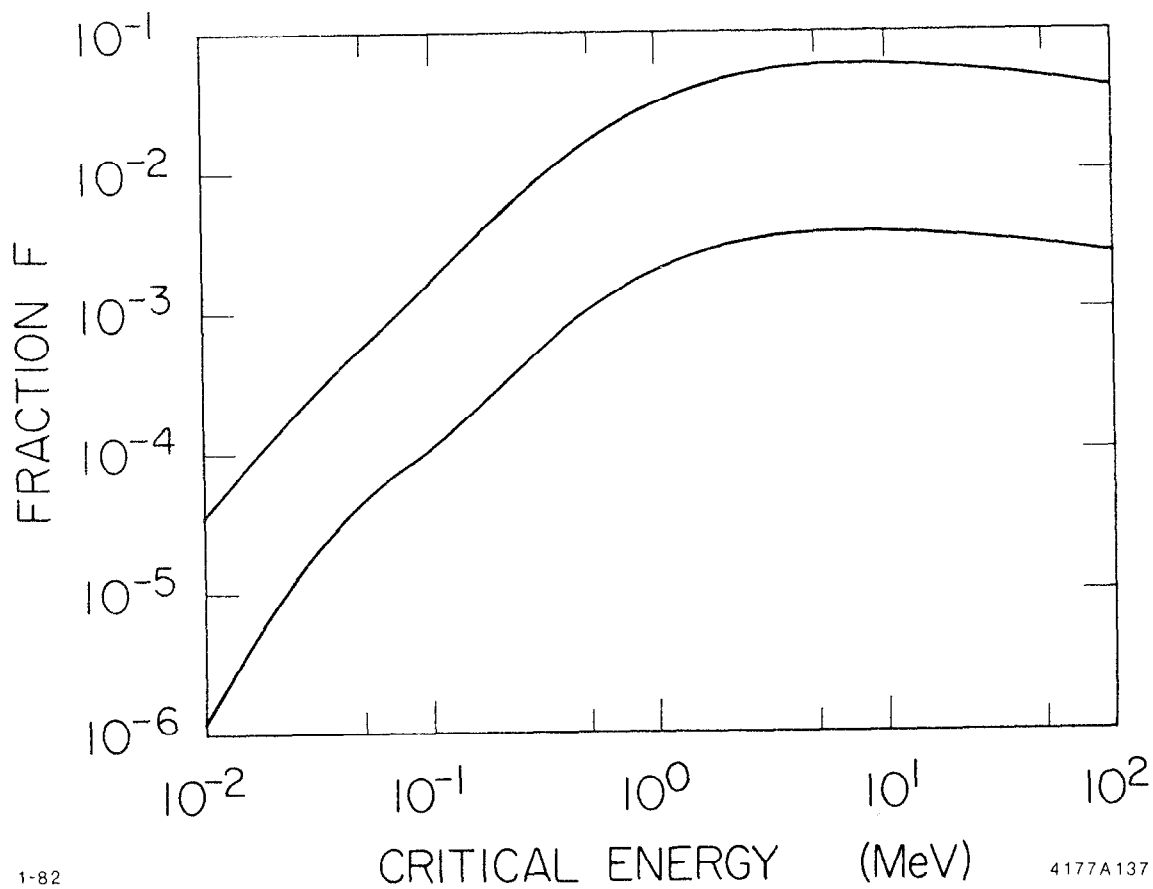
Figure 1 shows the dependence of F_1 on the critical energy K_c . For later reference, the factor for scattering on M2 only is also shown. The factor 0.15 in Eq. (1) arises from averaging over angles in the scattering in M2. For the second bounce on M3 it is assumed that scattering into as well as out of the detector lining will result in photons into the detector, therefore the solid angle has been taken to be 2π .

Table III. Mass Scattering and Absorption Coefficients (cm²/g)[†]

K (MeV)	Compton Scattering μ_s (INCOH)	Rayleigh Scattering μ_s (COH)	Photoelectric	
			Total μ_a^*	Absorption μ_{aa}^*
.01	.15	4.97	123.	123.
.013035	.147	3.87	62.2	62.2
			159.01	127.
.015	.146	3.31	107.	88.4
.0152	.146	3.26	104.	86.3
			145.64	114.
.015861	.145	3.11	131.	104.
			151.75	119.
.02	.142	2.34	82.8	68.3
.03	.135	1.38	28.5	25.1
.04	.129	.913	13.2	12.0
.05	.123	.642	7.15	6.66
.06	.118	.48	4.36	4.1
.08	.109	.294	1.98	1.89
.088004	.106	.246	1.53	1.47
			7.2094	2.48
.1	.101	.195	5.23	2.21
.15	.0866	.0919	1.82	1.12
.2	.0759	.0532	.849	.605
.3	.0616	.024	.294	.237
.4	.052	.0136	.142	.121
.5	.0453	.00878	.0826	.073
.6	.0404	.0061	.0541	.0488
.8	.0331	.00343	.0287	.0266
1.0	.282	.00221	.0181	.017

[†] E. Storm and H. I. Israel, Nuclear Data Tables A7, 567 (1979).

* $\mu_{aa} = f\mu_a$, where f is the average fraction of photon energy transferred to electrons as a result of photoelectric absorption.



1-82

4177A137

Fig. 1. Fraction of synchrotron radiation reflected off mask M2 interior surface (upper curve) followed by scattering off the detector (M3) lining (lower curve) as a function of the synchrotron spectrum critical energy.

The fraction of photons absorbed on M2 with subsequent emission of a fluorescent photon is given by (Eq. A2, Appendix):

$$F_2 = \frac{G}{2n_T} \left(\frac{\mu_s}{\mu_a} (K_\alpha) \right)_{\text{COH}} \int_{K_{\min}}^{\infty} \left[1 + r \ln \frac{r}{1+r} \right] \frac{dn}{dK} dK \quad (3)$$

with the notation of the Appendix. Unlike for F_1 , the effect of the lining M3 is energy independent and reduces the rate of photons into the detector by a constant factor of ~ 7 .

Figure 2 shows the dependence of F_2 on the critical energy K_c , for the one- and two-bounce cases.

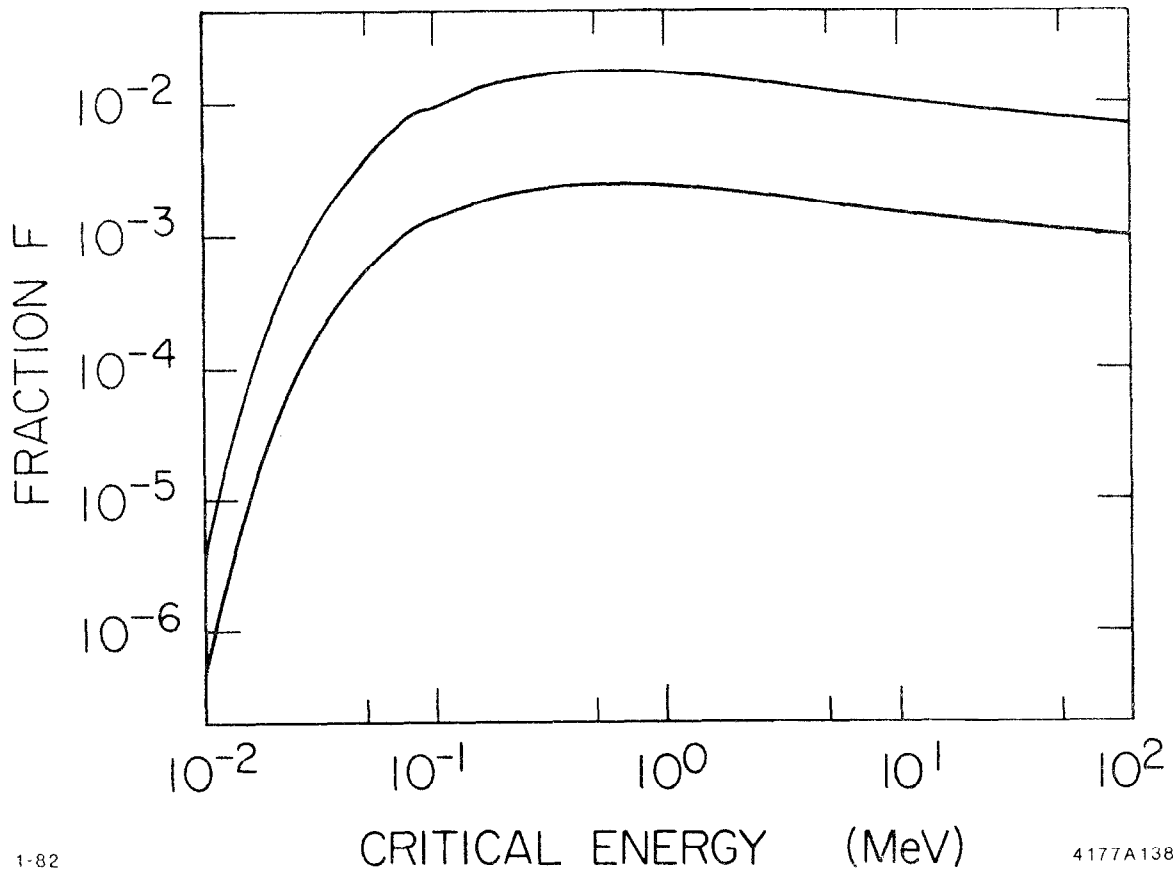
The third source of photons is due to forward, coherent scattering off the edge of M2, followed by a second forward coherent scatter on the lining M3. It is easy to see that this contribution can be reduced strongly by tapering the edge and making the wedge angle equal to the angle of incidence of the soft bend photons. In that case we have for edge scattering on M2 followed by a second coherent scatter off M3 (Eq. A3, Appendix):

$$F_3 = \frac{1}{n_T} \int_0^{\infty} \left(\frac{\mu_s}{\mu_a} (K) \right)_{\text{COH}}^2 \frac{\theta_s}{\mu_a} \frac{1}{\rho \Delta z} \frac{dn}{dK} dK \quad (4)$$

where θ_s is the average angle of scattering into the detector in a single scatter and ρ is the density of the mask. The photon energy is essentially unchanged in the succession of two coherent scatters.

Figure 3 shows the dependence of F_3 on the critical energy K_c , for the one- and two-bounce cases.

Fluorescence off the edge of M2 is described by an expression similar to F_3 , the difference being that the escape probability of the exiting photon is now controlled by the mass absorption coefficient at the K_α X-ray energy. We have, for fluorescence off M2 and scattering off M3 (Eq. A4, Appendix):



1-82

4177A138

Fig. 2. Fraction of synchrotron photons absorbed on mask M2 inner surface with subsequent fluorescent emission (upper curve), followed by scattering off the detector (M3) lining (lower curve) as a function of the synchrotron spectrum critical energy.

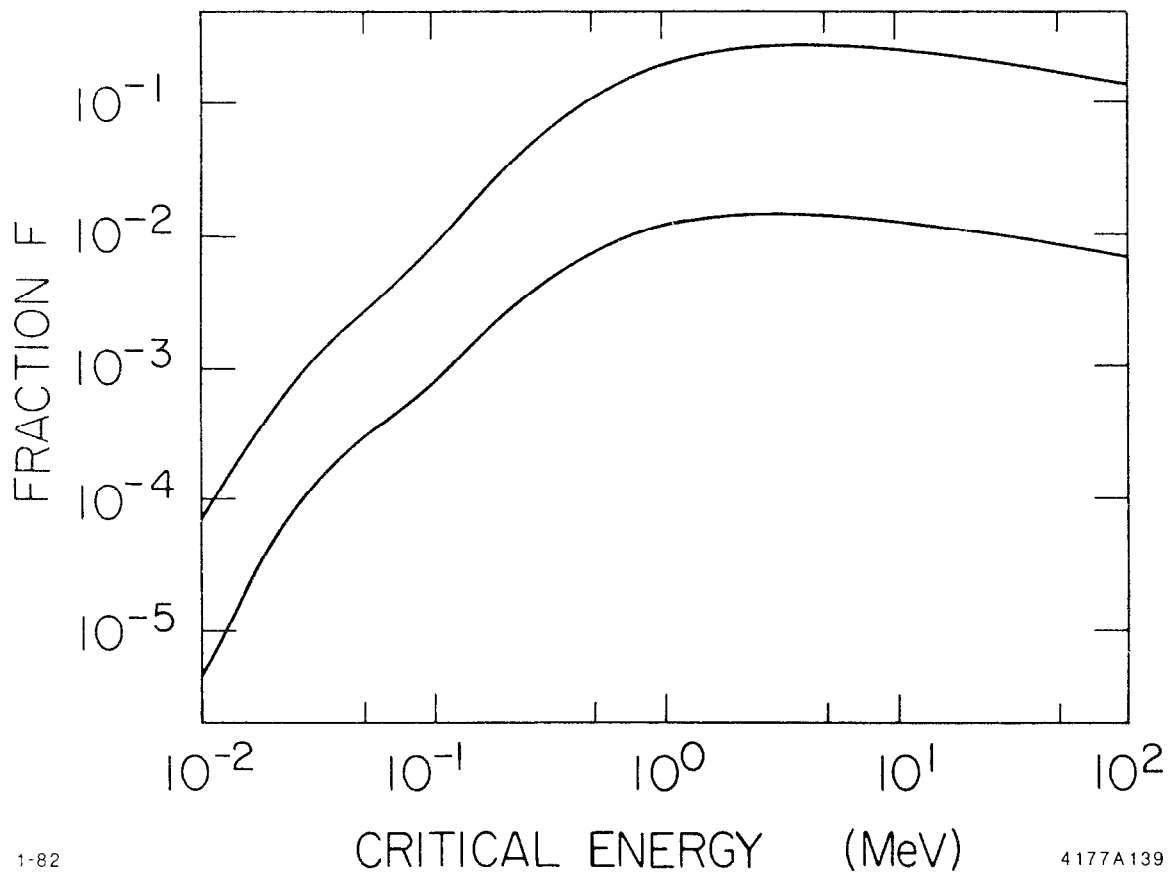


Fig. 3. Fraction of synchrotron radiation scattered off mask M2 edge surface (upper curve) followed by scattering off the detector (M3) lining (lower curve) as a function of the synchrotron spectrum critical energy.

$$F_4 = \frac{G}{n_T} \int_{K_{\min}}^{\infty} \left(\frac{\mu_s}{\mu_a} (K_\alpha) \right)_{\text{COH}} \frac{\theta_s}{\mu_a (K_\alpha)} \frac{1}{\rho \Delta z} \frac{dn}{dK} dK \quad (5)$$

Figure 4 shows the dependence of F_4 on the critical energy.

4. Geometrical Factors

The yield of photons per crossing into the detector, due to the processes 1-4 above, is given by

$$Y = \text{FLUX} * \text{F-FACTOR} * \text{SOLID ANGLE} \quad (6)$$

where, for scattering and fluorescence on the face of M2, the FLUX is the number of photons striking the mask, and for scattering and fluorescence off the edge of M2 the FLUX is the number of photons per radian. For reflection and fluorescence off the face of M2 we have, for two beams of 5×10^{10} particles of 50 GeV each

$$\text{FLUX} = 2 \times 5 \times 10^{10} \times 1031 \left(\frac{\gamma}{e^+} \right)_{\text{rad}} \times \Delta\theta \text{ photons} \quad (7)$$

where $\Delta\theta$ is the angular interval subtended by the mask at the soft bend center. For edge scattering and fluorescence we have

$$\text{FLUX} = 2 \times 5 \times 10^{10} \times 1031 \text{ photons/rad} \quad (8)$$

The SOLID ANGLE subtended by the detector lining to the photons from M2 has been calculated for the SC and MQ-QUADS, for 30 and 200 mrad detectors and two positions of M2. At each position the inner radius of M2 is adjusted to just clear the disrupted beam. The detector lining is shaped such that its boundary forms an aperture stop at the point where the limiting angle of the detector (30 or 200 mrad) intersects the "Quadrupole SR(QSR) stay-clear limit" to be discussed in Sect. VI, below.⁸ The radius, x_a , and the distance from IP, z_a , of this aperture stop are a function of the position of M2. The solid angle subtended by the detector lining to the once-reflected or fluorescent photons is then determined by the space between two cylinders, at $\pm z_a$, of lining material viewed from the beam axis at the position of M2.

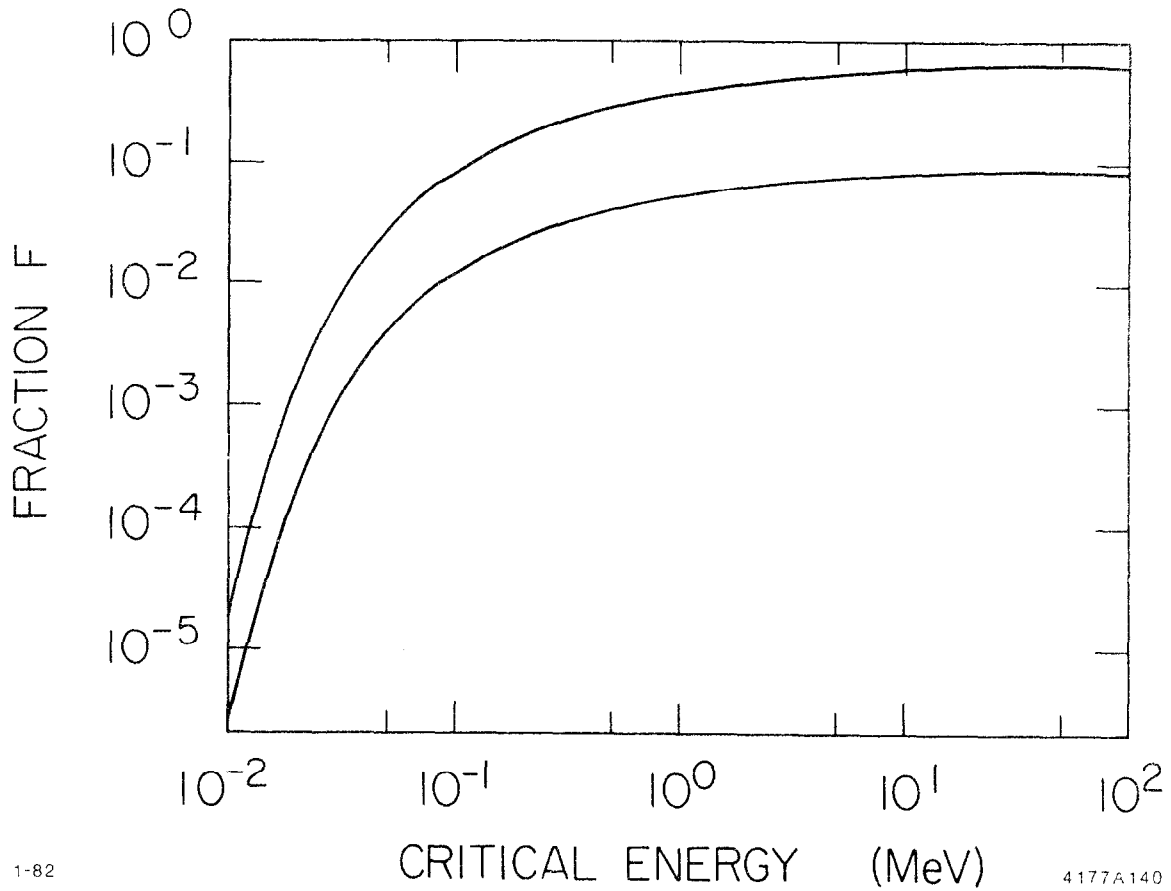


Fig. 4. Fraction of synchrotron photons absorbed on mask M2 edge surface with subsequent fluorescent emission (upper curve), followed by scattering off the detector (M3) lining (lower curve) as a function of the synchrotron spectrum critical energy.

Figures 5, 6 and 7 show three of the layouts for which the yields of photons have been computed. Figure 5 is the case of the SC magnets with a 30 mrad detector, the primary mask M1 at 8.3 m and M2 at 6.8 m. The aperture stop has a radius $x_a = 30$ mm at $z_a = \pm 1$ m. The mask M2 has been put as far away from IP as possible while still clearing the disrupted beam and shielding the lining M3 from direct soft bend photons.

Figure 6 shows the same final focus scheme and detector limits with different positions and radii for M2 and M3. M2 has been moved in to ± 2 m and has a radius of 5 mm. The aperture is now determined by soft bend SR and has a radius of 8 mm at $z = \pm 0.27$ m. Assuming a 5 mm minimum radial clearance to allow for beam steering, etc., Fig. 6 represents a "closest-in" configuration for the detector.

Figure 7 shows the MINIQAD scheme with M2 located at ± 3 m and radius 7.5 mm. The detector limits are 200 mrad. The aperture stop is at ± 5.3 cm and has a radius of 11 mm.

5. Rate of Soft Bend Photons in the Detector

The rate of soft bend photons reaching the detector via scattering or fluorescence on M2 and M3 has been calculated using Eq. (6) above with the data and results listed in Tables IV, V and VI. The first three columns contain the geometrical factors: the detector limits, the aperture stop [z_a (m), x_a (mm)], the mask [z (m), radius (mm)] and the angular interval of the SBSR intercepted by the mask ($\Delta\theta$). Contributions due to scattering or fluorescence off the bore or face of nearby quadrupoles, if any, have been listed separately. For the quadrupole bore, the distance z refers to its center. Columns four, five and six specify the radiation by type, critical energy and the number of photons/bunch striking the mask. For the configurations considered, the calculated rates due to edge effects are small and have not been included in the tables. The values of the two-bounce factors F_1 and F_2 evaluated at the critical energy K_c are listed in column seven. The solid angles subtended by the detector lining (column eight) are in the range 10^{-7} to 10^{-5} sr. The last column lists the number of photons entering the detector per bunch. These results will be discussed in Sect. VIII.

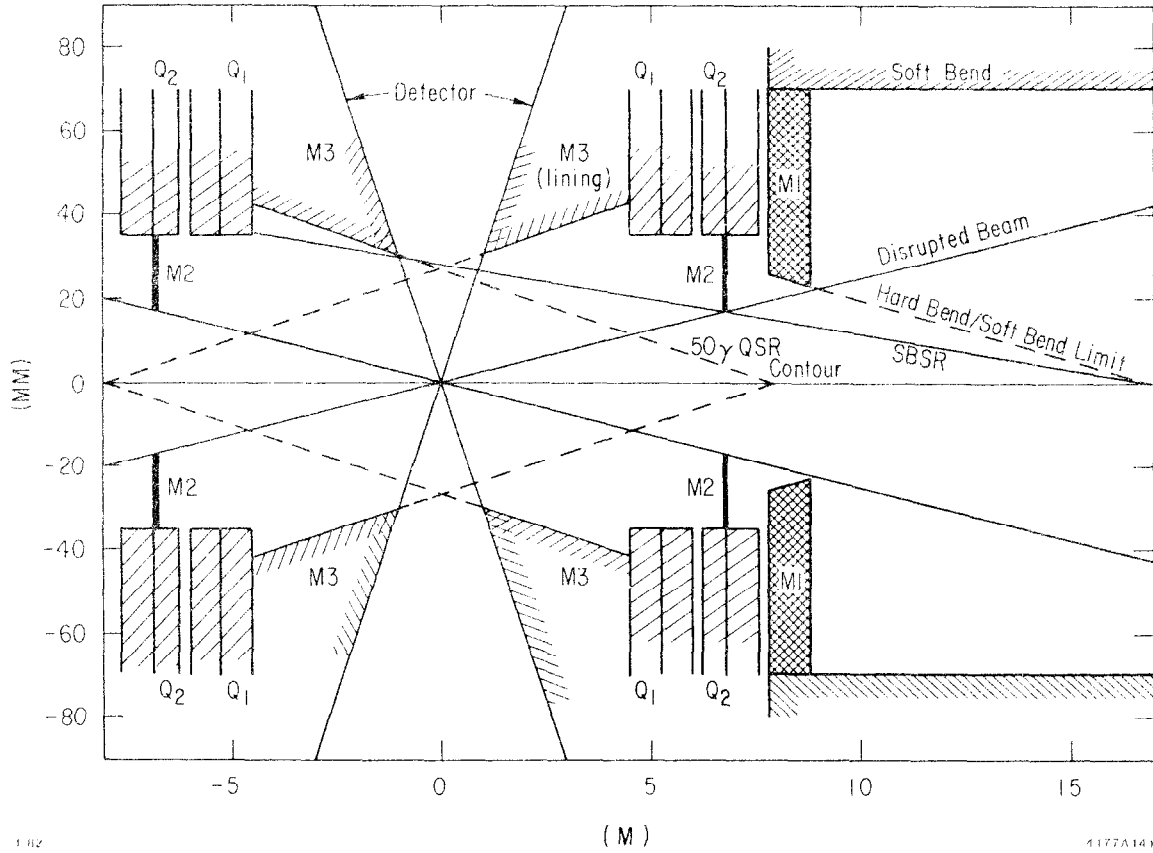


Fig. 5. Plan view of SLC interaction region for SC-QUADS optics, and mask M2 at the 6.8 m-position for a central detector with acceptance to within 30 mrad of the beam axis. Masks M1 and M2 are the primary and secondary synchrotron radiation masks respectively; mask M3 represents the lining (shielding) material of the central detector. Q1 and Q2 are the nearest quadrupoles to the IP.

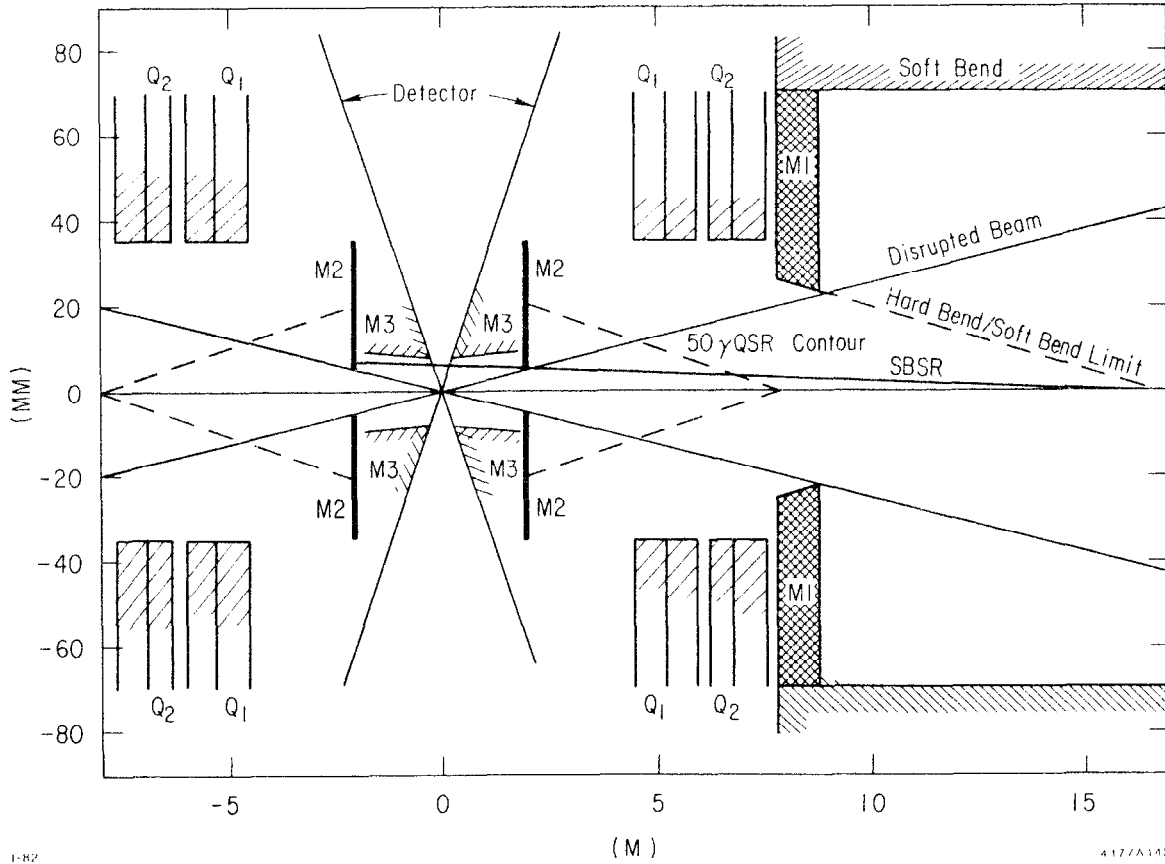


Fig. 6. Plan view of SLC interaction region for SC-QUADS optics, and mask M2 at the 2 m-position for a central detector with acceptance to within 30 mrad of the beam axis. Masks M1 and M2 are the primary and secondary synchrotron radiation masks, respectively; mask M3 represents the lining (shielding) material of the central detector. Q₁ and Q₂ are the nearest quadrupoles to the IP.

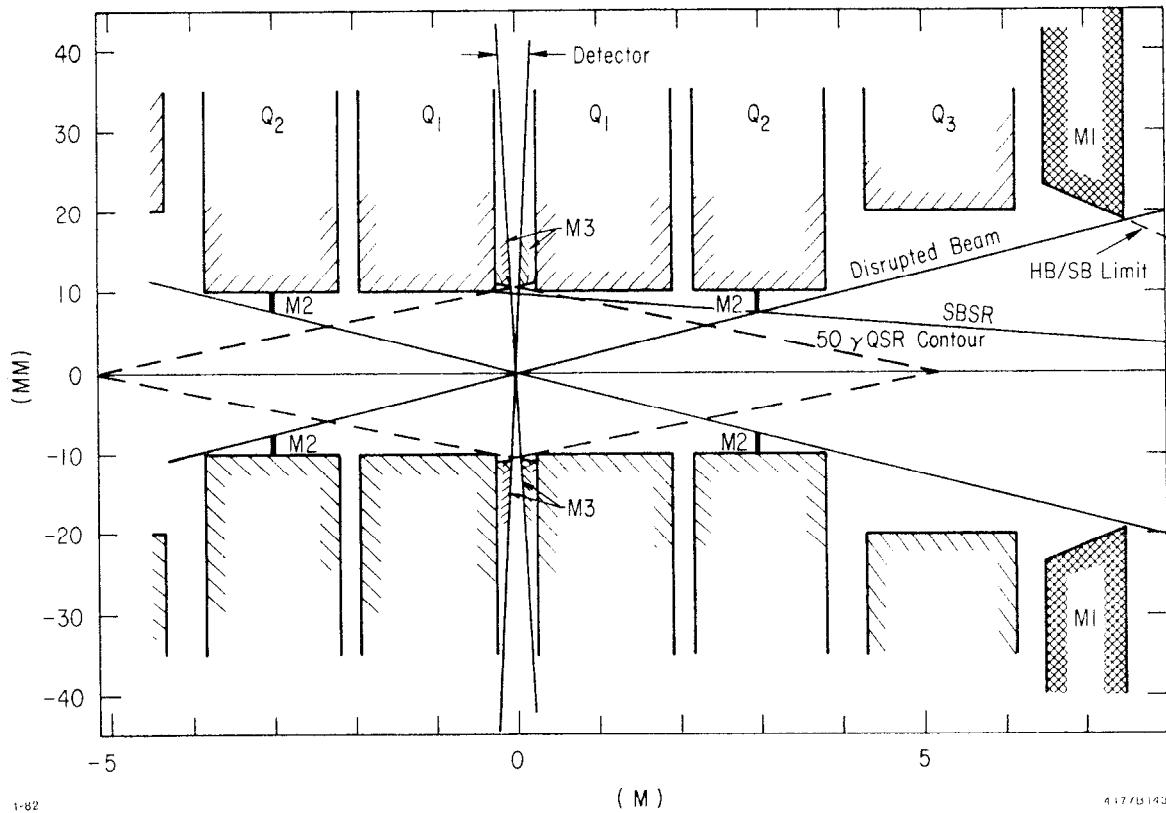


Fig. 7. Plan view of SLC interaction region for MQ-QUADS optics, and mask M2 at the 3 m-position for a central detector with acceptance to within 200 mrad of the beam axis. Masks M1 and M2 are the primary and secondary synchrotron radiation masks, respectively; mask M3 represents the lining (shielding) material of the central detector. Q₁, Q₂ and Q₃ are the nearest quadrupoles to the IP.

Table IV. SC-QUAD Optics: Photons/Bunch in 30 mrad Detector

Detector		Mask			Source of Photons	Critical / Median Energy KeV	γ / Bunch / Beam on Mask	Reflection / Fluorescence Factor F	$\Delta\Omega/2\pi$ Subt by Detector sr	γ / Crossing into Detector
θ Min MR	Aperture Stop M/MM	Type	Dist / Radius M/MM	$\Delta\theta$ from SB Center, MR						
30	1.0/30.	M2	6.85/17.1	0.77	SBSR/Ref1	$K_c = 44$	39.7×10^9	3.6×10^{-5}	5.9×10^{-6}	16.9
					SBSR/Fluor			4.0×10^{-4}		187.
		Qbore	5.675/35.	0.16	SBSR/Ref1		8.25×10^9	3.6×10^{-5}	10.5×10^{-6}	6.2
					SBSR/Fluor			4.0×10^{-4}		69.
		Qface	4.5/35.	0.07	SBSR/Ref1		3.6×10^9	3.6×10^{-5}	21.8×10^{-6}	5.7
					SBSR/Fluor			4.0×10^{-4}		63.
	M2	6.85/17.1	-	QSR/Ref1	$K_{1/2} = 80$	3.6×10^9	3.9×10^{-4}	5.9×10^{-6}	16.6	
				QSR/Fluor			3.3×10^{-3}		140.	
				DISR. Beam			$K = 500$		-	-
	0.27/8.	M2	2./5.	0.08	SBSR/Ref1	$K_c = 44$	4.1×10^9	3.6×10^{-5}	4.5×10^{-6}	1.3
					SBSR/Fluor			4.5×10^{-4}		16.6
				-	QSR/Ref1	$K_{1/2} = 60$	2.2×10^{10}	3.0×10^{-4}		59.4
QSR/Fluor					3.0×10^{-3}			594.		
0.08				DISR. Beam	$K = 500$	-	-	0.4×10^{-9}		3.8

Table V. SC-QUAD Optics: Photons/Bunch in 200 mrad Detector

θ Min MR	Detector		Mask		Source of Photons	Critical / Median Energy KeV	γ / Bunch / Beam on Mask	Reflec- tion / Fluores- cence Factor F	ΔΩ/2π Subt by Detector sr	γ / Crossing into Detector
	Aperture Stop M/MM	Type	Dist / Radius M/MM	Δθ from SB Cen- ter, MR						
200		M2	6.59 / 16.5	0.79	SBSR/Refl	K _C = 44	40.7 × 10 ⁹	3.6 × 10 ⁻⁵	0.7 × 10 ⁻⁶	2.2
				0.11	SBSR/Fluor			4.0 × 10 ⁻⁴		
	0.135/27.	Qbore	5.54/ 35.	-	SBSR/Refl	K _C = 44	5.7 × 10 ⁹	3.6 × 10 ⁻⁵	1.2 × 10 ⁻⁶	0.5
				-	SBSR/Fluor			4.0 × 10 ⁻⁴		
		M2	6.59/ 16.5	0.11	QSR/Refl	K _{1/2} = 86	3.9 × 10 ⁹	3.9 × 10 ⁻⁴	0.7 × 10 ⁻⁶	2.1
				-	QSR/Fluor			2.9 × 10 ⁻³		
				0.08	DISR. Beam	K = 500	-	-	2.3 × 10 ⁻⁹	22.9
				0.11						
	0.04/8.	M2	2./5.	0.08	SBSR/Refl	K _C = 44	4.1 × 10 ⁹	3.6 × 10 ⁻⁵	0.6 × 10 ⁻⁶	0.2
				-	SBSR/Fluor			4.0 × 10 ⁻⁴		
				-	QSR/Refl	K _{1/2} = 58	2.2 × 10 ¹⁰	3.0 × 10 ⁻⁴		8.0
				-	QSR/Fluor			3.0 × 10 ⁻³		
			0.08	DISR. Beam	K = 500	-	-	0.03 × 10 ⁻⁹	0.3	

Table VI. MQ-QUAD Optics: Photon/Bunch in 200 mrad Detector

Detector		Mask			Source of Photons	Critical / Median Energy KeV	γ / Bunch / Beam on Mask	Reflection Fluorescence Factor F	$\Delta\Omega/2\pi$ Subt by Detector sr	γ / Crossing into Detector			
θ Min MR	Aperture Stop M/MM	Type	Dist / Radius M/MM	$\Delta\theta$ from SB Center, MR									
200	0.053/10.6	M2	3.0/7.5	0.17	SBSR/Ref1	$K_c = 111$	8.8×10^9	1.3×10^{-4}	0.44×10^{-6}	1.0			
					SBSR/Fluor			1.4×10^{-3}		10.8			
		Qbore	1.625/10.	0.17	SBSR/Ref1		8.8×10^9	1.3×10^{-4}		2.8×10^{-6}	6.4		
					SBSR/Fluor			1.4×10^{-3}			69.0		
		M2	3.0/7.5	-	QSR/Ref1		$K_{1/2} = 34$	2.4×10^8		2.1×10^{-4}	0.44×10^{-6}	0.04	
					QSR/Fluor					2.5×10^{-3}		0.53	
				0.17	DISR. Beam	$K = 500$	-	-	0.2×10^{-9}	1.9			
	0.03/6.0	M2	2.0/5.0	-	0.145	SBSR/Ref1	$K_c = 111$	7.5×10^9	1.3×10^{-4}	0.27×10^{-6}	0.52		
						SBSR/Fluor			1.4×10^{-3}		5.6		
						QSR/Ref1			$K_{1/2} = 30$		1.7×10^9	1.9×10^{-4}	0.17
						QSR/Fluor						2.0×10^{-3}	1.84
					0.145	DISR. Beam			$K = 500$		-	-	0.04×10^{-9}

6. Quadrupole SR Due to the Primary Beam

In the SC scheme the quadrupole closest to the detector has a gradient of 107 T/m and a length of .75 m. A primary beam of 5×10^{10} electrons with a 1 s.d. spatial extent of 1 mm will then produce of order 7×10^9 photons with a critical energy of about 180 KeV. Similar numbers are obtained for the MQ scheme. Keil⁹ and Hofmann have pointed out that quadrupoles produce considerably more SR above the critical energy than bending magnets (see Appendix). For these reasons it is not clear that primary beam quadrupole synchrotron radiation can be neglected as a source of background in the detector.

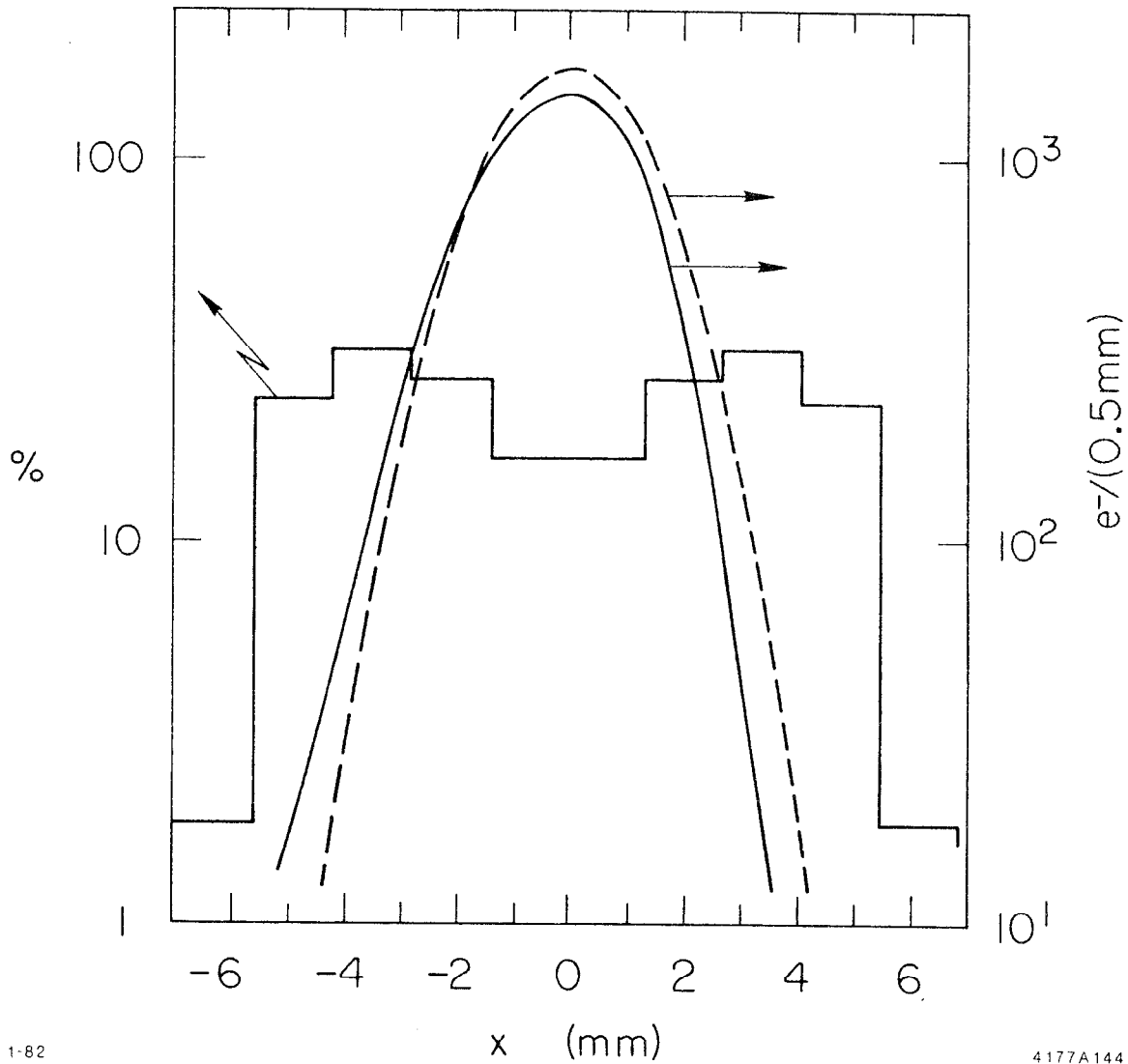
The QSR background has been computed using program SYNCHRO of A. R. Clark et al., for the two-quad SC configuration and the three-quad MQ configuration. The particles are traced towards the IP starting at the outboard side of Q_2 (SC) or Q_3 (MQ). At this point the distribution is assumed to be Gaussian in x and y with standard derivations taken from the final focus ray tracing programs.¹⁰ We have

	SC-QUADS	MQ-QUADS
σ_x	1.143 mm	1.376 mm
σ_y	2.592 mm	0.586 mm

As the quadrupole field increases with x and y, the tails of the particle distributions carry extra weight in producing photons. Figure 8 shows, as an example, the particle distribution at Q_3 of the MQ configuration and the Gaussian by which it has been approximated in calculating the QSR striking the inboard face of a mask at 3m. As shown in Fig. 8, ~17% of the photons striking this mask originate from a distance <1 s.d. in the distribution of Q_3 , while for $2 < x/\sigma_x < 3$ the fraction is 31% (for particles with $y/\sigma_y < 3$). The "real" distributions for $x/\sigma_x > 3$ contains 0.7% of the electrons, while for the Gaussian distribution the fraction is 0.3%. We estimate the uncertainty in the results on QSR due to the effects of tails to be about 50%.

With the input data as described, the yield of photons into the detector due to QSR was calculated with Eq. (6):

$$Y = \text{FLUX} * \text{F-FACTOR} * \text{SOLID ANGLE} , \quad (6)$$



1-82

4177A144

Fig. 8. Fraction of "Quadrupole" synchrotron photons striking the inside face of mask M2 vs the x coordinate of the radiating e^\pm at Quadrupole Q_3 (histogram). The solid and dashed curves are the "exact" e^\pm beam distribution at Q_3 and the Gaussian distribution used in the QSR background calculation, respectively.

where, as in the case of SBSR above, FLUX is the flux of photons striking M2, the F-factor is the probability for scattering or fluorescence, weighted by the QSR energy distribution [dn/dK in Eqs. (1), (3), (4) and (5)] and SOLID ANGLE is the solid angle subtended by the detector lining to the photons from M2.

The calculation of the first factor in Eq. (6), the flux of QSR photons produced, gives the following results:

- (a) In the layout of Fig. 5, 3.6×10^9 QSR photons hit the inboard face of M2, 3.0×10^6 photons hit the $Q_1 + \text{Sextupole} + Q_2$ bore and 1.8×10^4 photons hit the inboard face of Q_1 . No QSR photons reach the outboard face of M2. Moving M2 to $z = \pm 2M$ (Fig. 6), 1.0×10^{14} QSR photons hit the outboard face of M2, 2.2×10^{10} reach the inboard face at the opposite side of the IP.
- (b) In the layout of Fig. 7 the outboard side of M2 is struck by 3.7×10^4 QSR photons, the same-side Q-bore catches 2×10^3 photons, the face of Q_1 across the IP catches 1.1×10^4 photons, the quad bore across the IP catches 9.5×10^6 photons and the inboard face of M2 across the IP is struck by 2.4×10^8 photons. Moving M2 into 2m produces 4.7×10^7 photons on the outboard side of M2, 1.7×10^9 on the inboard side of M2 across the IP and negligible fluxes on the quads.
- (c) Calculating the fluxes at different z , we obtain contours of constant QSR flux. We position the detector lining along the 50 QSR photon/beam contour. The aperture stop is the intersection of the detector limits with this contour. The contours emerge from a virtual source point at $z = 8$ m for the SC-QUADS, $z = 5.25$ m for the MQ-QUADS. (See Figs. 5, 6 & 7.)

The F-factor in Eq. (6) is obtained in a way similar to that of the SBSR, the difference being in the calculation of the energy dependence dn/dK . While for SBSR the energy dependence is characterized by one parameter, the critical energy, the QSR energy distribution depends on the position and size of the mask and has no well-defined critical energy. We characterize it by $K_{1/2}$, the energy for which half the photons

have $K < K_{\frac{1}{2}}$. As seen in Tables IV, V and VI, $K_{\frac{1}{2}}$ depends on the position and aperture of the mask.

The resulting F-factor, listed in Tables IV, V and VI, shows that for the SC-QUADS, $F(\text{QSR})$ is about one order of magnitude larger than $F(\text{SBSR})$, while for the MQ-QUADS they are similar in magnitude. The QSR energy distributions are decreasing more slowly than the SBSR distribution when K is increased. This is evidenced by the fact that calculating F with an "equivalent" SBSR spectrum, setting $K_c = K_{\frac{1}{2}}$, results in F-factors that are a factor 3 to 5 (for SC-QUADS) or 10 to 14 (for MQ-QUADS) smaller than the ones in Tables IV, V and VI.

Multiplying the flux, the F-factor and the solid angle of the detector lining, we obtain the flux of QSR photons into the detector, listed in the last column of Tables IV, V and VI.

7. Backscattering from the Beamstrahlung Dump

The beamstrahlung produced when the two beams interact must eventually impact some object as it travels away from the interaction point. A small fraction of the secondaries produced from this impact will be directed back into the aperture within the detector and hence may scatter into the detector, itself. It should be noted that the disrupted beam itself is refocused and transported to a relatively distant beam dump, and thus is assumed not to pose a similar background problem for the detector. The synchrotron radiation produced by the disrupted beam as it exits through the quadrupoles near the IR presents a background problem similar in character to that of the beamstrahlung; however, the magnitude of this background is much smaller, so we will not discuss it further here.

The gammas emitted as beamstrahlung have an angular distribution which is roughly uniform in solid angle out to a maximum angle of 2.2 mrad, and strictly zero beyond that maximum angle. These photons are characterized by a maximum critical energy of 300 MeV. The total energy of the photons is 0.5×10^{-3} that of the incident beam;¹¹ thus the total photon energy for two 50 GeV beams of 5×10^{10} particles each is

$$E_{\gamma} = 2.5 \times 10^{12} \text{ MeV}$$

Where will the beamstrahlung impact? The half-cone angle (2.2 mrad) of the beamstrahlung is sufficiently small that it should be possible to design the beam line such that it will not impact until after traversing the low and high field bend magnets. It seems unavoidable, however, to prevent most or all of this radiation from impacting in the vicinity of the yoke of the quadrupole which is outboard of the high field bend magnet (at a distance of approximately 30 m from the IP). At this distance the radius of the disk of beamstrahlung radiation has grown to 66 mm. We assume that all of the beamstrahlung will be dumped here.

We have investigated, using the EGS program, the characteristics of particles which emerge from the surface when a gamma ray strikes a semi-infinite block of material at normal incidence. Runs were made using Pb and Al as the material for incident gamma energies of 10, 50 and 200 MeV. The angles and energies of particles which emerge from the incident surface were tabulated. The particles which emerge are dominated by photons of energy 0.5 MeV which have been produced by the annihilation of positrons. The rates of interest vary over a range of about a factor of three among the cases investigated. We characterize these results as follows:

$$f_{BS} = 0.02 \text{ photons}/2\pi * \text{steradian}/\text{incident MeV} .$$

Thus for the beamstrahlung intensity noted above, we expect

$$N_Y (\text{back scatter}) = 5.0 \times 10^{10} \text{ photons}/2\pi \text{ steradian} .$$

Note that this rate is intended to be correct only in the backward direction; it would be incorrect (an overestimate) to use it to calculate the total number of photons which emerge from the dump.

The sensitive solid angle of the detector is that defined by the two circular apertures as described above. These apertures are viewed from a source which is a uniform disk of radius 66 mm at a distance of 30 m. (We neglect, for the moment, the partial shadowing of these apertures by the mask described above.) For a source point on axis it is easy to calculate this solid angle directly as the difference in solid angle of the two apertures as viewed from the source. For source points on the disk with radii larger than the aperture radius the calculation

is more complicated. An approximation, which estimates this solid angle based on the area of two nonconcentric circles of equal radius, gives results that are in error by as much as a factor of two for the present case.

Using a better approximation than that described above, we have calculated the solid angle of the aperture (for various configurations) averaged over source positions uniformly distributed over a disk of radius 66 mm at a distance of 30 m. The results are summarized in Table VII. If a circular mask (as described previously) is present in these configurations, the aperture will be partially shadowed by this mask. The reduced effective solid angle of the aperture because of the presence of the mask has been estimated and is also included in Table VII. As a point of reference, the solid angle of the aperture as viewed from a point on-axis at 30 m is also tabulated. Note that all solid angles are given not in steradians, but as a fraction of 2π steradians.

These gammas which enter the aperture must scatter there if they are to enter the detector. The fraction of these 0.5 MeV gammas which will so scatter has been evaluated using the EGS program and is

$$f_{\text{graze}} = 0.19$$

We are now in a position to estimate the number of photons which will enter the detector as a consequence of dumping the beamstrahlung at 30 meters. It is

$$N_{\gamma}(\text{detector}) = E_{\gamma} \cdot f_{\text{BS}} \cdot \frac{\text{SA}}{2\pi} \cdot f_{\text{graze}}$$

The pertinent solid angles for various mask and aperture combinations are listed in Table VII, and the corresponding number of photons reaching the detector in Tables IV, V and VI.

8. Conclusion: Normal or S-Bend IR?

The yields of photons into an SLC detector resulting from soft bend SR, quadrupole SR and disrupted beam radiation (DBR) via reflection, scattering and fluorescence off a mask and off the detector lining,

Table VII. Solid Angle of Aperture Viewed from Beamstrahlung Dump at 30 m.

Final Focus	θ_{\min} mrad	Aperture Stop m/mm	Mask M2 m/mm	(Solid Angle of Aperture)/ 2π ($\times 10^9$)		
				As Viewed from Axis	Average Over Beamstrahlung Disk	Average Over Disk, Shadowed By Mask
SC	30	1.00/30.	6.85/17.1	67.	74.	16.
		0.267/8.	2.00/5.0	1.3	2.9	0.4
	200	0.135/27.	6.59/16.5	7.3	8.6	2.3
		0.040/8.	2.00/5.0	0.2	0.3	0.03
MQ	200	0.053/10.6	3.0/7.5	0.4	0.6	0.2
		0.030/6.0	2.0/5.0	0.1	0.1	0.04

calculated for the six configurations of equipment (SC/MQ, 30/200 MR, MASK FAR/NEAR) considered have been summarized in Table VIIIa, first column. The following features are then apparent:

- (a) The number of photons entering the detector per bunch ranges from ~10 to ~700 depending on the configuration.
- (b) Moving the mask from the "far" to the "near" position decreases the contribution of the SBSR photons, due to the better shadowing of the opposite side by the same-side mask in the "near," small aperture position. At the same time the QSR contribution increases due to the steep increase in the number of QSR photons at small distance from the beam. The DBR contribution decreases since the solid angle for DBR is reduced in the "near" position. The net result is that for the SC-QUADS the total yield of the photons is not strongly affected by the position of the mask. For the MQ-QUADS the effect of moving the mask is obscured by the fact that in the "far" position 85% of the SBSR photons in the detector do not originate from the mask but from the quad-bore.
- (c) The number of background photons in a detector with a minimum opening angle of 200 mrad around the beam is at least a factor eight less than the corresponding number for a detector which extends down to 30 mrad.

One may wonder to what extent the number of photons could be reduced, if not by moving the mask, by making use of the fact that one of the components of the background, the SBSR, is not azimuthally symmetric, but is tangential to the direction of the incident beams and confined to a very small angle with respect to the horizontal plane.

The effect of azimuthally limiting the mask is shown in Table VIIIa, columns two and three. In column two the mask has been cut in half, leaving only the sides which stop the incident SBSR. For the three configurations with the masks in the "far" position the SBSR is obviously not changed, the QSR is reduced by a factor of two, and the disrupted beam backscattered radiation (DBR) is increased since the detector lining is now only partly shadowed by the mask and hence the solid angle

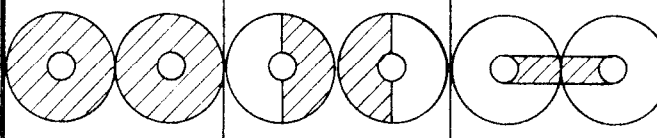
is increased (in the ratio $d\Omega_1 + d\Omega_2/2 d\Omega_2$, where $d\Omega_{1,2}$ are the solid angles of the two last columns in Table VII). The net result is a < 20% increase in the background.

For the three configurations with the mask in the "near" position, the mask can not be cut azimuthally without the penalty of directly irradiating part of the detector lining with QSR. A fraction of this radiation would reach the detector in a single scatter and hence the background would be greatly increased. For these three configurations, we have therefore pushed the detector lining out to the position it had in the corresponding "M2 far" position (e.g., M2 as in Fig. 6, with M3 as in Fig. 5). The attendant increase in solid angle results in a significant increase in background due to SBSR and QSR. The DBR component is also increased: at the shielded side of the M2 no DBR photon can reach the pushed-out detector lining, but at the exposed side the rate is increased due to the larger solid angle subtended by this lining. The backgrounds for the "M2 near" are indicated in Table VIII. For example, for the SC-QUADS/30 MR DETECTOR configuration, about 31K photons would enter the detector per crossing.

Table VIIIa, column three shows the effect of removing most of the mask, leaving only a rod in the horizontal plane, with a height determined by the beam divergence in the soft bend. Here again the lining has been pushed outwards for the "M2 near" cases in order to prevent single bounce photons from entering the detector. The rod has been assumed to absorb all SBSR and none of the QSR. The rates are increased, with respect to the full mask cases, by factors varying from one to five. For a detector with 200 mrad minimum angle there appears to be little sensitivity to the replacement of a full-azimuth mask by a thin rod.

A different way of using the azimuthal asymmetry of the SBSR to affect the background is to exploit the possibility of an "S-bend" IR, in which the incident beams follow trajectories which are part of two circles of equal radius R tangent at the IP and with a distance between the centers equal to 2R. In an S-bend IR the mask will stop all of the same-side SBSR that would otherwise hit the detector lining without being an obstacle to the SBSR from the other beam.

Table VIII. Background photons per crossing are recorded for various arrangements of magnets, detectors and masks for 5×10^{10} , 50 GeV particles per beam. The backgrounds are summarized for: (1) 30 mrad and 200 mrad minimum detector angular acceptance; (2) SC and MQ quad optics; (3) two positions for the secondary mask, M2; and (4) three mask azimuthal geometries. Part (a) is for the "normal" geometry, and part (b) is for the "S-bend" geometry for the final focus bends. The figure at the top of this table refers to mask M2 looking out from IP. In the boxes marked "A" the detector lining has been pushed out to the position in the corresponding "MASK FAR" configuration.

(a)				
		Normal IR		
SC-QUADS 30 MR DET MASK FAR	SBSR QSR DBR	348 157 <u>152</u>	348 78 <u>428</u>	348 0 <u>703</u>
	TOTAL	657	854	1051
SC-QUADS 30 MR DET MASK NEAR	SBSR QSR DBR	18 653 <u>4</u>	1600 29100 <u>352</u>	1600 0 <u>703</u>
	TOTAL	675	31052 A	2303 A
SC-QUADS 200 MR DET MASK FAR	SBSR QSR DBR	31 18 <u>22</u>	31 9 <u>52</u>	31 0 <u>82</u>
	TOTAL	71	92	113
SC-QUADS 200 MR DET MASK NEAR	SBSR QSR DBR	2 88 <u>0</u>	80 1760 <u>41</u>	80 0 <u>82</u>
	TOTAL	90	1881 A	162 A
MQ-QUADS 200 MR DET MASK FAR	SBSR QSR DBR	87 1 <u>2</u>	87 0 <u>4</u>	87 0 <u>6</u>
	TOTAL	90	91	93
MQ-QUADS 200 MR DET MASK NEAR	SBSR QSR DBR	6 2 <u>0</u>	34 6 <u>3</u>	34 0 <u>6</u>
	TOTAL	8	43 A	40 A

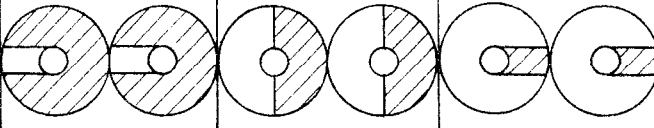
(b)				
		S-Bend IR		
SC-QUADS 30 MR DET MASK FAR	SBSR	144	144	144
	QSR	157	78	0
	DBR	<u>152</u>	<u>428</u>	<u>703</u>
	TOTAL	453	650	847
SC-QUADS 30 MR DET MASK NEAR	SBSR	0	0	0
	QSR	653	29100	0
	DBR	<u>4</u>	<u>352</u>	<u>703</u>
	TOTAL	657	29452 A	703 A
SC-QUADS 200 MR DET MASK FAR	SBSR	6	6	6
	QSR	18	9	0
	DBR	<u>22</u>	<u>52</u>	<u>82</u>
	TOTAL	46	67	88
SC-QUADS 200 MR DET MASK NEAR	SBSR	0	0	0
	QSR	88	1760	0
	DBR	<u>0</u>	<u>41</u>	<u>82</u>
	TOTAL	88	1801 A	82 A
MQ-QUADS 200 MR DET MASK FAR	SBSR	75	75	75
	QSR	1	0	0
	DBR	<u>2</u>	<u>4</u>	<u>6</u>
	TOTAL	78	79	81
MQ-QUADS 200 MR DET MASK NEAR	SBSR	0	0	0
	QSR	2	6	0
	DBR	<u>0</u>	<u>3</u>	<u>6</u>
	TOTAL	2	9 A	6 A

Table VIIIb, columns one to three show the effect of an S-bend IR with different masks. Comparing a given configuration and a given type of mask with and without an S-bend, it appears that an S-bend reduces the background in all configurations, in most cases by a factor less than two. The azimuthally symmetric part of the SBSR (from the quad-face and bore), the QSR and the DER and not affected by the choice S-bend versus normal IR. Since these sources dominate, there is no significant improvement in the S-bend arrangement of the IR.

In conclusion, lining the detector with a thin layer of Pb, choosing the minimum detector angle not less than 200 mrad, and making a judicious choice of position and azimuthal profile of the masks (keeping their aperture clear of the disrupted beams) will result in manageable levels of background photons in an SLC detector, without the need to resort to an S-bend IR.

With minor additional work the results reported in this note can be used to define SR-stay-clear limits and to provide guidance to an engineering design of the vacuum chamber and the masks for the SLC interaction region, once the choice between miniquads and super-conducting quads has been made.

References

1. D. Koltick, SLC Workshop Note 49.
2. W. G. Langeveld, SLC "IR Group" Minutes, June 25, 1981.
3. R. Larsen, Note April 23, 1980.
4. R. Larsen, Note January 29, 1980.
5. E. Storm and H. I. Israel, Nuclear Data Tables A7, 565 (1970).
6. E. Fermi, Course on Nuclear Physics, (University of Chicago Press, 1951).
7. M. Stobbe, Ann d. Phys. 7, 661 (1930).
8. This QSR stay-clear limit lies outside the limit due to the maximum angle soft bend SR admitted by the masks. Preliminary results were based on the SBSR limit only.
9. E. Keil, CERN/ISR-LTD/76-23.
10. Programs, TRANSPORT and TURTLE (courtesy K. L. Brown and F. Bulos).
11. J. Jaros, AATF/80/22, May 7, 1980 and May 20, 1980.
12. R. A. Mack, CEAL-1027 (1966).
13. H. DeStaebler, SLAC/Group A Eng. Note 60-R1.
14. A. R. Clark, Photon-Induced Fluorescence from Tantalum, May 2, 1977.

APPENDIX A

1. The Synchrotron Radiation Distribution Function

Critical energy $K_c = \frac{276.8}{\rho(\text{m})}$ MeV at 50 GeV, ρ = bending radius

$$x = K/K_c$$

$$\frac{dn}{dK} = \frac{P_\gamma}{K_c^2} \frac{1}{K/K_c} S(K/K_c) \quad , \quad n_T = \int \frac{dn}{dK} dK = \frac{15\sqrt{3}}{8} \frac{P_\gamma}{K_c}$$

$$\frac{1}{n_T} \frac{dn}{dK} = \frac{8}{15\sqrt{3}} \frac{1}{x} S(x) dx \quad , \quad \int_0^\infty S(x) dx = 1$$

$$S(x) = \frac{9\sqrt{3}}{8\pi} x \int_x^\infty K_{5/3}(s) ds$$

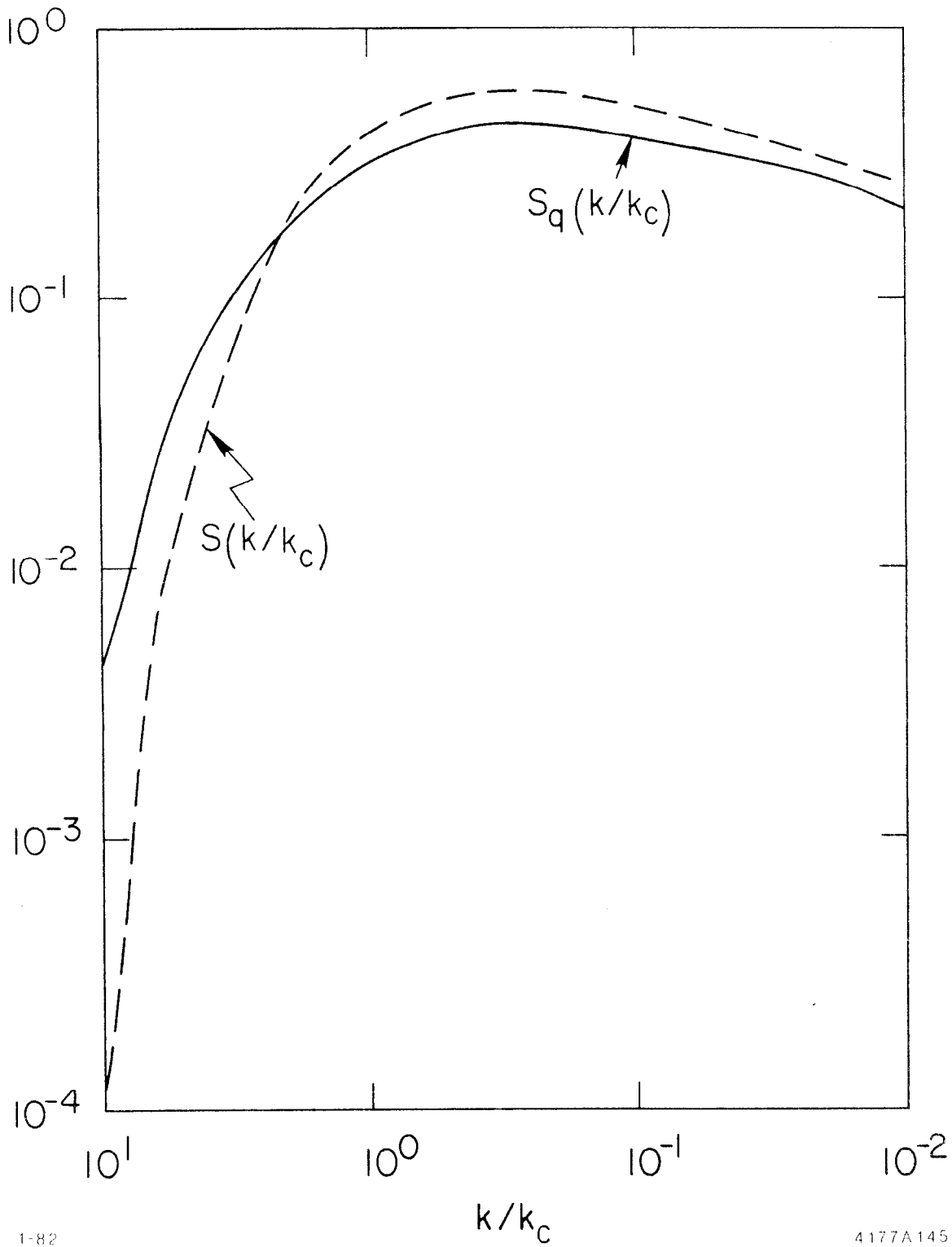
$$P_\gamma = \frac{c C_\gamma E^4}{2\pi\rho^2} \text{ GeV/sec} \quad , \quad C_\gamma = 8.85 \times 10^{-5} \text{ m/GeV}^3$$

The distribution function has been evaluated by (a) interpolating data by R. A. Mack¹² and (b) using approximate formulae by H. DeStaebler.¹³ There is good agreement in the range 10-100 keV.

The formulae above apply to SR generation in dipole magnets. As pointed out in Ref. 9, they can be used for quadrupole magnets by computing P_γ with a bending radius evaluated at a distance from the quadrupole axis equal to 1 standard deviation (σ) of the Gaussian distribution of particles in the beam and by substituting $S(x)$ with

$$S_q(x) = \frac{9\sqrt{3}}{8} x \int_0^\infty K_{5/3}(s) [1 - \text{erf}(x/s\sqrt{2})] ds$$

A plot of (Fig. A-1, taken from Ref. 9) $S(x)$ and $S_q(x)$ vs x shows that for quadrupole magnets there is more SR above $x=1$ than for bending magnets. At $x=10$ the ratio is ≈ 50 .



1-82

4177A145

Fig. A-1. Comparison of the synchrotron power spectra appropriate for bend magnets, $S(K/K_c)$, and for quadrupole magnets, $S_q(K/K_c)$.

2. Reflection

The fraction of photons scattering in a semi-infinite medium through an angle θ_s into the backward hemisphere is given by (see Ref. 4)

$$f(K, \theta_s) = \int_0^{\infty} e^{-\mu_a x} e^{-\mu_a x / \cos \theta_s} \mu_s(\theta_s) dx \quad .$$

After integration and averaging over angles, assuming isotropy, we have

$$f(K, \theta_s) = \frac{\mu_s(\theta_s)}{\mu_a [1 + (1/\cos \theta_s)]} \quad ; \quad f(K) = \frac{\int_0^1 f(K, \theta_s) d\cos \theta_s}{\int_{-1}^{+1} d\cos \theta_s} = 0.15 \frac{\mu_s}{\mu_a} (K)$$

The mass scattering (μ_s) and absorption (μ_a) coefficients have been taken from Table III (Ref. 5). Scattering into the backward hemisphere is Compton scattering and non-isotropic. The fraction of Compton scattering and the degree of anisotropy is energy dependent. For photon energies in the range $10 < K < 100$ keV the net anisotropy is $< 10\%$. Part of the Compton scattering is forward, with e^- going backwards, with negligibly small energy. The backward photon energy K' is given by

$$\frac{K'}{m_e} = \frac{\alpha}{1 + 2\alpha} \quad ; \quad \alpha = \frac{K}{m_e} \quad ; \quad m_e = \text{electron mass} \quad .$$

The fraction of soft bend SR reflected on M2 is

$$F = \frac{0.15}{n_T} \int_0^{\infty} \frac{\mu_s}{\mu_a} (K) \frac{dn}{dK} dK$$

and the fraction scattering off M2 and M3 is

$$F_1 = \frac{0.15}{n_T} \int_0^{\infty} \left(\frac{\mu_s}{\mu_a} (K) \right)_{\text{INCOH}} \left(\frac{\mu_s}{\mu_a} (K') \right)_{\text{COH}} \frac{dn}{dK} dK \quad . \quad (\text{A.1})$$

The mass scattering coefficients μ_s of Table III have been evaluated for free electrons. The effect of binding on the value of F_1 is energy dependent and less than ~20% for $K > 20$ keV.

3. Fluorescence

The fraction of photons absorbed in a mask with subsequent emission of a fluorescent photon through an angle θ_s is given by:

$$f(K, \theta_s) = \int_{K_{\min}}^{\infty} e^{-\mu_a(K)x} e^{-\mu_a(K_\alpha)x/\cos\theta_s} \mu'_a dx$$

$\mu'_a = \mu_a(K)G$ with G = probability for the absorption in the K-shell followed by emission of a photon with energy equal to the difference of the K-shell and L-shell binding energy in the material of the mask. The K and L shell electrons are bound⁶ with an energy $\approx Ry (Z-1)^2$ and $Ry (Z-5)^2/4$. For Pb $K_\alpha = 72$ keV. The factor G is <1 due to the contribution of radiation-less absorption (Auger electrons) and absorption in other than K-shells. The threshold energy $K_{\min} = 88$ keV for Pb. Averaging over angles we have

$$f(K) = \frac{G}{2} \left[1 + r \ln \frac{r}{1+r} \right] ; \quad r = \frac{\mu_a(K_\alpha)}{\mu_a(K)} .$$

The fluorescence factor for M2 weighted by the SR distribution is

$$F = \frac{G}{2n_T} \int_{K_{\min}}^{\infty} \left[1 + r \ln \frac{r}{1+r} \right] \frac{dn}{dK} dK .$$

For the two-bounce case, fluorescence on M2 and coherent scattering on M3, we have

$$F_2 = \frac{G}{2n_T} \int_{K_{\min}}^{\infty} \left(\frac{\mu_s}{\mu_a} (K_\alpha) \right)_{\text{COH}} \left[1 + r \ln \frac{r}{1+r} \right] \frac{dn}{dK} dK . \quad (\text{A.2})$$

An upper limit for G can be obtained from the probability for K-shell

absorption of photons with energy equal to the K-shell binding energy. In Ref. 5, this upper limit is estimated to be 0.767 at the K-edge for $A=92$, weakly dependent on energy (0.82 at 1000 keV). Reference 14 quotes a value $G=0.757$ for Tantalum. We have used the latter value for Pb.

For the calculation of r the values of Table III (Ref. 5) have been used. The table was cross-checked by calculating the mass absorption coefficient near the K-edge with the formula of Stobbe:⁷

$$\frac{\sigma_K}{\sigma_{\text{THOMSON}}} = 128\pi \frac{137^3}{Z^2} \left(\frac{K_{\text{min}}}{K}\right)^4 \frac{e^{-4\xi \operatorname{arccot} \xi}}{1 - e^{-2\pi\xi}}$$

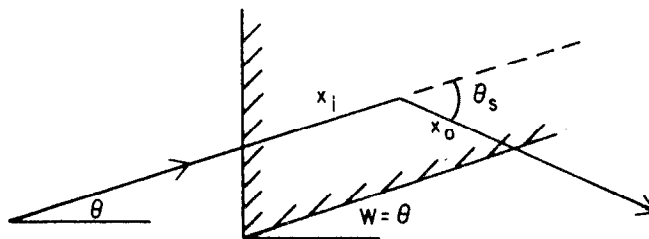
with $\xi = \sqrt{K_{\text{min}}/K - K_{\text{min}}}$. For Pb $\mu(K_\alpha) = N_{\text{AV}}\sigma_K/A = 5.6 \text{ cm}^2/\text{g}$, in reasonable agreement with Ref. 5. For $K_\alpha = K$, F_2 reduces to the form of F_1 .

4. Edge Scattering

Consider a mask M2 of which the inner edge is tapered to follow the average direction of the photons from the soft bend. For a photon incident with angle θ equal to the wedge angle w , at a distance y from the tip of the edge, the probability for coherent scattering through an angle θ_s is given by

$$f(y) = \int e^{-\mu_a x_i} \mu_s e^{-\mu_a x_o} dx_i$$

$$= \frac{\mu_s}{\mu_a} e^{-\mu_a y/\theta_s}$$



Integration over the impact distance y gives

$$f(K) = \frac{\mu_s}{\mu_a} \frac{\theta_s}{\mu_a}$$

The dimension of "f" is g/cm^2 . In order to obtain the yield of photons

"f" is multiplied by the rate of incident photons per g/cm^2 along the y-direction. For edge scattering off M2 we thus obtain for the SR distribution:

$$F = \frac{1}{n_T} \int \frac{\mu_s}{\mu_a} \frac{\theta_s}{\mu_a} \frac{1}{\rho \Delta z} \frac{dn}{dK} dK$$

where $1/\rho \Delta z$ is the number of radians per g/cm^2 of mask. Δz is the distance between the source (center of soft bend) and the mask, and ρ is the density of the mask material. For edge scattering off M2, followed by coherent scattering off M3, we have

$$F_3 = \frac{1}{n_T} \int \left(\frac{\mu_s}{\mu_a} (K) \right)_{\text{COH}}^2 \frac{\theta_s}{\mu_a} \frac{1}{\rho \Delta z} \frac{dn}{dK} dK \quad . \quad (\text{A.3})$$

5. Edge Fluorescence

In analogy with edge scattering we have

$$f(y) = \int e^{-\mu_a(K)x_i} \mu'_a e^{-\mu_a(K_\alpha)x_o} dx_i = \frac{\mu'_a}{\mu_a(K)} e^{-\mu_a(K_\alpha)y/\theta_s}$$

and

$$f = \frac{\mu'_a}{\mu_a} \frac{\theta_s}{\mu_a(K_\alpha)}$$

where μ'_a is the mass absorption coefficient at the fluorescent photon energy $K = K_\alpha$. For fluorescence on M2 we have:

$$\begin{aligned} F &= \frac{1}{n_T} \int_{K_{\min}}^{\infty} \frac{\mu'_a}{\mu_a} \frac{\theta_s}{\mu_a(K_\alpha)} \frac{1}{\rho \Delta z} \frac{dn}{dK} dK \\ &= \frac{1}{n_T} G \frac{\theta_s}{\mu_a(K_\alpha)} \frac{1}{\rho \Delta z} \int_{K_{\min}}^{\infty} \frac{dn}{dK} dK \quad . \end{aligned}$$

For fluorescence on M2 followed by coherent scattering off M3 we have:

$$\begin{aligned} F_4 &= \frac{1}{n_T} \left(\frac{\mu_s}{\mu_a} (K_\alpha) \right) \int_{K_{\min}}^{\infty} \frac{\mu'_a}{\mu_a} \frac{\theta_s}{\mu_a(K_\alpha)} \frac{1}{\rho \Delta z} \frac{dn}{dK} dK \\ &= \frac{1}{n_T} \left(\frac{\mu_s}{\mu_a} (K_\alpha) \right)_{\text{COH}} G \frac{\theta_s}{\mu_a(K_\alpha)} \frac{1}{\rho \Delta z} \int_{K_{\min}}^{\infty} \frac{dn}{dK} dK \end{aligned} \quad (\text{A.4})$$

The dependence of F_1 to F_4 on the critical energy is shown in Figs. 1-4.

C. Photons and Electrons from Beam-Gas Bremsstrahlung:

The energy loss for highly relativistic electrons in passing through matter is dominated by bremsstrahlung. A Monte Carlo program has been written which generates events according to the differential bremsstrahlung cross section.^{1,2} Figure 1 is a sample output which shows how strongly peaked the cross section is toward small angles. There is a dependence of the angular distribution with the photon energy, but as can be seen the main part of the cross section at even large photon energies is contained within 10 microradians.

The root mean square angle for both the emitted photon and scattered electron is:

$$\langle \theta^2 \rangle^{1/2} \sim \frac{m_e}{E} = \frac{1}{\gamma} .$$

At SLC beam energies this is 10 microradians. The order of magnitude of the radiation emitted in the backwards direction is:

$$\frac{\sigma_{\text{back}}}{\sigma_{\text{forward}}} \sim \frac{1}{\gamma^4} \sim 10^{-20} \text{ at SLC} .$$

For all practical purposes at the SLC we can assume that the bremsstrahlung photon and electron continue to move along the initial direction of the incoming electron. This means we can eliminate the bremsstrahlung photons in the straight sections near the interaction region as a source of background. They will move through the interaction region along a straight trajectory and interact in the beam pipe downstream of the detector.

The degraded energy electrons are a possible source of background. The bremsstrahlung electrons produced in the region between the first bend and the quadrupole just before the interaction region can be over focused into the detector because of their lower energy. To check how many electrons might be overfocused we look at the radiation cross section.³ Evaluating the cross section using nitrogen as the target:

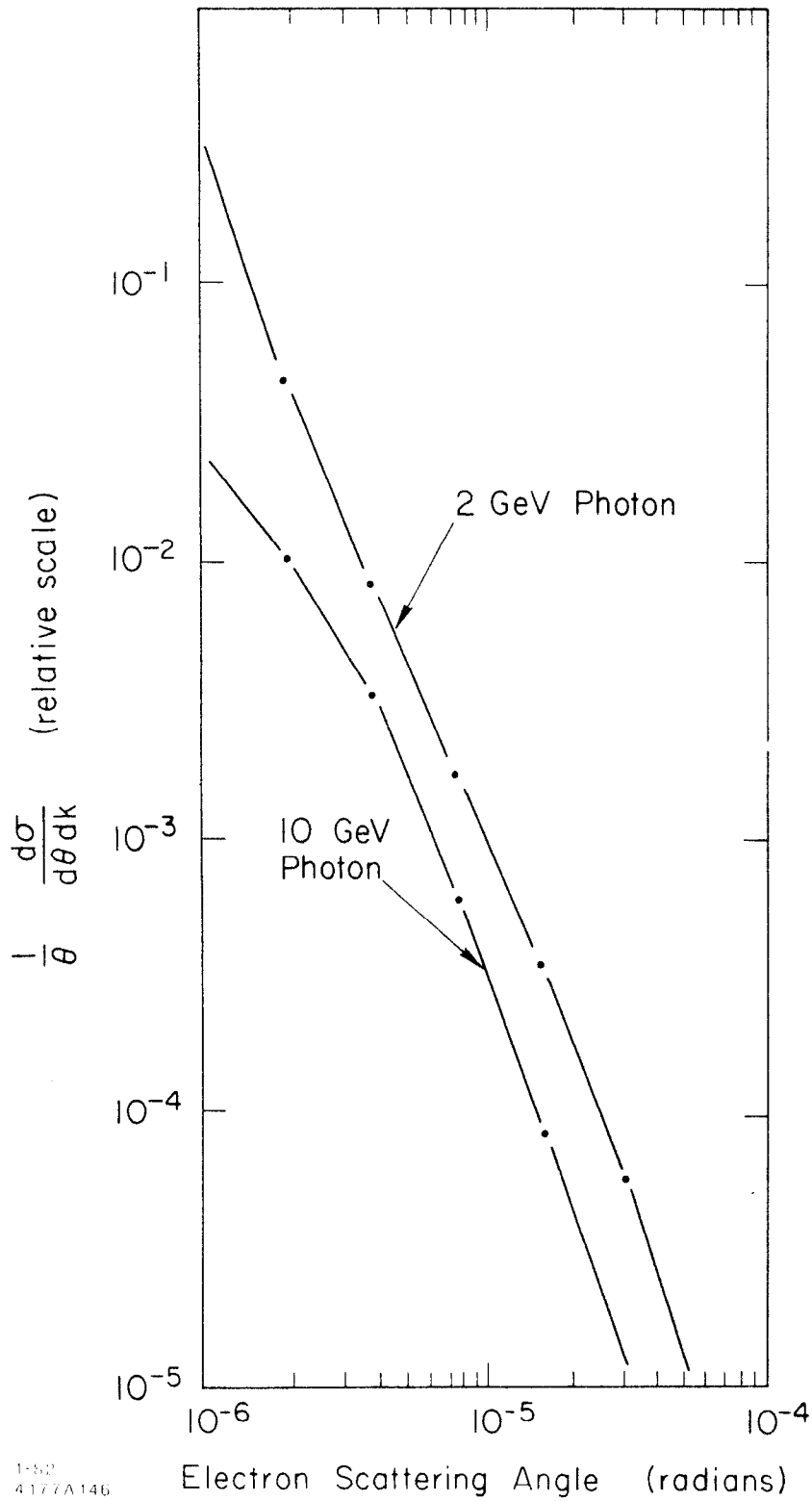


Fig. 1. The differential bremsstrahlung cross section for an electron to be scattered at an angle, θ , accompanied by a photon emitted at any angle but with a given energy.

$$\sigma_{\text{total}} = 7.3 \times 10^{-25} \text{ cm}^2 \int_{K_{\text{min}}}^{K_{\text{max}}} \frac{dK}{K} = 7.3 \times 10^{-25} \text{ cm}^2 \ln \left[\frac{K_{\text{max}}}{K_{\text{min}}} \right]$$

For K_{max} we will use the full electron energy. For K_{min} we use the smallest electron energy loss which will just pass through the final focus. The SLC design energy spread is $\frac{1}{2}\%$, so $K_{\text{min}} = 250$ MeV. The exact value one uses for K_{min} is not very important because the total cross section has only a logarithmic dependence on K_{min} .

The resulting number of bremsstrahlung electrons per crossing due to both the electron and positron beam at the SLC can be written

$$N_{\text{brem}} = P(\text{nanotorr}) \times N_{\text{per-beam}} (10^{10}) \times L(\text{cm}) \times Z^2 \times 10^{-7}$$

using the values of 5 nanotorr for the pressure, 5×10^{10} particles per beam, a distance between the first bend and the first quadrupole of 1700 cm and nitrogen as the gas, the number of bremsstrahlung electrons due to both beams is

$$N_{\text{brem}} \sim .2 \text{ per crossing} \quad .$$

This number is reasonable small when compared to a PEP value of five per crossing. But the SLC will be much stronger focusing than PEP. This will cause a larger portion of the bremsstrahlung electrons to be over focused into the detector as compared to PEP.

To keep the number of bremsstrahlung events low, the SLC should hold to its design pressure of a few nanotorr.

References

1. D. Koltick, SLC Workshop Note 49.
2. H. Bethe and W. Heitler, Proc. Royal Soc. 146A, 83 (1934).
3. J. D. Jackson, Classical Electrodynamics, Wiley, New York, N.Y.

D. Large Angle Synchrotron Radiation

Synchrotron radiation by a high energy electron is highly collimated in the electron's direction. Expressions for frequency and angular distributions of this radiation are typically obtained through approximations which exploit this collimation. While this approach describes the main features of synchrotron radiation, background effects from the tails of the synchrotron radiation distribution may not be well-known. In particular, with the large numbers of particles per bunch in the SLC, the question arises as to whether there is a few percent probability of energetic synchrotron radiation at large angles.

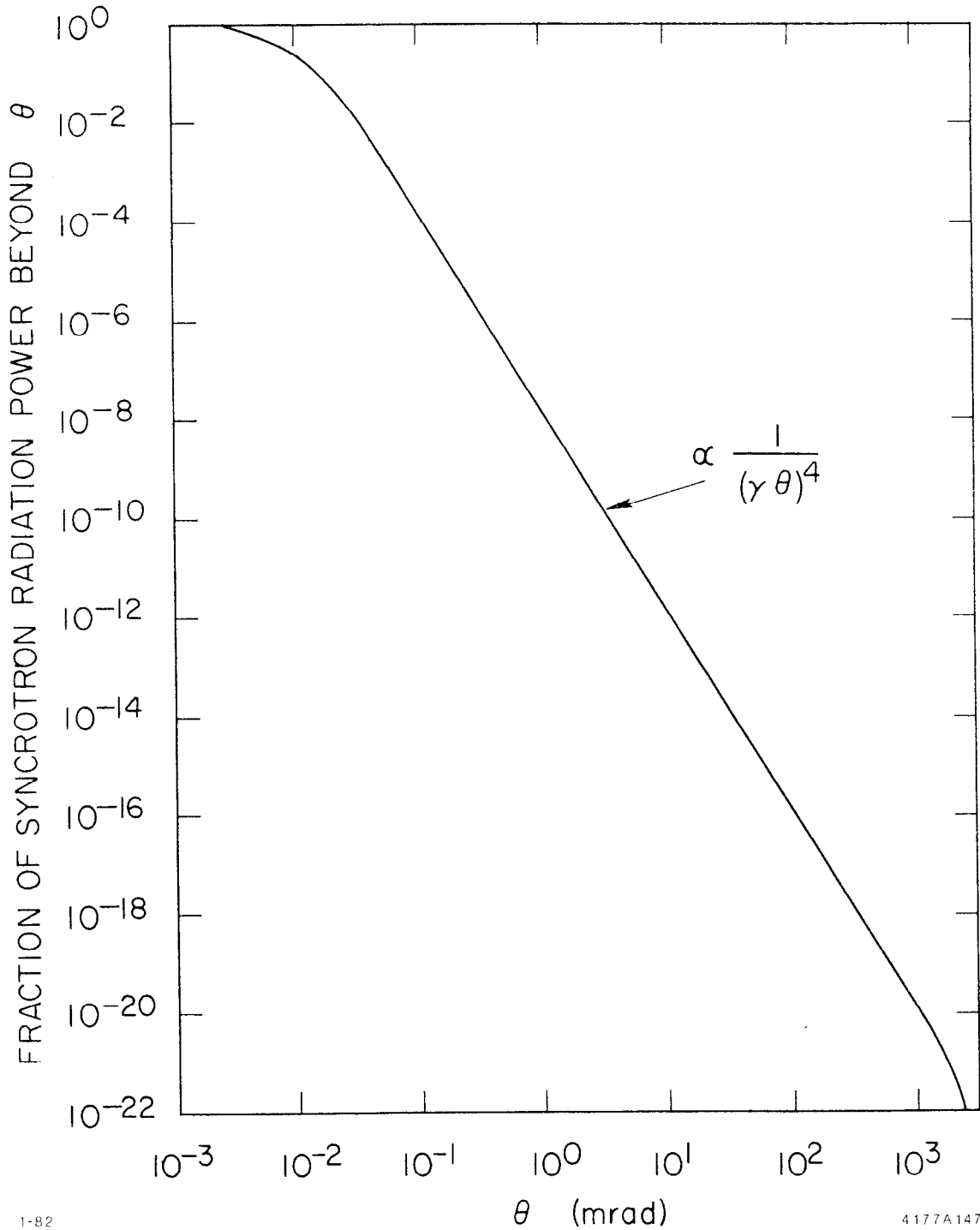
Two analyses of this question were made. SLC Workshop Note 68¹ evaluated the power in the synchrotron radiation from angle θ (to the e^\pm direction) to 180° in the laboratory. The fraction of the power radiated beyond angle θ (for all azimuthal angles) is shown in Figure 1 at 50 GeV. Note that a fraction less than 10^{-10} of the power is radiated beyond four mrad and less than 10^{-20} is radiated "backwards".

SLC Workshop Note 69² evaluated the synchrotron radiation photon yield at large angles out of the electron bending plane. Expressions were obtained for the fraction of radiated photons with frequencies $\omega \geq \omega_{\min}$ and at angles $\psi \geq \psi_{\min}$ (ψ measured out of e^\pm bend plane). For the SLC at 50 GeV, the beam-beam disruption for a $\beta^* = 1$ cm final focus³ results in e^\pm deflection angles ~ 0.7 mrad, critical energies $\hbar\omega_c \sim 100$ MeV, and total numbers of synchrotron photons ("beamstrahlung") $N_Y^{\text{TOT}} \sim 5 \times 10^{10}$. The resulting numbers of synchrotron radiation photons per crossing at large angles are then given in Figure 2.

In summary, the very large angle "backward" synchrotron photons should pose no problems to detectors. However, some increase in the detector backgrounds may come from non-"zero degree" synchrotron radiation striking the mask edges near the 2.5 mrad beamstrahlung stay clear.

References

1. D. Stork, SLC Workshop Note 68.
2. D. B. Smith, SLC Workshop Note 69/SCIPP Internal Memo, 81/1.
3. J. Jaros, Internal SLAC Memo AATF/80/22 (1980).



1-82

4177A147

Fig. 1. Fraction of synchrotron radiation power beyond angle θ to the electron direction. The curve is for 50 GeV e^\pm ($\gamma = 10^5$).

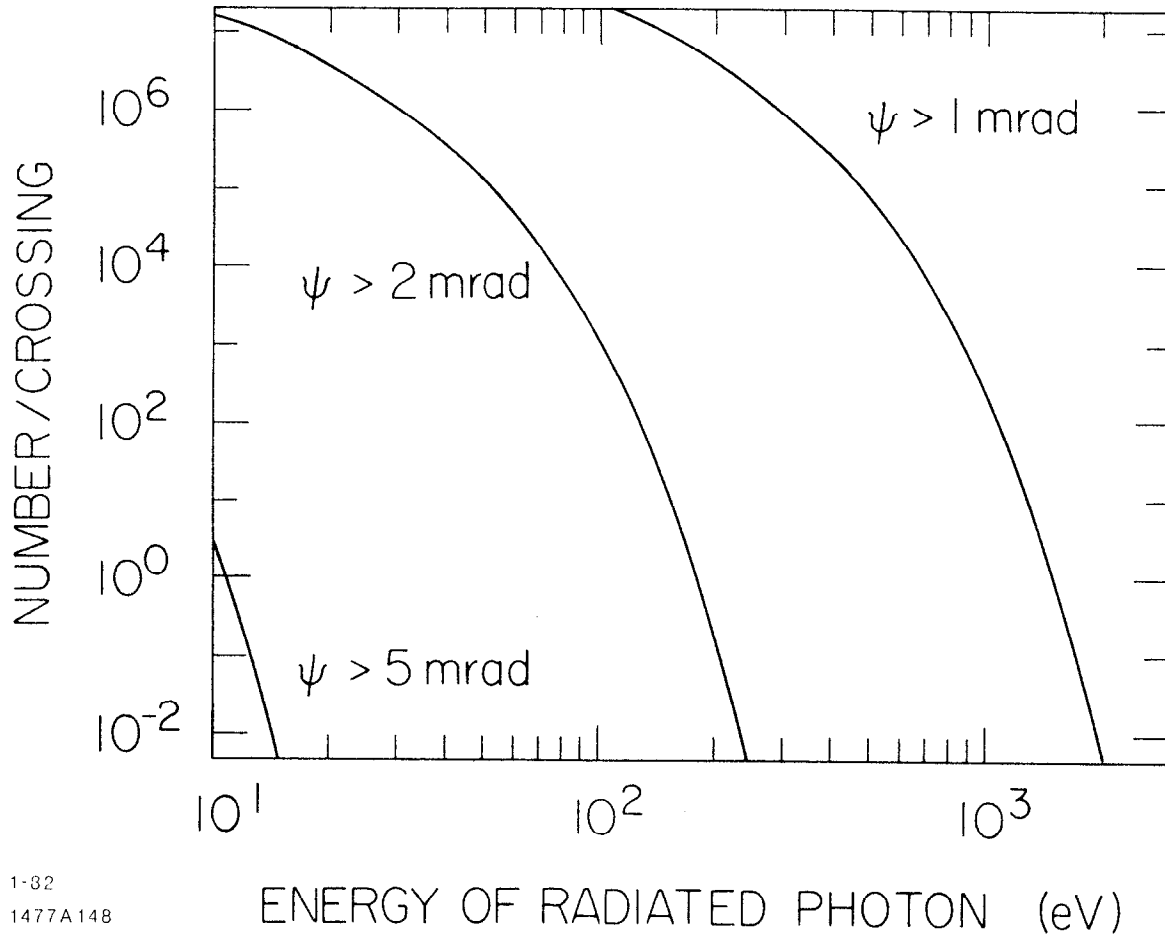


Fig. 2. Numbers of large angle synchrotron photons per crossing as a function of angle ψ_{\min} , and minimum photon energy, $\hbar\omega$.

E. Mu-pairs from $e^+e^- \rightarrow e^+e^-\mu^+\mu^-$ at the Z^0 Peak

In the Weinberg-Salam model the total cross section for $e^+e^- \rightarrow Z^0 \rightarrow \mu^+\mu^-$ at the Z^0 peak is ~ 1.9 nb (for $\sin^2\theta_W = 0.25$, giving $M_{Z^0} = 87$ GeV and $\Gamma_{Z^0} = 2.3$ GeV). The total cross section for $e^+e^- \rightarrow \gamma^* \rightarrow \mu^+\mu^-$ is ~ 0.01 nb. The energy dependence is given in Figure 1; see, for example, Ref. 1.

The process $e^+e^- \rightarrow e^+e^-\mu^+\mu^-$ at 50 GeV beam energy has a cross section of 200 nb, a factor hundred larger than the Z^0 signal. In $>99\%$ of the events, both final e^+ and e^- go down the beampipe, leaving two muons as the signature of these events.

To investigate whether this background is serious, the PEP-9 Monte Carlo program was used to simulate a possible trigger condition that would reduce the cross section to a manageable level. The events were generated with a generator due to J. Vermaseren and included the diagrams listed in Figure 1.

Cutting on the muon energies and/or on the collinearity angle, θ , between the muons we obtain the results listed in Table I. The cross sections and their energy dependence near the Z^0 are also shown in Figure 2.

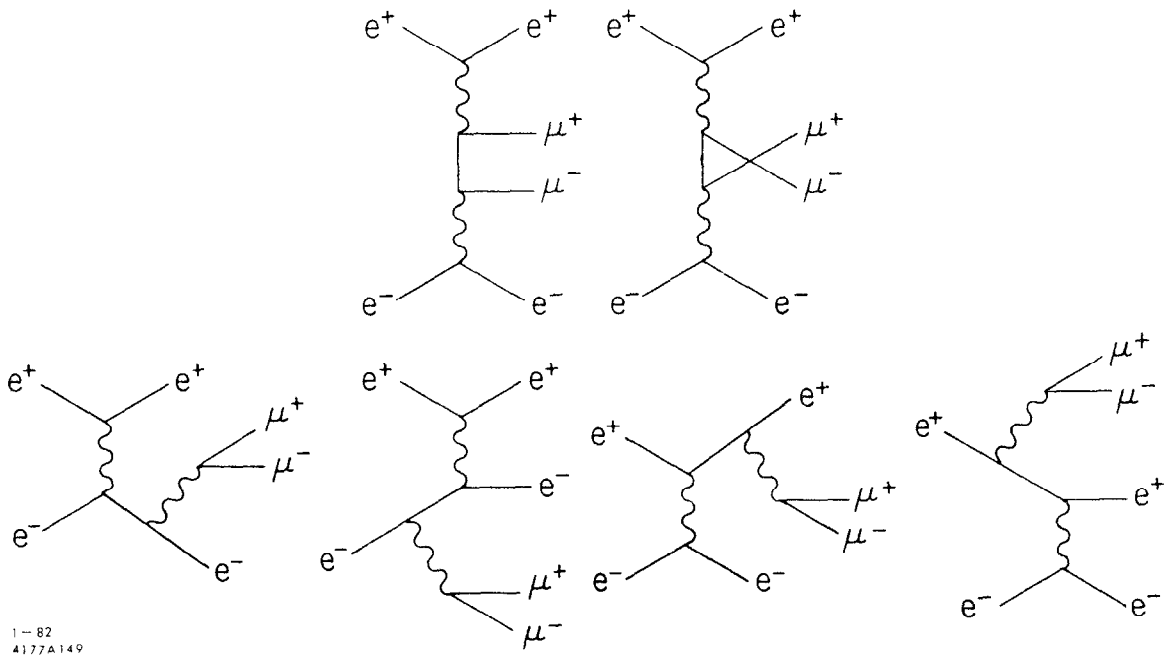
It follows that even with rather loose cuts the background due to $e^+e^- \rightarrow e^+e^-\mu^+\mu^-$ will be negligible.

Reference

1. J. Ellis and M. K. Gaillard, CERN 76-18 Yellow Report.

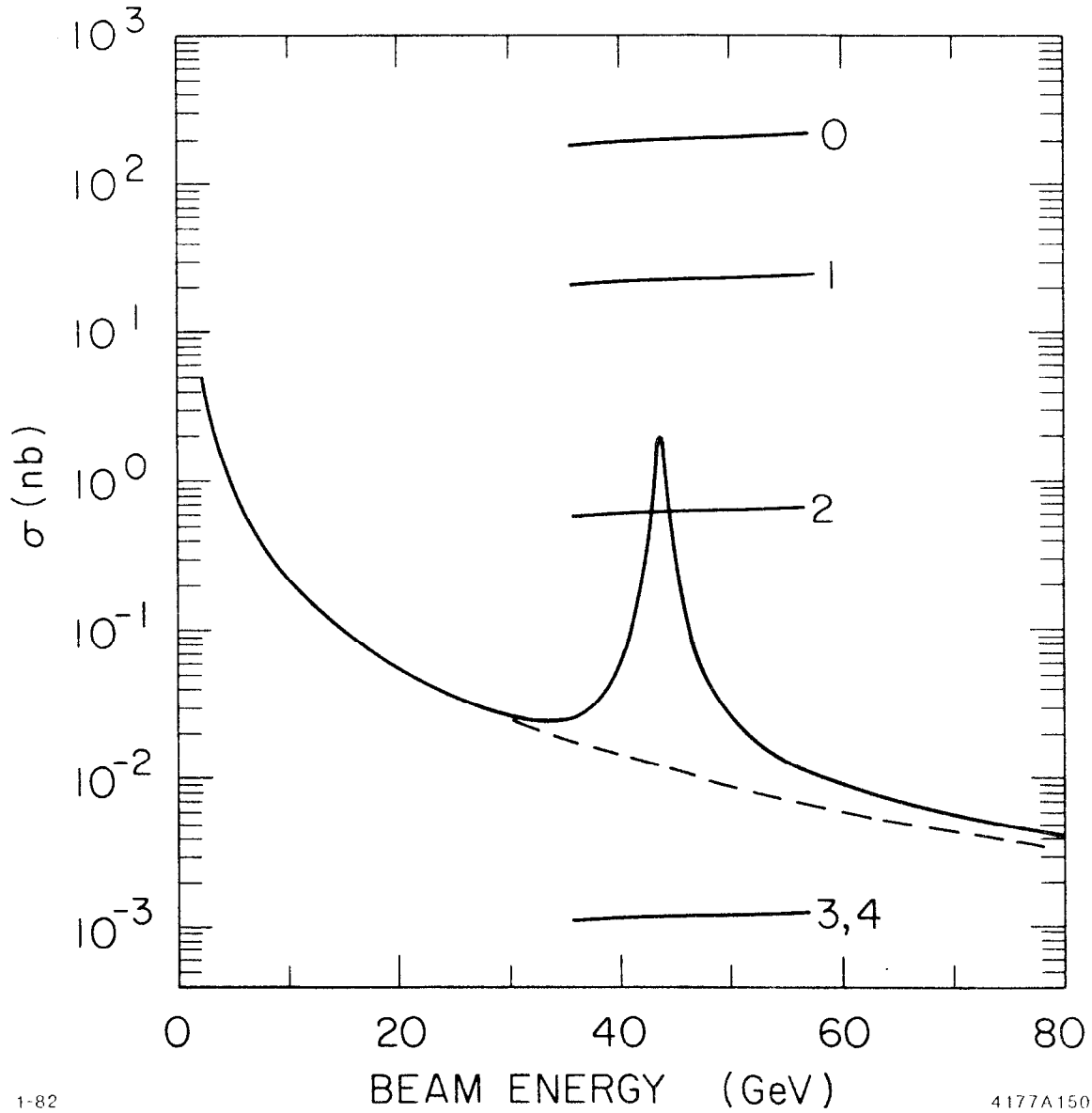
Table I.

Case	E(one muon)	E(other muon)	θ	Cross Section
0	no cut	no cut	no cut	201. nb
1	no cut	no cut	$> 145^\circ$	19.9 nb
2	> 20 GeV	> 20 GeV	no cut	0.5 nb
3	> 20 GeV	> 20 GeV	$> 145^\circ$	$< 1.$ pb
4	> 40 GeV	> 40 GeV	no cut	$< 1.$ pb



1-82
4177A149

Fig. 1. Graphs used to evaluate cross section for $e^+e^- \rightarrow e^+e^-\mu^+\mu^-$.



1-82

4177A150

Fig. 2. Muon pairs from $e^+e^- \rightarrow e^+e^-\mu^+\mu^-$ at the Z^0 peak; cross sections "0" to "4" correspond to the data selections in Table I.

VII. e^+e^- OPTION FOR THE SLC

A. Introduction

Electron-electron interactions have not been studied for 15 years; present day storage ring accelerators cannot collide electrons. Historically it was Burton Richter,^{1,2} whose group 15-20 years ago last studied electron-electron interactions; then the energy was $\sqrt{s} = 1.11$ GeV. The future will belong to LEP and the SLC, but note that only the SLC has a two electron option.

It is estimated that this option will cost \$600,000. Additionally, time is not necessarily taken from the e^+e^- program. Time slots for e^+e^- will occur during periods of e^+ down time.

No new detectors are contemplated; costs and physics opportunities make this unjustified. Good electron, photon, and muon identification are the attributes one wishes in an e^+e^- detector.

B. e^+e^- Physics

The electron-electron elastic scattering rates, with both electron beams longitudinally polarized, are calculable. One is referred to SLC Workshop Notes Nos. 5 and 6.^{3,4} At forward angles the cross section is Møller/QED. At near 90° cm, the Weinberg-Salam contribution from an exchange Z^0 , increases the rates by 20%.

More detailed predictions -- polarization predictions -- are given in SLC Workshop Note No. 6. Four possible longitudinal polarization arrangements exist: two of these, σ_{LR} and σ_{RL} , are equal and small, 16% of the unpolarized rates, near 90° . Two of the polarization rates are large; σ_{LL} is 1.92 times the 90° unpolarized rate and σ_{RR} is 1.76 times the 90° unpolarized rate. The Z^0 exchange favors the σ_{LL} rate.

Two photon physics, $e^+e^- \rightarrow e^+e^- + \text{hadrons or leptons}$, is another target of opportunity. The rates are near equivalent to e^+e^- two photon physics but the tagging/identification of events is cleaner. The two lepton polarization makes possible detailed tests.

Finally, the spectacular possibility. Harari⁵ has theorized that the electron is a three rishon composite $\bar{T}\bar{T}\bar{T}$. The theory is an alternative to Grand Unification; Grand Unification predicts a neutrino mass and proton decay in the 10^{30} - 10^{34} year range. The Harari, composite lepton, composite W^+ , Z^0 theory suggests a neutrino mass but proton decay unlikely at the 10^{30} - 10^{34} year range.

There appear to be two signs for composite leptons in e^-e^- . One is a search for an electron form factor, a deviation from QED/Weinberg Salam using polarized electron scattering at $\sqrt{s} = 100$ GeV. Why not -- maybe. A second indication would be the discovery of one unambiguous event of the type

$$\begin{aligned} e^-e^- &\rightarrow \mu^-e^- \\ e^-e^- &\rightarrow \mu^-\mu^- \end{aligned} .$$

Under Grand Unification, this process is second order -- hopeless. Under the Harari scheme there is an exchange particle in the 10-100 TeV range permitting the process. One may refer to SLC Workshop No. 6 for rates experimentally accessible. Using a G^2s/π rate dependence one might see such muons if the exchange composite boson were less than 10 TeV. In any case it is an important question.

C. SLC e^-e^- Option

1. Electron Source

A second Pockels Cell needs to be added to the laser beam path. Then the two e^- pulses can start with the same or opposite longitudinal polarization.

2. Damping Ring

No changes. Both electron bunches use the electron damping ring. The two electron bunches have parallel or antiparallel spin direction as they reenter the linac. One electron bunch (the north arc one) has its spin direction optimized for the north arc; the other bunch is parallel or antiparallel to this direction.

3. Switchyard

A choice between two systems, a R.F. kicker or a ferrite core kicker magnet. Ample room exists for either system.

The R.F. kicker could replace the last 10 foot cavity of the linac. Its kick would be ± 0.25 mr at an R.F. frequency $2856 + (17.85/2)$ GHz. Cost would approximate \$150,000.

The ferrite kicker would cost less, \$80,000. The kicker angle would be ± 0.5 mr. The stability requirement, 0.05%, for the ferrite magnet choice is 4 times that of the R.F. kicker approach.

Either kicker would be followed by a special septum magnet, the design of which is described in SLC Workshop Note No. 25.⁶ This magnet must be moved into place and replace the initial dipole used for e^+e^- operation. The septum magnet cost is approximately \$200,000.

Both electron bunches enter the north, south arcs with the same phase space ellipse as for normal operation.

4. Arcs

The south arc magnets are switched in polarity. The electrons in the south arc precess and arrive at the IR in an arbitrary but calculable spin state. The north arc precession is preset optimally in the damping ring; the south arc precession then is fixed, non optimal. For cost reasons no hardware to correct this problem is envisioned. Calculations are in progress studying the south arc precession seeking to locate "energy windows" where the south and north arc electrons both arrive at the IR with appropriate longitudinal polarization.

5. Beam-Beam Interaction

In contrast to the electron-positron case there is a repulsion, an antipinch, as the two electron beams cross. A nominal luminosity $L_0 = 1.0 \times 10^{30}/\text{cm}^2\text{s}$ will be reduced 10% by this effect; a luminosity $L_0 = 4.0 \times 10^{30}/\text{cm}^2\text{s}$ will be reduced 30%.

6. Beam Dump

Separate or local beam dumps for the electron beams appear the cost effective solution. The electron beams exit at the hard bend points nearest the IR. The optics are shown in the IR Group Minutes.⁷

Incremental cost for two local beam dumps and vaults are estimated at \$100,000. No additional magnets are required.

7. Møller Polarimeter

A Møller iron foil may be placed in each of the spent beam trajectories, specifically in the soft bend region. At this point the electrons have not precessed significantly from their IR valves. Instrumentation to follow the trajectories of the Møller scattered electrons appear straightforward. This system monitors both electron beam polarizations directly and continuously.

References

1. W. Barber, G. O'Neill, B. Gittelman and B. Richter, Phys. Rev. D 3, 2796 (1971).
2. W. Barber, B. Gittelman, D. Cheng and G. O'Neill, Phys. Rev. Lett. 22, 902 (1969).
3. E. Jenkins, SLC Workshop Note 5.
4. E. Jenkins and K.-W. Lai, SLC Workshop Note 6.
5. H. Harari, SLAC Conference Talk, August 1980; H. Harari, SLAC Conference Talk, August 1981.
6. E. Jenkins, SLC Workshop Note 25.
7. E. Jenkins, SLC "IR Group" Minutes, October 10, 1981.

VIII. PERMANENT MAGNET QUADRUPOLES FOR THE SLC FINAL-FOCUS SYSTEM

A full-scale, fixed-field prototype of a 2-cm bore, "mini-quad" quadrupole has been designed and is now being fabricated. The magnet is formed of twenty layers along the axial direction which have sixteen permanent magnet blocks (samarium cobalt) magnetized as shown in Fig. 1. The magnet assembly is essentially a precision, slotted, brass guide for the SmCo_5 blocks with aluminum retaining rings and a seamless, stainless steel vacuum tube supported and aligned by aluminum guides at either end. The faces of the blocks nearest the magnet axis thus form a sixteen-sided regular polyhedron.

The final magnetic design (R. Holsinger) resulted in a pole tip field of 9.64 kG in the assembled magnet for a material having a residual induction of $BR = 8.5$ kG. Figure 2 shows a 'Pandira' simulation of a single block together with its dimensions for a type 'C' field orientation (easy axis parallel to long axis). Magnetic measurements of the individual blocks produced by Recoma Inc. have indicated that they are within the +5% field tolerance and the 8.5 kG residual induction specifications requested. We therefore can expect to achieve the predicted results for the full magnet shown in Fig. 3.

Presently we are assembling single layers to determine the best assembly procedure as well as determine the effects of relative induction errors among the individual blocks of a layer. The design of the measurement coils has begun. There will be two independent coils -- one intended to measure relative harmonic strengths other than dipole and quadrupole and the other intended to measure the distribution of all harmonics as a function of the axial position. We intend to use a fast Fourier transform analyzer (FFT) for this purpose which analyzes the signal induced by rotating the magnet rather than the coil. The design of the magnet rotation fixture¹ has just begun.

There are a number of ways to vary the strength of such lens. We will study the use of differing shunt techniques as well as other methods involving adjustment of axial layers.^{2,3} Since we intend to measure

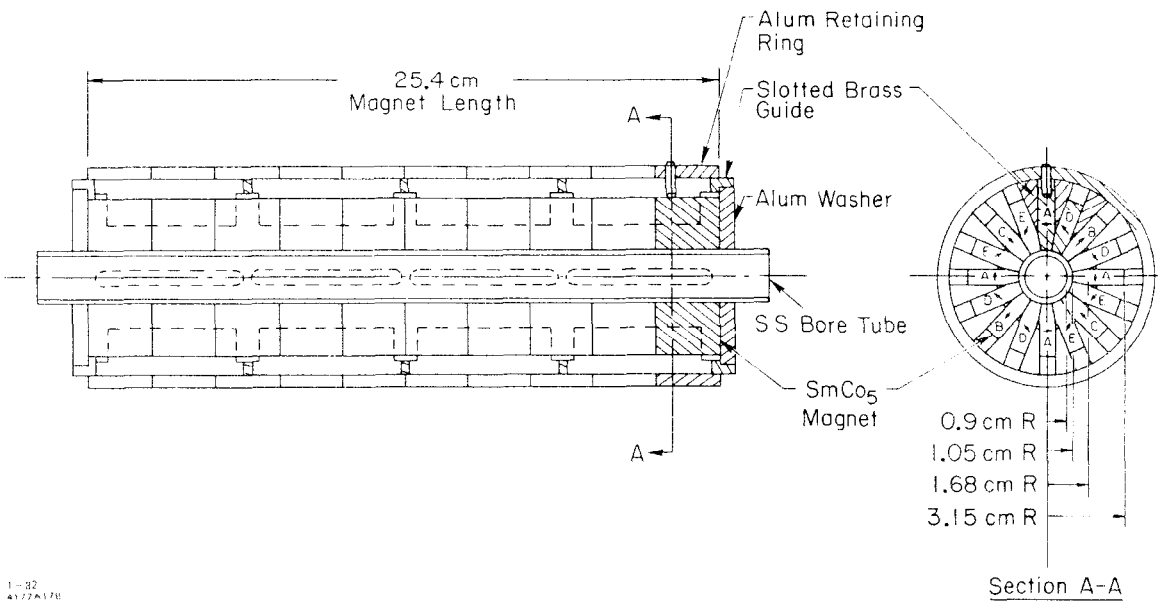
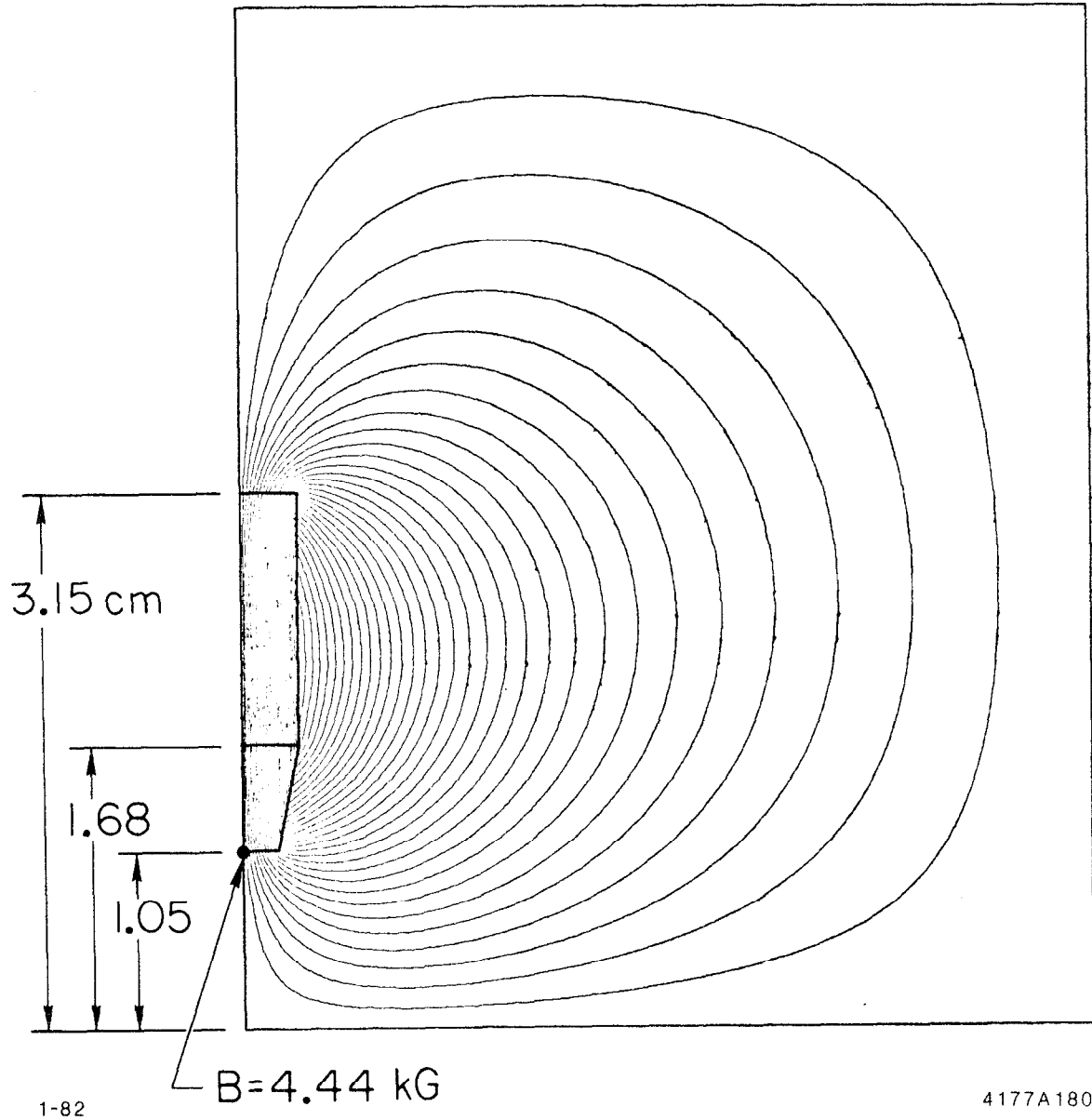


Fig. 1. Prototype "mini-quad" SmCo₅ permanent magnet quadrupole.



1-82

4177A180

Fig. 2. Single block magnetic field simulation.

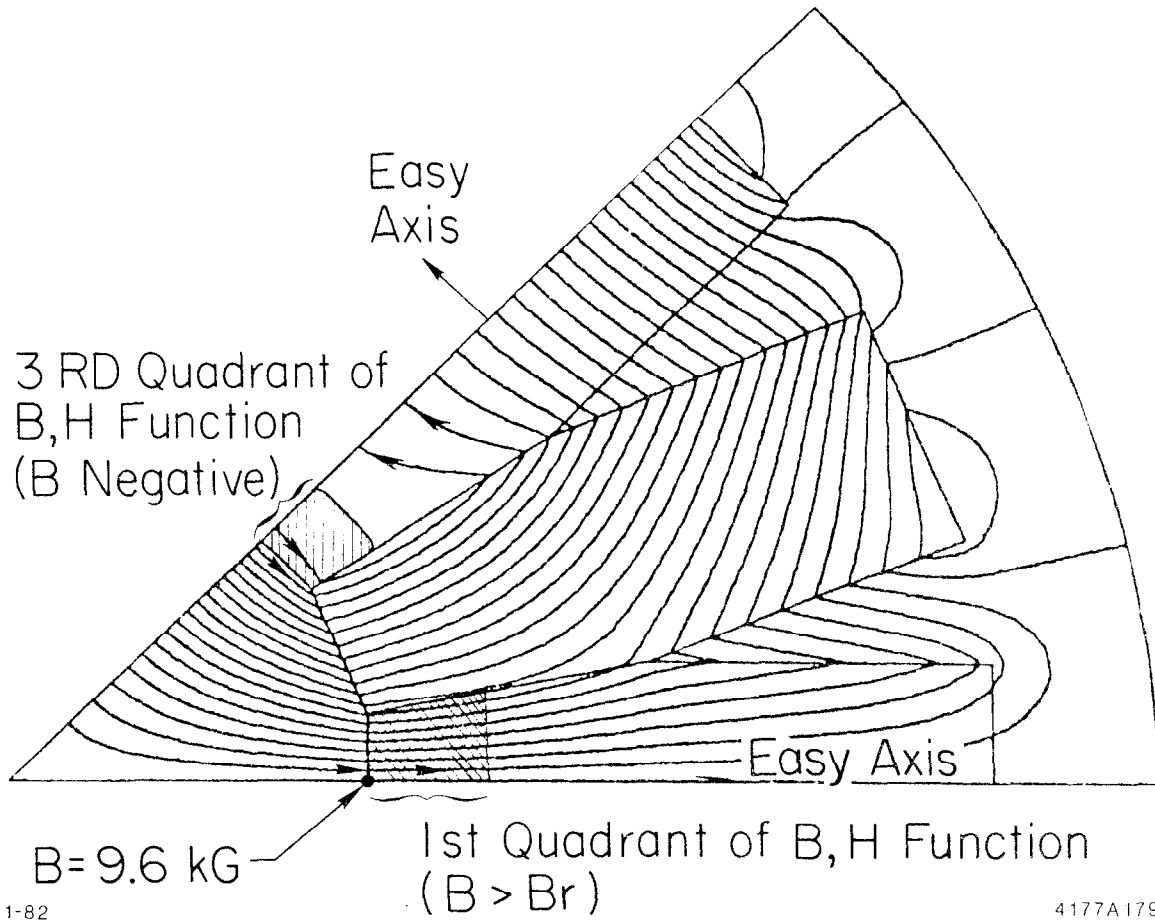


Fig. 3. Flux distribution in 1/8th of a permanent magnet quadrupole.

twenty axial layers in close axial proximity, we will also arrange to measure a single and double layer as a function of their axial separation. It is hoped to begin measurements in January, 1982.

References

1. D. Meyer, SLC Workshop Note 4.
2. J. A. J. Matthews, SLC "IR Group" Minutes, June 25, 1981.
3. R. L. Gluckstern and R. F. Holsinger, NIM (1981).

APPENDIX: SLC WORKSHOP NOTES

<u>NUMBER</u>	<u>TITLE</u>	<u>AUTHOR</u>
1.	A System for SLC Workshop Notes.	D. Leith
2.	Interaction Region Group Organization.	J. Matthews
3.	A Different Concept for Detector Magnets and Experimental Areas for the SLC.	D. Meyer
4.	Magnetic Measurement of Samarium-Cobalt Quadrupoles for the SLC.	D. Meyer
5.	Beam-Beam Interaction - Polarization Effects in the Electron-Electron Mode.	E. Jenkins
6.	Electron-Electron Interactions at 90 GeV.	E. Jenkins & K. Lai
7.	Tubes Monte Carlo - User's Guide.	C. T. Day
8.	Effects of the Z^0 on Bhabha Scattering and Its Use for Luminosity Monitor.	D. Koltick J. Va'Vra
9.	How to Use the Mark II Monte Carlo Program HOWL.	G. Hanson
10.	Tracking Jets Through a Solenoidal Field.	H. Sadrozinski
11.	Momentum Distributions and Angle and Momentum Correlations for Jets at the Z^0 Pole.	G. Tarnopolsky
12.	dE/dx Measurement in a Jet Chamber.	J. Va'Vra
13.	Proposed Parametrization of Tracking Chamber Measuring Capabilities.	G. Trilling
14.	Comparison of the Ali and Day Monte Carlos at 30 GeV and 100 GeV.	B. Barnett B. Blumfield
15.	Ultraviolet Cerenkov Counters for 50 - 50 GeV e^+e^- Detector.	D. Meyer
16.	New Madsim Model Number 9.	J. Brau & G. Tarnopolsky
17.	Spin-Momentum Correlations in Decay $\tau \rightarrow \rho\nu$.	J. Brau & G. Tarnopolsky
18.	Measurement of Jet Properties at SLC Energies.	V. Luth
19.	TOF Counter System for 50 + 50 GeV e^+e^- Detector.	J. M. Weiss
20.	Comments on the Radiative Correction Effects on Asymmetries Measurements Around the Z^0 .	G. Bonneaud

<u>NUMBER</u>	<u>TITLE</u>	<u>AUTHOR</u>
21.	e^+e^- Annihilation with a Polarized Electron Beam Around the Z^0 Mass.	G. Bonneaud
22.	Statistical Considerations for Muon Asymmetry Measurements at the Z^0 .	H. Ogren
23.	Effect of the Polar Angle Cut-Off on the Measurement of the Asymmetry in $Z \rightarrow \mu\mu$.	H. Sadrozinski
24.	Do We Need a Hadron Calorimeter in a Magnetic Detector?	R. Hollebeek, J. R. Johnson & P. Mockett
25.	Switchyard for the Collider - e^-e^- Option.	E. Jenkins
26.	Multiplicities, Momentum Distributions, and Muon Identification.	B. Blumenfield, B. Barnett & D. Hon
27.	Proposed Parametrization of the Measurement Capabilities Electromagnetic Calorimeters.	J. Hauptman
28.	Accuracy of Coupling-Constant Determinations for $e^-e^+ \rightarrow Z^0 \rightarrow \mu^-\mu^+$ with Longitudinally Polarized e^- .	J. Button-Shafer
29.	Report of Calorimeter Subgroup on Resolution.	D. Coyne, V. Luth, L. Price & H. Williams
30.	Monte Carlo Study of Jet Statistics and a Simple Model for Track Acceptance Calculations at the SLC.	R. Fabrizio
31.	Drift Time Distributions in a Jet Chamber.	J. Va'Vra & L. Roberts
32.	General Formalism for e^+e^- Annihilations with Longitudinally Polarized Beams.	G. Bonneaud, C. Prescott & M. DeCrombrughe
33.	SLC Beam Position Monitor Near the Interaction Point.	D. Meyer
34.	A Compact Calorimeter for e^+e^- Annihilations in the 100 GeV Region.	M. Cavalli-Sforza D. Coyne
35.	Secondary Vertex Detection at the SLC--and Overview.	J. Jaros
36.	Large Drift Chambers with Multi-Wire Cell Design.	F. Grancagnolo, A. Seiden & D. Smith
37.	Can the Decay $\tau \rightarrow \rho\nu$ be Measured Directly?	J. Hauptman
38.	A Sketch of Progress in SLC Workshop - <i>Not for Distribution</i>	D. Leith

<u>NUMBER</u>	<u>TITLE</u>	<u>AUTHOR</u>
39.	Using the SLC as a Photon Accelerator.	C. Akerlof
40.	Momentum Resolution Requirements for Various Pieces of Physics.	H. Lynch
41.	Measurement of the τ Polarization at the SLC.	J. Brau & G. Tarnopolsky
42.	Spectroscopy of Mesons Containing t and b Quarks at the Z^0 .	M. Gilchriese
43.	Threshold Factors and the Top Quark Mass.	G. Tarnopolsky
44.	Spin Effects in $e^+e^- \rightarrow$ Hadrons at High Energy	D. Perret-Gallix
45.	Drift Chamber Gases - A Technology Review for the SLC Workshop.	G. Baranko
46.	Tracking Chamber Segmentation Requirements.	G. Trilling
47.	Monitoring the Separation Between Beams with Synchrotron Radiation.	S. Yellin
48.	Counting Neutrino Flavors at the SLC.	R. J. Cence
49.	Photons and Electrons from Beam-Gas Bremsstrahlung.	D. Koltick
50.	Short Lifetime Decay Studies at SLC Using Bubble Chambers.	R. C. Field
51.	What Limits Spatial Resolution in Drift Chambers?	J. Jaros
52.	An Azimuthally Symmetric, Induction-Field Drift Chamber as a Vertex Detector.	J. Hauptman
53.	Backgrounds at the SLC Interaction Point.	E. S. Miller & J. C. Sens
54.	Solid State Vertex Detectors.	N. Reay
55.	Detector Parameters for the Study of Three Jet Events at the SLC.	J. Dorfan
56.	Parametric Study of the Shape of $t\bar{t}$ Events at the SLC; Tagging t Events and Obtaining the t Mass.	J. Dorfan
57.	Production and Possible Detection of the Neutral Higgs Boson at Z Energies.	P. Kooijman
58.	Requirements on the Momentum Resolution for Z^0 Physics μ Tagging and Reconstruction of K_S^0 and D^0 .	H. Sadrozinski

<u>NUMBER</u>	<u>TITLE</u>	<u>AUTHOR</u>
59.	A Monte Carlo Study of Short Lifetime Decays at the SLC.	B. Ratcliff
60.	Miniature Jet Chamber for the Vertex Detector with Excellent Double Track Separation.	J. Va'Vra
61.	Physics Goals of Secondary Vertex Detector at SLC.	J. Layter
62.	High Resolution, Position Sensitive Solid State Detectors Utilizing the CCD Concept.	A. Bross
63.	Beam Pipe Fields.	S. Parker
64.	Beam Swapping and Polarization Mixing: Two Techniques to Cancel Spurious Experimental Asymmetries at the SLC.	J. Brau & G. Tarnopolsky
65.	The SLAC Linear Collider Final Focus System.	K. Brown, F. Bulos & J. Matthews
66.	Electron-Positron Annihilation to Two Photons as a Luminosity Monitor.	D. Koltick
67.	Beam Dumping for the SLAC Linear Collider.	T. Fieguth, L. Keller & D. Walz
68.	Large Angle Synchrotron Radiation.	D. Stork
69.	Approximate Distributions for Synchrotron Radiation at Large Angles Out of the Bending Plane.	D. Smith
70.	A Compton Polarimeter for the SLC.	R. Prepost
71.	Searching for Highly Interacting Quarks.	S. Parker
72.	Spin-Dependent Compton Scattering and Applications to an SLC Polarimeter.	C. Prescott
73.	Use of Magnetic Field Outside a Solenoid for Momentum Determination.	H. Lynch